

**VILNIUS UNIVERSITY
CPST SEMICONDUCTOR PHYSICS INSTITUTE**

GEORGIOS MANOLIS

**OPTICAL AND ELECTRICAL PROPERTIES OF HIGHLY EXCITED
3C-SIC CRYSTALS AND HETEROSTRUCTURES**

Doctoral Thesis

Technological Sciences, Material Engineering (08T)

Vilnius, 2013

Dissertation was prepared at the Institute Applied Research, Vilnius University in 2008 – 2012.

Scientific Supervisor:

Dr. Ramūnas Aleksiejūnas (Vilnius University, Physical Sciences, Physics – 02P, Semiconductor Physics (P 265))

Reziumė

Kubinis silicio karbidas (3C-SiC) yra perspektyvi plačiatarpė puslaidininkinė medžiaga, savo savybėmis pranokstanti silicį (Si) ir įgalinanti gaminti elektronikos prietaisus, kurie veiktų didelių galių ir dažnių srityje, aukštose temperatūrose ir kenksmingose aplinkose. Kol kas 3C-SiC kokybė yra ganėtinai prasta lyginant su Si ir vis dar neprilygsta heksagoninių silicio karbido politipų (4H- ir 6H-SiC) kokybei, kuriuos jau yra galima įsigyti komerciniu būdu. Užaugintas 3C-SiC vis dar pasižymi dideliu įvairių defektų (kitų politipų intarpai, dvyniavimosi domenai ir pakavimo defektai) kiekiu. Kokybiško 3C-SiC užauginimas yra sunkus uždavinys, nes kubinė SiC fazė yra metastabili, dėl to turi būti išpildytos specialios sąlygos, kad būtų įmanoma kontroliuoti jos augimą.

Šiame darbe aukštos laikinės skyros optiniai metodai yra pritaikomi 3C-SiC kristalų elektroninių parametrų nustatymui, siekiant juos susieti su auginimo technologijomis ir taip prisidėti prie šios medžiagos auginimo sąlygų optimizavimo.

Pagrindiniai šio darbo tikslai buvo ištirti krūvininkų rekombinacijos ir pernašos parametrų 3C-SiC kristaluose priklausomybę nuo auginimo technologinių parametrų, priemaišų ir struktūrinių defektų tankio.

Buvo atrastas naujas būdas, paremtas skirtuminio pralaidumo metodika, skirtas krūvininkų gaudyklių koncentracijai plonuose sluoksniuose išmatuoti ir nustatyti šių gaudyklių prigimtį. Svarbu yra tai, kad tokia medžiagos charakterizacija yra atliekama medžiagos neardančia optine metodika.

Mes ištyrėme tam tikrų auginimo sąlygų skirtingose auginimo technologijose įtaką elektroninėms 3C-SiC savybėms. Tai leido atlikti netiesioginį sluoksnių struktūrinės kokybės nustatymą naudojant medžiagos neardančias optines priemones, ir įvertinti skirtingų auginimo technologijų potencialą optimizuojant 3C-SiC auginimą. Remiantis šiais rezultatais mes galėjome nustatyti ir palyginti 3C-SiC kristalų kokybę, kurie buvo užauginti

skirtingomis, plačiausiai naudojamomis technologijomis, kas leido nustatyti perspektyviausią auginimo technologiją 3C-SiC puslaidininkiui.

Galiausiai, mes ištyrėme kokią įtaką turi padėklų paviršinės savybės krūvininkų gyvavimo trukmei ir judriui epitaksiniuose sluoksniuose.

Table of contents

Acknowledgements.....	9
Introduction.....	11
The main tasks of the Thesis	13
Scientific novelty and importance	13
Statements.....	14
Layout of the Thesis	14
Author's contribution	15
List of publications related to this Thesis.....	15
List of publications not included in this thesis.....	16
Chapter 1 Silicon carbide – an overview	17
1.1 The history of SiC	17
1.2 The crystal structure of SiC.....	18
1.3 Applications of SiC	21
1.4 The cubic SiC	24
1.5 Defects in SiC.....	26
1.5.1 Point defects.....	27
1.5.2 Extended defects	28
Chapter 2 Growth of 3C-SiC	33
2.1 Vapor Liquid Solid deposition (VLS).....	33
2.2 Chemical Vapor Deposition (CVD).....	37
2.2.1 CVD on VLS seed layer.....	37
2.2.2 CVD on undulant Si.....	38
2.3 Sublimation Epitaxy (SE).....	39
2.4 Continuous Feed - Physical Vapor Transport (CF-PVT).....	42
Chapter 3 Carrier Dynamics and optical time-resolved techniques	45

3.1 Free carriers in semiconductors.....	47
3.2 Carrier dynamics	48
3.2.1 Carrier transport	48
3.2.2 Carrier scattering mechanisms.....	50
3.2.3 Carrier recombination	53
3.2.4 Carrier trapping.....	57
3.2.5 Compensation in semiconductors	59
3.2.6 Thermal activation energy of impurities.....	61
3.3 Optical time-resolved techniques	62
3.3.1 Light-induced transient grating (LITG) technique	62
3.3.2 Differential transmittance (DT) technique.....	65
Chapter 4 Experimental setup.....	67
4.1 Light Induced Transient Grating (LITG)	67
4.2 Differential Transmission (DT).....	69
4.2.1 Collinear configuration	69
4.2.2 Orthogonal configuration.....	70
Chapter 5 Excess carriers decay in 3C-SiC	73
5.1 Excess carrier recombination lifetime of bulk n-type 3C-SiC	73
5.1.1 Introduction.....	73
5.1.2 Samples and techniques	74
5.1.3 Results and discussion	75
5.1.4 Conclusions.....	80
5.2 Carrier dynamics in 3C-SiC epilayers grown by sublimation epitaxy on different SiC substrates	81
5.2.1 Introduction.....	81
5.2.2 Samples and techniques	81

5.2.3 Results and discussion	84
5.2.4 Conclusions	96
Chapter 6 Carrier dynamics of differently grown 3C-SiC layers	97
6.1 Reflections of VLS growth conditions on epilayer properties	98
6.1.1 Introduction	98
6.1.2 Samples and techniques	99
6.1.3 Results and discussion	100
6.1.4 Conclusions	103
6.2 Electronic properties of high growth rate sublimation epitaxy of 3C-SiC	103
6.2.1 Introduction	103
6.2.2 Samples and techniques	104
6.2.3 Results and discussion	105
6.2.4 Conclusions	108
6.3 Study of homoepitaxial CVD 3C-SiC on VLS seed layer	109
6.3.1 Introduction	109
6.3.2 Samples and experimental techniques	109
6.3.3 Results and discussion	110
Samples CL1, CL3, CL4	110
Samples CN1, CN2, CN3	112
Lifetime vs. CVD layer thickness	115
6.3.4 Conclusions	117
6.4 Electronic properties of bulk 3C-SiC grown by sublimation techniques	117
6.4.1 Introduction	118
6.4.2 Samples and techniques	118

6.4.3 Results and discussion	121
Samples B4 and B5 (CF-PVT).....	121
Samples FS50 and FS24 (SE)	126
6.4.4 Conclusions.....	126
6.5 Comparison of the electronic properties in variously grown 3C-SiC ...	127
Chapter 7 The influence of substrate surface morphology on 3C-SiC electronic properties	129
7.1 Defect induced anisotropy in diffusivity of homoepitaxial 3C-SiC.....	129
7.1.1 Introduction.....	129
7.1.2 Samples and experimental techniques	129
7.1.3 Results and discussion	131
7.1.4 Conclusions.....	134
7.2 On the substrate roughness correlated carrier lifetime.....	134
7.2.1 Introduction.....	134
7.2.2 Samples and experimental techniques	135
7.2.3 Results and discussion	136
7.2.4 Conclusions.....	138
Prospects.....	139
References.....	141

Acknowledgements

First of all I would like to express my sincere thanks to my supervisor Dr. Ramunas Aleksejunas.

My warmer thanks to Prof. Kestutis Jarasiunas for this journey in science he offered to me.

I would express my sincere thanks to Dr Arunas Kadys, Dr Tadas Malinauskas, Dr Saulus Nargelas, Patrikas Scajev and Dr Gediminas Liaudaugas.

My special thanks to Dr. Vytautas Grivickas for his advices and cooperation in several publications, as well as, Mindaugas Karaliunas for his support during exams.

I have to mention all MANSiC members for their cooperation and discussions during meeting, schools and conferences. I have to thank especially Dr. Jean Lorenzzi and Dr. Georgios Zoulis for their hospitality during my training on VLS and LTPL techniques. Last but not least, I must express my warm thanks to Dr. Milena Beshkova who has spent hours and hours to scientific, and not only, conversations.

Among others, I am thankful to Dr. Kostantinos Giannakopoulos and HEAL-LINK for the unlimited feeding of knowledge.

I am thankful to E.U., via MANSiC project, and to my family for their economic support of my studies.

Finally, I devote this Thesis to my brother Sotiris.

Introduction

The study of interactions between light and matter is one of the most extended research fields both for their fundamental theoretical approaches and for their applications. Optical phenomena that occur during these interactions resulted in the development of a variety of methods for the investigation of material properties. As scientific knowledge is growing and spectroscopic methods based on linear interactions have been widely and successfully used, novel spectroscopic methods, based on non-linear regime of light and matter interactions, are introduced expanding the scientific horizons. The characterization of materials by contactless non-destructive optical techniques is of crucial importance for materials growth process optimization so for the layers as long as for their heterostructures.

Since lasers, and especially pulsed ones, became available all excitation-dependent material properties can be regarded in their nonlinear regime. Short laser pulses in the wide family of pump-probe techniques allow the monitoring of carrier motion, creation, and annihilation by means of both absorptive and refractive optical nonlinearities from nanosecond to femtosecond time-scales. Among the wide variety of pump-probe modifications, light-induced transient grating (LITG) and differential transmission (DT) techniques have been utilized for the photo-induced carrier monitoring. LITG technique, based on sample's excitation by a spatially modulated light field, allows the simultaneous investigation of carrier transport as well as the generation and recombination processes at the surface and interior of both thin layers and bulk crystals. DT, as a simpler technique, which is based on modulated absorption of a below band gap energy photons, is in widespread use and is a general tool applicable to most semiconductor materials and devices, provides an exceptional advantage of its different geometries for the study of carrier recombination mechanisms. Thus, nonlinear optical techniques of active spectroscopy are presented as a bridge between the optical and electronic semiconductors properties as, based on strong correlation between electrical

and optical phenomena, potentially they are able to analyze electrical processes by optical means.

Silicon carbide (SiC) even if as synthetic composite has almost two centuries of life only it was studied as a semiconductor only at the beginning of 20th century. Nevertheless, only in 50's, when space and nuclear applications started to develop, SiC has attracted the interest after the development of a new method for the growth of high quality single crystals. Since then, many research activities coming from several institutes, universities and industries all over the world have been the focused on SiC. This is because it possesses physical properties that make it a perfect candidate for applications on devices operating at high temperatures, frequencies and powers, under strong radiation and chemical corrosive environments. Among the over 200 polytypes that have been identified only three of them are the most common: the one (and only) cubic (3C-SiC) and the two hexagonal (4H- and 6H-SiC). Up to now, research and industry have focus on these hexagonal polytypes. Even if 3C-SiC is expected to have superior properties than the hexagonal counterparts, the production of adequate quality substrates has been proved problematic. Nevertheless, in order to benefit of all potentialities of 3C-SiC, epitaxial layers with an acceptable quality must be grown. Many researchers have faced the difficulty of growing 3C-SiC layers with a reasonable quality due to the large crystal lattice mismatch (~20 %) with Si substrate and the difference in their thermal expansion coefficients (~8 %). The use of hexagonal SiC polytypes as substrate for the growth of 3C-SiC, instead of the physical mismatches one faces the systematic formation of twin boundaries which are highly undesirable for device performances. As non-equilibrium carrier lifetime and diffusivity are very sensitive to the existence of point and extended defects in a material, LITG and DT techniques are aiming through their feedback information to growers the improvement of 3C-SiC structural quality. The latter was my task as a member of characterization group in MANSiC project funded from European Union.

The main tasks of the Thesis

1. Investigation of carrier dynamics in 3C-SiC thin and bulk layers grown by VLS, CVD, SE and CF-PVT techniques at various excitation and temperature conditions and evaluation of their optical/electrical parameters.
2. Investigation of the impact that 3C-SiC growth parameters have on the properties of 3C-SiC by means of optical time-resolved techniques.
3. Determination of concentration and nature of carrier traps in relatively thin epilayers by implementation of time-resolved optical techniques.
4. Investigation of excess carrier recombination and diffusion peculiarities arising due to the extended defects in 3C-SiC in a wide range of excitations and temperatures.

Scientific novelty and importance

Optical time-resolved techniques, such as LITG and DT, are known and used already for several decades. Despite this fact, we succeeded to extend their field of application and to observe some novel phenomena in 3C-SiC related to its growth techniques. We used LITG and DT techniques to investigate carrier recombination and transport in a wide band gap indirect semiconductor like 3C-SiC. We found a novel way, based on DT technique, to determine the carrier trap concentration in finite thickness layers, as well as to attribute them to specific impurity species. We investigated the influence of several particular growth conditions at different growth techniques on electronic properties of grown layers, and hence, a chance to characterize indirectly layers structural perfection by non-destructive optical means, as well as to evaluate the potentiality of growth techniques to 3C-SiC material optimization. Based on these results, we were able to evaluate and compare quality of 3C-SiC specimens manufactured by nearly all currently available growth techniques that allowed distinguishing the most promising growth methods for 3C-SiC semiconductor.

Statements

1. Density and thermal activation energy of a dominant carrier trapping center in 3C-SiC can be determined from the differential transmission experiment under a proper choice of experimental conditions. Chemical nature of the traps can be assessed from the activation energy and comparison of measured trap density with SIMS data.
2. Conventional vapor-liquid-solid (VLS) deposition technique does not contribute to optimization of electronic properties of homopolytypically overgrown by SE, CF-PVT and CVD 3C-SiC layers. Purification procedure in VLS technique results in promising seed layers with advanced electronic properties.
3. The majority of currently used growth methods (slow- and fast-SE, CF-PVT and VLS) does not provide means to enhance electrical quality of 3C-SiC layers by increasing layer thickness or optimizing growth temperature; carrier lifetime remains within 2-6 ns range independent on growth conditions. CVD alone provided 3C-SiC layers with the lifetime increasing with layer thickness d as $\tau_R \propto (1.9 \pm 0.1) \times d$ within 5-12 μm region and reaching 100 ns in the thickest samples.
4. The morphology of substrate surface can modulate the electronic properties of 3C-SiC epilayers. Anisotropy in ambipolar carrier diffusivity in 3C-SiC layers grown by CVD can be achieved by ordered arrays of grooves that do not damage the high lifetime values. Also, bulk lifetime in 3C-SiC epilayers grown homo- or hetero-polytypicaly by SE increases with substrate short range roughness.

Layout of the Thesis

This Thesis is organized in seven chapters as follows. Chapter 1 is an overview on SiC – historic background along with general information on the material, including structural and physical properties, as well as, a brief account of defects that appear in SiC. Chapter 2 is a brief introduction on growth

techniques have been used for our samples production. Chapter 3 gives an overview on carrier dynamics (recombination, transport, trapping) and on optical time-resolved principles. Chapter 4 describes the experimental setups which have been used for measurements during my doctoral studies. Chapters 5, 6 and 7 contain the experimental results of 3C-SiC; Chapter 5 is dealing with recombination and trapping processes of excess carriers, and Chapter 6 deals with correlation of electronic and structural properties of 3C-SiC bulk and thin layers, as well as, with their growth conditions. Finally, Chapter 7 deals with the effects that substrate can have on epilayer electronic properties.

Author's contribution

The author carried out the vast majority of experiments described in the thesis. The author was very active in interpretation of results and prepared several drafts of present publications, but also contributed to preparation process of others drafts.

List of publications related to this Thesis

- [A1] V. Grivickas, **G. Manolis**, K. Gulbinas, K. Jarasiunas, and M. Kato, “Excess carrier recombination lifetime of bulk n-type 3C-SiC”, Applied Physics Letters **95**, 242110 (2009).
- [A2] N. Jegenyas, **G. Manolis**, J. Lorenzzi, V. Souliere, D. Dompont, A. Boulle, G. Ferro and K. Jarasiunas, “Nondestructive evaluation of photo-electrical properties of 3C-SiC (111) homoepitaxial layers grown by CVD”, Materials Science Forum **679-680** 153 (2011).
- [A3] **G. Manolis**, K. Jarasiunas, I. G. Galben and D. Chaussende, “Optical Investigation of Electronic Properties in Bulk and Surface Region of Sublimation-grown 3C-SiC Crystals”, Materials Science Forum **615-617** 303 (2009).
- [A4] **G. Manolis**, G. Zoulis, S. Juillaguet, J. Lorenzzi, G. Ferro, J. Camassel and K. Jarasiunas, “Optical characterization of VLS+CVD grown 3C-SiC

films by non-linear and photoluminescence techniques”, Materials Science Forum **645-648** 443 (2010).

List of publications not included in this thesis

- [B1] V. Grivickas, K. Gulbinas, P. Grivickas, **G. Manolis** and J. Linnros, “Fundamental band edge absorption in 3C-SiC: phonon absorption assisted transitions”, Materials Science Forum **645-648** 231 (2010)
- [B2] **G. Manolis**, M. Beshkova, M. Syvajarvi, R. Yakimova and K. Jarasiunas, “Carrier dynamics in hetero- and homo-epitaxially sublimation grown 3C-SiC layers” Materials Science Forum **679-680** 161 (2011)
- [B3] V. Grivickas, K. Gulbinas, **G. Manolis**, M. Kato and J. Linnros, “Internal Stress in Freestanding 3C-SiC Grown on Si and Relation to Carrier Lifetime”, AIP Conference Proceedings **1292** 91 (2010)
- [B4] P. Onufrijevs, T. Serevicius, P. Scajev, **G. Manolis**, A. Medvids, L. Chernyak, E. Kuokstis, C. C. Yang and K. Jarasiunas, “Characterization of Optical and Photoelectrical Properties of ZnO Crystals”, Acta Physica Polonica A **119**(2) 274 (2011)
- [B5] P. Ščajev, P. Onufrijevs, **G. Manolis**, M. Karaliūnas, S. Nargelas, N. Jegenyes, J. Lorenzzi, G. Ferro, M. Beshkova, R. Vasiliauskas, M. Syväjärvi, R. Yakimova, M. Kato and K. Jarašiūnas, “On applicability of time-resolved optical techniques for characterization of differently grown 3C-SiC crystals and heterostructures”, Materials Science Forum **711** 159 (2012).
- [B6] A. Kadys, P. Scajev, **G. Manolis**, V. Gudelis, K. Jarasiunas, P. Abramov, S. Lebedev and A. Lebedev, “On the correlation of the structural perfection and nonequilibrium carrier parameters in 3C SiC heterostructures”, Materials Science Forum **645-648** 219 (2010).

Chapter 1 Silicon carbide – an overview

1.1 The history of SiC

Silicon carbide (SiC) as synthetic composite has almost two centuries of life. In early years, it was the product of Swedish chemist Jöns Jacob Berzelius in his attempt to synthesize diamond [1]. Later, Eugene Acheson was the first who produced polycrystalline SiC in an electric furnace in 1885 [2] named as carborundum in the namesake company [3]. SiC is also well known as moissanite from the name of French chemist Henri Moissan [4, 5] who has first found it naturally studying fragments of a meteorite. Even though, SiC is found only in minute quantities in nature, mainly in certain types of meteorite or in volcanic corundum deposits and kimberlites, it is remarkably common in space and almost exclusively in its cubic polytype.

As a semiconductor, SiC has been studied from the early 20th century. In 1907, the first publications on its electrical properties and electroluminescent diode was made by G.W. Pierce [6] and H.J. Round [7], respectively. Few years later, in 1912, the polytypism of SiC was identified by H. Baumhauer [8]. Nevertheless, the early success and the fast progress of the silicon technology overshadowed the research on SiC and its potential applications on electronic components for power applications at high frequencies and high temperatures. Only in the mid 50's, when space and nuclear applications started to develop, SiC has attracted the interest, especially, after the development by Jan Anthony Lely of a new method for the growth of high quality single crystals [9]. This method, commonly referred as the “Lely method”, was further improved by Hamilton [10] and Novikov [11] since the yield of the process was low, the sizes of the platelets irregular and while the most of the crystals have hexagonal crystal structure, no real control of the polytypism existed. The growing interest was resulted in the launch of the 1st International SiC Conference, in Boston (USA) in 1958. During the next two

decades, a new technique, called “(seeded) sublimation” or “modified Lely technique”, was developed by I. Swiderski et al. [12] and Y.M. Tairov and V.F. Tsvektov [13]. In parallel, initially Kendal [14] who studied the SiC formation by the cracking of gaseous precursors of C and Si at high temperatures and later Nishino [15] with the heteroepitaxial deposition on Si substrates were them who set the basis for today’s SiC chemical vapour deposition (CVD) technology.

1.2 The crystal structure of SiC

Silicon carbide is the only one stable compound in the Si-C binary phase diagram at atmospheric pressure that contains equal amount of Si and C. The Si-C bond with bonding energy of 289 kJ/mol and length of 1.89 Å is nearly covalent with ionicity value of 0.177 [16] having Si atom positively and C atom negatively charged. The smallest building element of any SiC lattice is a tetrahedron defined by strong sp^3 orbitals, either SiC_4 or CSi_4 (Fig. 1.2.1) which means that each carbon atom is surrounded by four silicon atoms with an inter-nuclear angle $\Theta=109.28^\circ$ and total tetrahedron height of 2.52 Å. Therefore, the first neighbor shell configuration is identical for all atoms in any crystalline structure of SiC with the ratio between the c- and a-axis to be

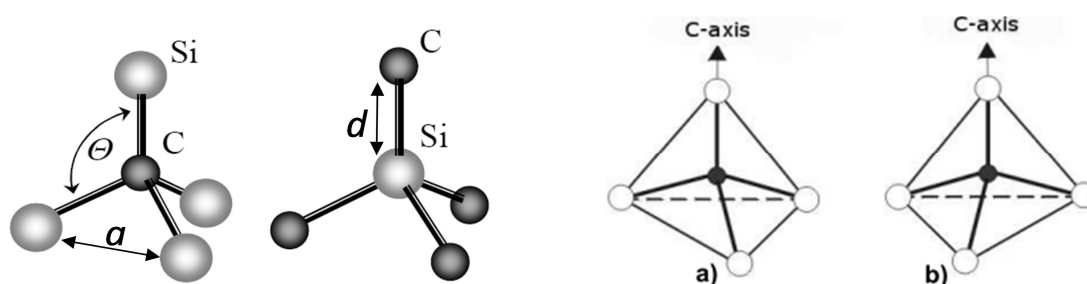


Fig.1.2.1 (left) Basic elements of SiC crystals: a tetrahedron contains one C and four Si atoms and vice versa. For the ideal bonding configuration $a=3.08$ Å, $d=1.89$ Å and $\Theta\sim 109^\circ$ [17]. (right) Perspective view of two SiC tetrahedra in which the c-axis is set along one of the Si-C bonds. The “twinned” SiC tetrahedron (b) arising from the rotation of the tetrahedron (a) by 180° around the c axis.

$c/a=0.8165n$, where n is the number of Si-C bilayers in the unit cell. The lattice constant - distance between two similar atoms - is usually denoted by the letter “ a ” and in SiC is 3.08 Å. In Fig. 1.2.1(right) one of the Si-C bonds has been taken as c axis and the tetrahedron shows a 3rd order rotational symmetry around each of the bonds, especially around the c axis. Since the 3rd order rotation symmetry around the c -axis is broken by a 180° rotation around the c -axis, this creates a “twinned” structure (Fig. 1.2.1(right)b) which mirrors the “regular” structure of Fig. 1.2.1(right(a)).

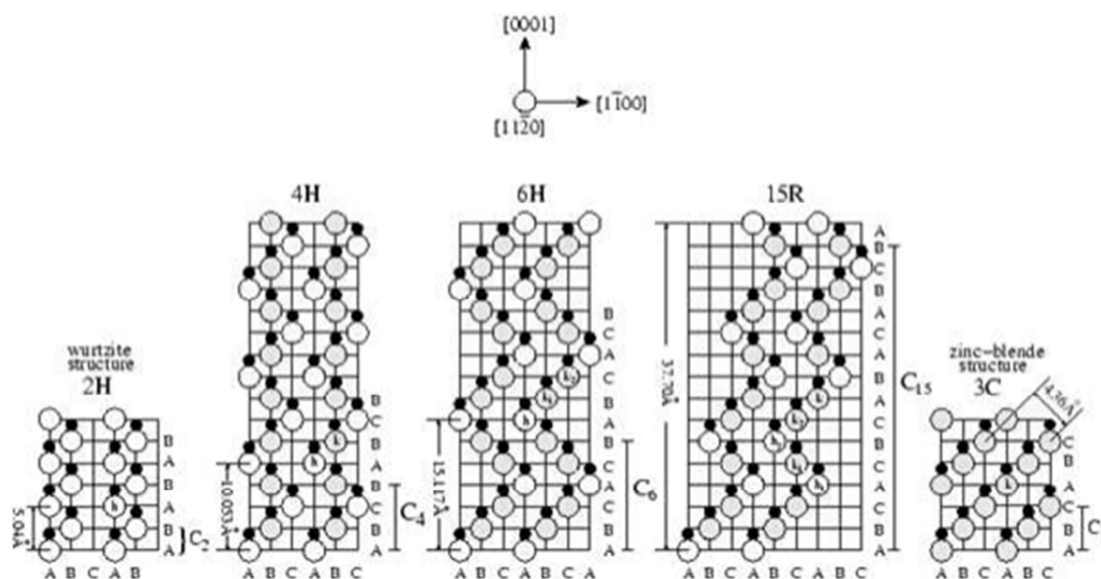


Fig. 1.2.2 Schematic representation in the $[1\ 1\ -2\ 0]$ of the most common SiC polytypes given with the Ramsdell notation. The white coloured bilayers represent the hexagonal sites (h) while the coloured ones the cubic sites (c) in regards to the previous layer.

Silicon carbide can be found or produced in single-crystalline, polycrystalline, or amorphous form. Single-crystalline silicon carbide occurs in many different crystalline structures denominated as “polytypes”. The phenomenon of polytypism is the special case of polymorphism when the variations of the same chemical compound are identical in two dimensions and differ in the third. More than 200 polytypes of SiC have been identified. Among them, there is only one cubic polytype referred also as β - or 3C-SiC. All the rest are called α -SiC. In addition, only few of them, such as 3C, 4H,

Table 1.1 Properties of SiCs, Si, diamond and GaN from [18, 19, 20, 21, 22, 23, 24].

Property		Si	3C-SiC	Diamond	4H-SiC	6H-SiC	α GaN
Space group		<i>Fd3m</i>	<i>F43m</i>	<i>Fd3m</i>	<i>P6₃mc</i>	<i>P6₃mc</i>	<i>P6₃mc</i>
Lattice const. (Å)	a-axis	5.43	4.36	3.567	3.08	3.08	3.18
	c-axis	-	-	-	10.08	15.12	5.18
Bond length (Å)		2.35	1.89	1.54	1.89	1.95	1.95
Density (g/cm ³)		2.3	3.2	3.5	3.2	3.2	6.1
Thermal cond. (W/cmK)		1.5	3.4	20	5.0	5.0	1.3
Melting point (°C)		1420	2830	4000	2830	2830	2500
Mohs hardness		7	≥9	10	≥9	≥9	≥9
Band gap (eV)		1.12	2.3	5.6	3.26	3.03	3.42
Exciton binding (meV)		~15	~27	~80	~21	~60	~26
Intrinsic carrier (cm ⁻³)		10 ¹⁰	10	10 ⁻²⁷	10 ⁻⁷	10 ⁻⁵	10 ⁻¹¹
Breakdown (10 ⁶ V/cm)		0.3	1.8	4	3	3	3.3
Electron mob. (cm ² /Vs)		1300	850	2200	900	600	1050
Hole mobility (cm ² /Vs)		600	40	1600	120	80	30
Saturation vel. (10 ⁷ cm/s)		1.0	2.5	2.0	2.0	2.0	2.0
Relative dielectric const.		11.8	9.6	5.5	10.0	9.7	10

and 6H-SiC, are stable enough and thus of technological interest [25]. The stacking sequences of the most common SiC polytypes are illustrated in Fig. 1.2.2.

There are several different methods to describe a silicon carbide crystal. The method that widely used is the Ramsdell notation [26], where the number indicates the number of bilayers involved in the unit cell and the letter describes the crystal symmetry as H for hexagonal, C for cubic, and R for rhombohedral. The only cubic polytype, 3C, has ABC stacking sequence with

zinc-blend lattice structure. The only pure hexagonal polytype that has wurtzite crystal structure is the 2H-polytype, while the other hexagonal polytypes are mixtures of zinc-blend and wurtzite structures. Among them, the most stable are the 4H and 6H, with corresponding stacking sequences ABCB and ABCACB, respectively. The rhombohedral polytype with the lower stacking sequence ABCBACABACBCACB is the 15R. There is also the possibility for the determination of the hexagonality, h , of a SiC polytype, which is the percentage of the hexagonal sites out of a whole crystal. Since 3C-SiC has only cubic sites, the hexagonality is obviously zero ($h=0$), whereas for 2H where the only site is hexagonal the hexagonality is one ($h=1$). In mixed-structure polytypes, the hexagonality varies between the two extremes. Moreover, the ratio c/a diverges from the ideal of tetrahedral structure (3C-SiC) since the group symmetry is changed and the c -axis may be stretched or compressed in order to increase the cohesion energy of the crystal lattice.

1.3 Applications of SiC

In the recent years, many research activities focus on silicon carbide (SiC) in all over the world. SiC superior properties versus silicon and many other semiconductors make it a promising material for high temperature, high frequency and high power device applications with resistant to harsh environments.

Silicon carbide in its single-crystalline, poly-crystalline or amorphous form has a wide variety of application. Traditionally it is used in high temperature, harsh environment, high-strength applications like abrasive and cutting tools, structural materials, automotive parts, astronomical and nuclear fuel equipment's parts, and steel production. Last decades it is also used in electric systems, electronic circuit elements, graphene production and biotechnology [19, 27, 28].

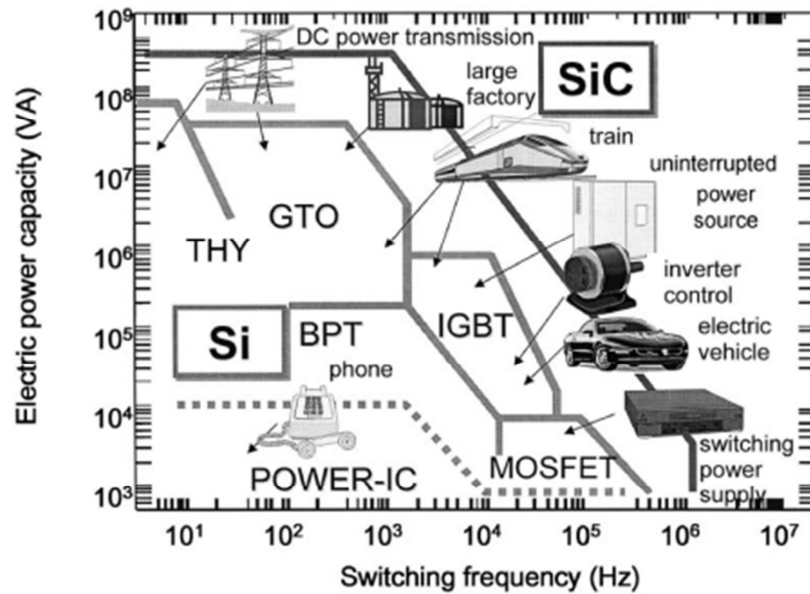


Fig. 1.3.1 Types of power devices.

Silicon carbide (SiC) is a leading alternative to Si in any application in which the environmental temperatures or level of radiation would damage silicon electronics or temperatures and corrosion would damage silicon or polymer sensor elements. SiC, like silicon, is usable as a semiconductor electrical element (Fig. 1.3.1). In addition, it possesses mechanical behavior that is comparable to silicon. At high temperature, silicon dramatically softens and dopants diffuse, changing electrical behavior. Conversely, SiC does not significantly soften even at 600 °C and has a very low diffusivity. SiC is also highly resistive to a wide range of chemicals and can withstand high-temperature oxidative environments. Because of its overall stability of mechanical and electrical properties at high temperatures along with a developed batch manufacturing infrastructure, SiC is poised to open up a host of harsh environment applications to microsystem technology [19]. Such high temperature electronic components and systems can play an important role in many areas, like aircraft, spacecraft, automotive, defense and power systems [29]. The recent trends of SiC applications in equipments and electronic devices are shown in Fig.1.3.2 together with the material improvements on crystal growth. Despite the chemical resistance of SiC, silicon-compatible

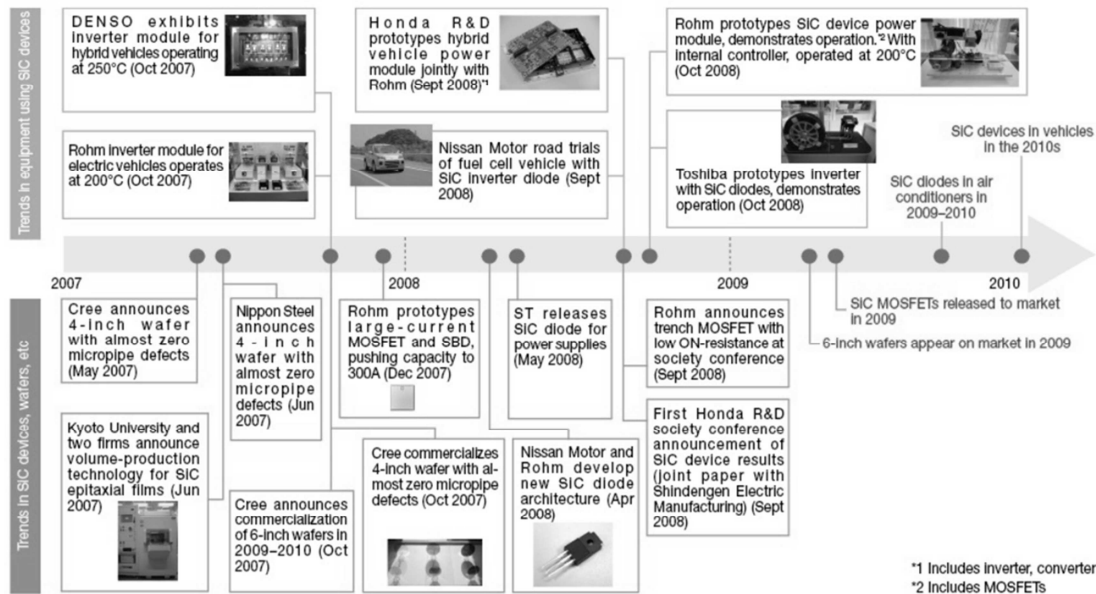


Fig.1.3.2 Evolution trends of the possible application of SiC material as an electronic device.

etching and polishing processes have been developed for SiC. This allows a similar degree of flexibility in layout as silicon or polymer MEMS.

Another important application of SiC is toward high power. Power semiconductor devices are important for regulation and distribution of electricity. Since the efficient use of electricity depends on the performance of power rectifiers and switches, further improvements in efficiency, size, and weight of these devices are quite desirable. SiC has a high breakdown strength and therefore, it needs thinner layers (Fig. 1.3.3) of even higher doping level, for a given blocking voltage compared, with the corresponding Si devices [30]. SiC is emerging as the most viable candidate in the search for a next-generation low-loss element due to its low ON resistance and superior characteristics under high temperatures. As a matter of fact, the power losses can decrease dramatically with the use of SiC-based devices from high efficiency inverters in DC/AC converters for solar/wind power supplies and electric/hybrid vehicles to power inverters for industrial equipment and air conditioners. Another desirable property of SiC for power application is its high thermal conductivity, which can facilitate the heat dissipation during operation. SiC power MOSFETs, diode rectifiers, and thyristors are expected

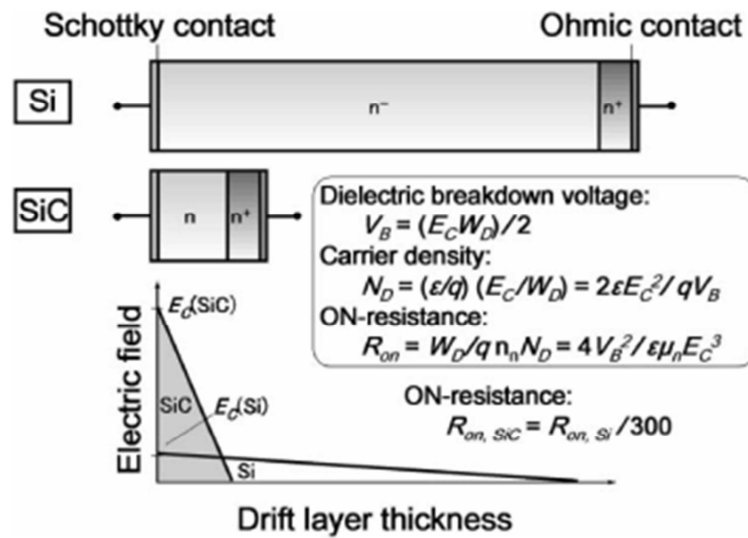


Fig. 1.3.3 Comparison of performance of Si and SiC devices in the case of Schottky diodes [21].

to function over higher voltage and temperature ranges with superior switching characteristics. The sizes of these devices are expected to become significantly smaller compared to correspondingly rated Si-based devices. This is mainly due to the fact that SiC devices will not require heat dissipating components.

1.4 The cubic SiC

The specific interest for the 3C-SiC polytype (variants) is justified by its electrical properties superiority versus its hexagonal counterparts. The only cubic polytype shows high low-field electron mobility, high saturation electron drift velocity, small donor ionization energy and almost an order of magnitude lower state density at 3C-SiC:SiO₂ interface, which are required for obtaining high-performance MOSFETs for power switching applications [31, 32].

First of all, 3C-SiC is the only polytype with isotropic properties due to its cubic crystal symmetry. In addition it is not subjected to micropipe defects formation. From Table 1.1, one can see that 3C-SiC has a larger saturation drift velocity than both 4H- and 6H-SiC polytypes, and is more than twice that of Si, which is advantageous for obtaining higher channel currents in microwave devices [33]. Additionally, among the three most stable SiC polytypes, 3C-SiC

has the highest electron mobility. The carrier mobility influences the frequency response or time response behavior of a device in two ways. First, the mobility is proportional to the carrier velocity for low electric field. Therefore a higher mobility material is likely to have a higher frequency response, because carriers can move more readily through the device. Second, the device current is dependent on the mobility; i.e. higher mobilities result in larger currents. At larger currents, the capacitance will charge more rapidly, which will result in a higher frequency response [34].

An interesting future device application for 3C-SiC is as a metal-oxide-semiconductor field effect transistor (MOSFET) especially in high current and high voltage switching applications. Such application requires small donor ionization energy and low density of traps at the interface between semiconductor and oxide. In hexagonal polytypes the interface state density is high at the SiO₂/SiC interface, which leads to low inversion channel mobility in MOSFET devices. On the other hand, using 3C polytype, these interface states are located inside the conduction band due to its lower bandgap [35]. It should lead to superior inversion channel mobility in MOSFETs. But this also depends on the material quality.

Palyakov et al. [36] has demonstrated theoretically the possibility of high electron mobility transistor (HEMTs) in a hetero-polytype junction β/α (3C/4H or 3C/6H). This study predicted the formation of a two-dimensional electron gas (2DEG) at such interface with superior potential for high electron mobility transistors (HEMTs) than the more widely studied nitride counterpart made of AlGaN/GaN hetero-system [36, 37]. Indeed, some significant benefits are expected using α/β SiC heterostructure due to larger band offset, chemical homogeneity of the interface, superior thermal conductivity and lack of compositional grading. All these advantages offer the possibility to achieve more reliable HEMTs with substantially higher 2DEG sheet densities. However, this 2DEG should only be observed when growing the 3C layer on C-face of α -SiC substrate due to appropriate spontaneous polarization in that direction. Some experimental attempts were made in order to demonstrate such

2DEG but the results were not really conclusive most probably because of the average crystalline quality of the deposited 3C layers [38, 39].

The benefits of 3C-SiC spread across a vast number of domains, from power electronics to chemical sensors, medical applications and biotechnology. There is also a theoretical prediction for the efficiency of solar cells produced from 3C-SiC that might reach the 30% or even higher [40, 41, 42].

1.5 Defects in SiC

The production of crystals with the lowest possible density of defects, as the main task of materials science, is of great importance in the case of semiconductors which are used for electronic applications. Most of the defects act as traps or recombination centers for carriers resulting in devices performance and lifetime reduction. Also, some defects may be multiplied through ageing and extensive operation and progressively degrade the device performances or destroy it. In this paragraph we will account in brief the defects that appear in SiC and especially in cubic polytype.

In general, the defects in a semiconductor are classified in point and extended. As point defects are considered these that include the substitution of a Si or C atom of the SiC matrix by one impurity, or impurity atoms in intermediate position in the crystal matrix, or Si or C vacancies and/or antisite defects. As extended defects are considered the one-, two-, and three-dimensional perturbations of a perfect crystal lattice. The most common one-dimensional defect are dislocations, while two- and three-dimensional defects are stacking faults, grain boundaries, double position boundaries, inversion domain boundaries, and all possible kinds of inclusions, respectively. In 3C-SiC the most common defects extended defects are inclusions of other polytypes, twinned domains and stacking faults.

1.5.1 Point defects

Point defects such as impurity substitution of matrix elements are present in most materials during growth independently of the used growth method. Depending on the application of the grown bulk material or epitaxial layer this doping of impurities can be either intentional or unintentional. Since SiC matrix is made of two group IV elements a V group impurity, that substitutes a Si or C site, has an extra electron that can be excited into the conduction band, and thus it is considered as a donor. The group III impurities, on the other hand, lacking of some electrons are considered as acceptors. The most common donor and acceptor species for SiC are N and P for the n-type materials and B, Al and Ga for the p-type doping. Depending on the size and chemical nature of the atoms, they can substitute more or less group IV atoms in the SiC matrix. Nitrogen and aluminum, having very high solubilities in SiC ($\sim 10^{21} \text{ cm}^{-3}$) substitutes C and Si sites, respectively [43, 44, 45]. Boron, on the other hand, can occupy both sites but is preferentially found on the Si site. All other impurities substitute mainly on the Si sublattice since this induces less lattice distortion and lowers the total energy. Substitutional impurities introduce states in the band gap of the SiC crystal which can be shallow or deep, depending of the impurity, with different binding energies and thus induce changes to the electronic properties of the semiconductor. Moreover, they are responsible for the screening and coupling effects in semiconductor. The first effect is responsible for the reduction of forbidden energy band gap the so called band gap shrinkage. The coupling effect results in degenerate impurity state levels within the conduction band and it is important at very high doping concentrations and at low band gap semiconductors and it is known as Burstein–Moss effect.

The interstitial defects in a crystal occur during the growth of the material or after post growth treatment by atoms of the matrix or impurities and occupy an area in between the atomic positions of the crystal lattice. These atoms do not create bonds with the atoms of the crystal of the semiconductor and are usually not optically or electrically active. Distortions that created in the crystal

lattice can lead to structural imperfections like dislocations or other more extended defects such as stacking faults. Not being anchored in atomic crystal positions they can diffuse in the crystal and interact with another defect called vacancy and be annihilated.

A vacancy in SiC is called the absence of a Si (V_{Si}) or C (V_{C}) atom from the crystal lattice. They are thermally stable at room temperature and far above [46], and since they have strong chemical bonds their mobility is reduced. These defects can be electrically active and affect the electronic properties. They create energy states in the band gap and can be optically identified. The two types of vacancies behave in different manners. The dangling bonds around the V_{Si} are strongly localized at the neighboring C atoms, while Si dangling bonds in the V_{C} vacancy are rather extended resulting in more effective recombination centers [47].

1.5.2 Extended defects

Dislocations appear during the growth, either when solidifying or when undergoing deformation and can be visualized as the insertion of an extra crystal plane in the half part of a perfect crystal. The dislocation can be described by the so called Burgers vector which remains constant during dislocation displacement even turning in a new direction. Dislocations are classified to screw, edge and mixed, depending on the direction of the Burgers vector in relation to the direction of the dislocation line. A dislocation is said perfect when the Burgers vector has the value of a lattice vector. In the case that the Burgers vector of the dislocation does not coincide with a lattice vector then it is called a partial dislocation. Even though in most cases the dissociation of a dislocation into two dislocations with smaller Burgers vector can reduce the elastic strain energy, it usually creates a fault in the crystal structure with higher energy. In thin layers there have been observed dislocations that start from the interface of the layer and the substrate and finish at the surface of the layer or an interface inside the layer. These dislocations differ from the other dislocations only in the direction of their

motion, as they climb in the layer instead of gliding in the slip planes. For this reason they can be threading edge dislocations (TED), threading screw dislocations (TSD) or threading mixed dislocations (TMD). They can be observed on the surface as points and only in the cross section of the layer the typical line shape of the dislocation can be seen. These dislocations are of great interest for electronic applications since more device structures are constructed on the surface of the layer and utilize the material near the surface. Since most dislocations are near the interface, they have no impact on the operation of devices. If there is a high density of threading dislocations reaching the surface of the material it is obvious that they will degrade the electronic properties of the device [48].

Stacking faults (SFs) are created by a disruption in the normal stacking sequence of the atomic levels and they are the most common and simplest two dimensional structural defects that can appear in the crystal structure of materials that have a closed packed structure. In the fcc crystals like SiC two kinds of SFs can be created, intrinsic or extrinsic. As a SF is created in the [111] crystallographic direction of the crystal if the stacking of the closed packed structure is altered from the normal ABCABC sequence. In the case of the intrinsic SF it can be considered that it is created by removing one atomic layer from the stacking sequence that can come by the concentration of vacancies in the crystal structure or slipping of the atomic planes due to shear stress. The extrinsic SF can be created by adding an atomic layer in between two stacking sequences. This can be caused by the introduction of excess atoms during growth in interstitial positions. In both cases the SFs are bordered by partial dislocations which are linked either with extrinsic/intrinsic SFs or vacancies. In the case of 3C-SiC, with cubic closed packed (ccp) structure in the $\langle 111 \rangle$ crystallographic direction of an fcc crystal, SFs play an important role in the quality of the electronic devices produced out of SiC. The electrical characteristics of these devices degrade over time by the increasing of the forward threshold electrical potential when applying a steady current [49, 50]. There have also been studies that exhibit the behavior of SFs as quantum wells

in the hexagonal polytypes [49, 50, 51] and are responsible for the deterioration of the electronic devices. The energy difference of the conduction band of the cubic polytype in respect with the hexagonal is quite large while the respective differences in the valence bands is of the order of 1/10 of the differences in the conduction bands. On the other hand, if the opposite is considered, having SF or an inclusion of a hexagonal polytype inside a 3C-SiC matrix, then there is no trapping of conduction band electrons, since the inclusion is behaving energetically as a barrier [49, 50, 52]. What is noteworthy is that in no other semiconductor, SFs were found to be linked so clearly with the creation of quantum wells [50, 53].

Another effect of polytypism of SiC is the appearance of transition layers during the growth. Some times in the initial steps of the growth of one polytype on top of another, as is the case of growth of the cubic polytype on top of hexagonal substrates, there have been observed a transition step of a homoepitaxial layer and then achieving the cubic polytype. In some other cases this happens with an addition of another polytype, just after the homoepitaxial step, that has a smaller band gap than the substrate polytype but higher than the cubic polytype, before finally reaching the cubic polytype [48].

Twinning occurs in crystal lattices during growth or by mechanical deformation. In this case the crystal is composed of parts of the same structure with different orientation with respect to one another. Every part is a monocrystal and each part can be derived by following certain symmetry rules. The stability of a crystal depends on the collection of atoms forming it to have the lowest possible free energy. The pattern for this is the atoms assuming the positions of the perfect crystal lattice and any deviation from that, would lead to higher energy states. The twin boundary interface is one such interface of higher energy. The intergrowths that created and taking into account that they do not arise independently of one another, the orientations with the highest probability of occurring are those that have the greatest number of structural elements in common. In this way their structural relationship had reduced interfacial energy. The greater the number of atoms in the region of the

interfacial plane which participate normally in the bonding of the two structures, the less abrupt is the discontinuity. That leads to lower energy, and consequently a more probable structure. The most probable intergrowths are those in which, all atoms of the structure in the region of the junction bridge the junction.

One way to describe twin boundaries and grain boundaries is the coincidence site lattice (CLS) approach. In order to use this approach it is considered that the two grains are overlapping. When they are mismatched by certain angles a Moirée pattern can be formed and some of the lattice points of one grain coincide exactly with some lattice points of the other grain and a CSL superstructure is created. It should be mentioned that there is no actual overlapping of the lattices, since lattices cannot actually overlap. If there are many points of coincidence the boundary is quite smooth and has a low energy. This is called a coherent boundary. On the other hand if there are not many coincidence points then the energy of the boundary is quite high and in order to reduce this energy it can create faceted boundaries in more than one crystallographic direction. These are usually called incoherent boundaries. Depending on the angle, the points of coincidence and if the twin boundary is coherent or not, there can be low energy and high energy CSLs. The relation between the number of lattice points in the unit cell of a CSL and the number of lattice points in a unit cell of the generating lattice is called Σ (sigma). It is the unit cell volume of the CSL in units of the unit cell volume of the elementary cells of the crystals. Usually twin boundaries have a $\Sigma 3$ CSL. The clearest indication that low Σ boundaries are preferable comes from innumerable observations of a different nature altogether – the observation that grain boundaries very often contain secondary defects with a specific role. This role is to correct for small deviations from a special low Σ orientation. For the cubic SiC case Σ is always odd [48].

Chapter 2 Growth of 3C-SiC

Cubic silicon carbide (3C-SiC), one of SiC polytypes, is a promising material for power semiconductor devices. Due to lack of suitable bulk growth technique of this material, several techniques have been proposed. Each technique has merits and drawbacks and all grown crystals have significant density of defects. These defects make intrinsic material properties blind. In general, kinds and densities of defects are different in crystals grown by different techniques. In the framework of MANSiC project I have investigated several samples been grown by different techniques which have been elaborated for thin layers and bulk 3C-SiC crystals. These techniques are the follow:

- Vapor Liquid Solid deposition (VLS)
- Chemical Vapor Deposition (CVD)
- Sublimation Epitaxy (SE)
- Continuous Feed Physical Vapor Transport (CF-PVT)

Complementary, HOYA CVD technique for bulk 3C-SiC is reported. In the next paragraphs a rough description of these techniques is presented.

2.1 Vapor Liquid Solid deposition (VLS)

The VLS deposition concept was initially [54] proposed in order to explain the unidirectional SiC whisker growth catalyzed by impurities. This growth process by VLS mechanism can be described by four consequent steps: (a) transport of the gaseous precursors to the surface of the liquid, (b) cracking of the precursors and dissolution of carbon and silicon in the liquid at the vapor-liquid (VL) interface, (c) transport of Si and C from the VL interface to the liquid-solid (LS) interface, and (d) crystallization of SiC at the LS interface. Although VLS mechanism is now frequently used to grow SiC nanowires [55], the growth of epitaxial films faces several difficulties. The implementation of the process which requires covering completely the seed makes impossible the

use of pure metal catalyst like for whiskers. The high reactivity of pure metals when they are in contact with SiC substrate is reduced with the highly recommended use of metal-Si alloys so that there is no need to add Si precursor in the gas phase. In addition, the liquid amount that is required reduces the diffusion of active species and hence results in lower growth rates. This is obvious to the achieved higher growth rates at the susceptor edges [56]. The experimental setup was composed of quartz, water-cooled vertical cold-wall reactor. The temperature of the radio-frequency (RF) heated graphite susceptor was controlled by an optical pyrometer. High-purity Ar was used as the carrier gas with propane (C_3H_8) as the reactant (Fig. 2.1) [56].

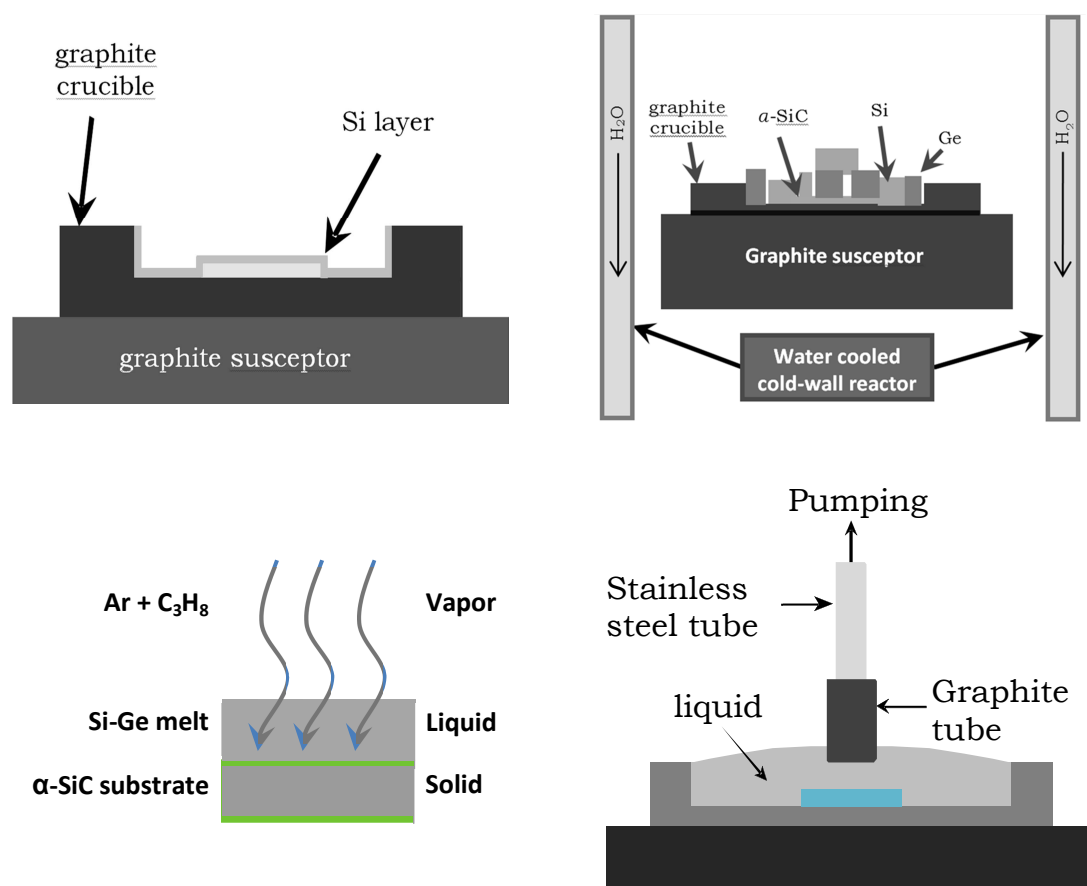


Fig. 2.1 Graphical representation of vertical cold-wall reactor (left) and VLS growth mechanism principle (right). (From [56])

The layers of 3C-SiC are grown on (0001) 6H-SiC wafers at the (111) direction where the lattice mismatch is minimized. In order to achieve identical

growth conditions, i.e. complete coverage of crucible's interior and hence wetting optimization, a thin Si layer is deposited inside the crucible by silane (SiH_4) in argon (Ar) ambient at 1000°C for 30 min (Fig. 2.1(a)). Then, the alloy elements in respective composition are set in the interior of the crucible after their cleaning procedure (Fig. 2.1(b)). Si, Ga or Ge, and Al in appropriate proportions are the elements that are commonly used in order a Si-(Ge/Ga)-Al melt to be formed above α -SiC substrate when temperature rises with Ge or Ga rich liquid to be desirable during the initial nucleation procedure with C atoms from cracked propane (C_3H_8) in Ar carrier gas (Fig. 2.1(c)). As an example, 6H-SiC substrate is covered by a $\text{Si}_{25}\text{Ge}_{75}$ melt which is fed by 5 sccm of C_3H_8 diluted in 5 slm Ar. The 3C nucleation step is performed at 1450°C for 5 min for twin defects elimination, followed by a 55 min growth at a lower temperature (1200°C) in order to limit Ge evaporation. This results in a growth rate in the $1\text{-}3\ \mu\text{m/h}$ range.

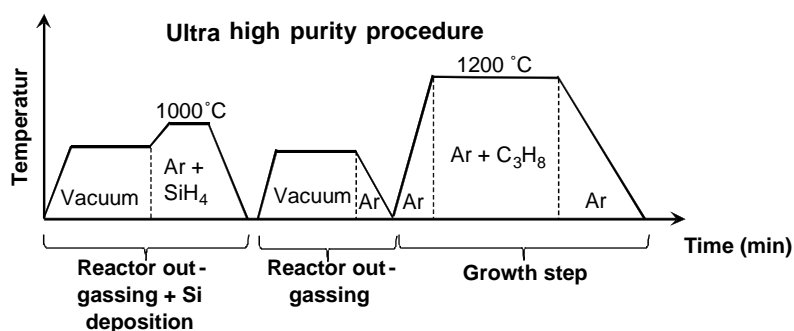


Fig. 2.2 Growth procedures used for ultra-high purity procedure. (from [56])

In order to reduce the nitrogen incorporation inside the VLS grown layers, only the pre-growth step is modified. First, small pieces of Zr-Ti alloy are placed beside the crucible (so that they are also heated) to act as N getter. Second, after the introduction of the sample inside the growth chamber, a prolonged pumping is performed at room temperature for several hours. Then, the temperature is increased to 860°C and is kept constant under active pumping in order to increase the out-gassing efficiency. The out-gassing conditions are chosen in such a way that they don't affect the subsequent 3C-

SiC deposition step. That is why the temperature never exceeded Ge melting point in order to maintain identical nucleation conditions. The third procedure is basically identical to high purity procedure except the addition of a crucible out-gassing step at 1000 °C under vacuum before the Si deposition. It is called “ultra-high purity” (UHP) procedure and is summarized in Fig. 2.2.

At the end of the experiments, the melt was sucked out by dipping a graphite tube, connected to a pump, into the top of the melt (Fig 2.1(d)). The remaining Si–Ge alloy inside the crucible was eliminated by wet chemical etching in HCl–HF–HNO₃.

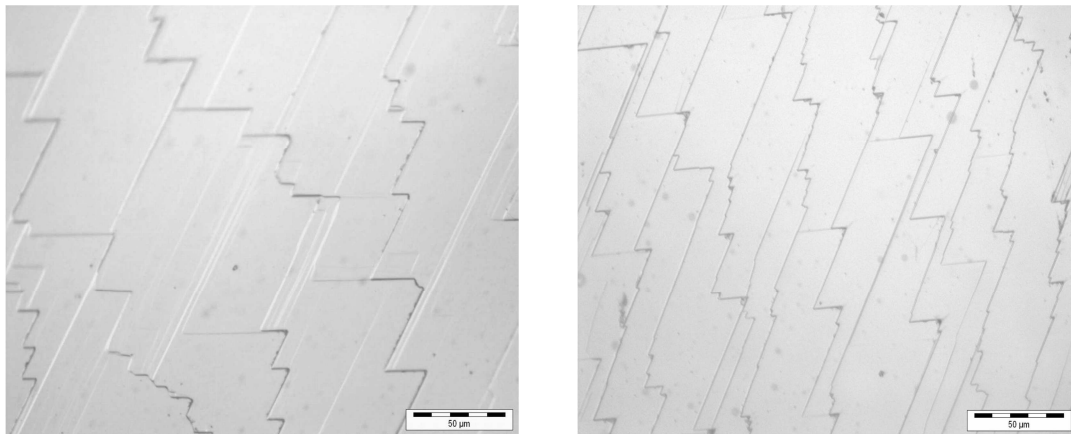


Fig. 2.3 Optical morphology of (111) 3C-SiC layers grown by VLS on (0001) 6H-SiC substrate using a) a standard and b) a high purity VLS procedure.

In Fig. 2.3 is illustrated the morphology of the 3C-SiC layers grown by VLS mechanism using the two different procedures. Both layers present identical step bunched surfaces with jagged step front. This is typical of single-domain 3C-SiC layers grown with the VLS technique. The main conclusion is then that the layer quality is apparently not affected by the procedure changes. On the other hand, in "High purity VLS" samples the nitrogen doping level is detected to be an order of magnitude lower than the samples grown by the standard VLS procedure.

2.2 Chemical Vapor Deposition (CVD)

2.2.1 CVD on VLS seed layer

The VLS growth procedure results in limited layer thickness of 1-3 μm because of liquid loss through evaporation and/or spreading. In order to obtain thicker 3C-SiC layers and to control the doping level CVD homoepitaxial growth is used. The experimental setup is composed of a vertical, cold-wall CVD reactor similar with VLS one. The precursor gases are silane (SiH_4) and propane (C_3H_8) diluted in H_2 at atmospheric pressure [57]. The temperature of the inductively heated graphite susceptor was controlled by an optical pyrometer. The 3C seeds were 3C-SiC(111) layers grown by VLS mechanism on top of 6H-SiC (0001) Si-face, on-axis substrates. Prior to the growth, the seeds were cleaned first by acetone and then by methanol in ultrasonic bath for 10-15 min, before being dried under Ar flow.

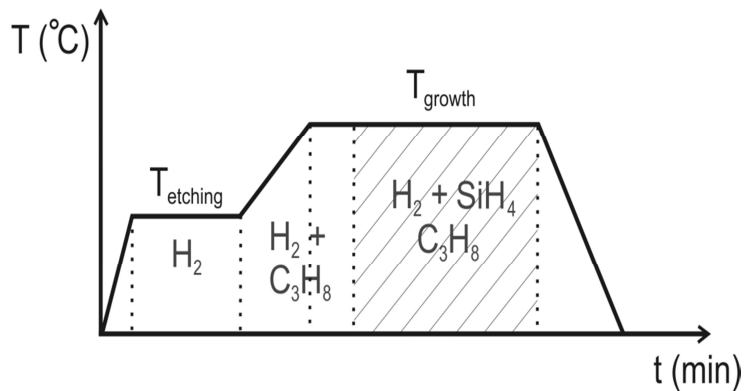


Fig. 2.4 Homoepitaxial growth procedure used on the 3C-SiC VLS seed.

The growth procedure begins with in-situ desoxydation/cleaning of the VLS seed at 1200°C under H_2 for 5 min. Then the temperature is increased up to the growth temperature ($1450^\circ\text{C} < T_{\text{growth}} < 1650^\circ\text{C}$) in 2 min under $\text{H}_2 + \text{C}_3\text{H}_8$. This gas mixture is kept during 5 min at T_{growth} before adding SiH_4 to start the epitaxial deposition for 1 up to 3 h with growth rate $\sim 3 \mu\text{m/h}$ (Fig. 2.4). The surface morphology of the samples was characterized by Nomarski interference microscope as in Fig. 2.5 one can see for low temperature growth.

Here a pronounced step-bunched morphology appears with rather different macro-structure [56].

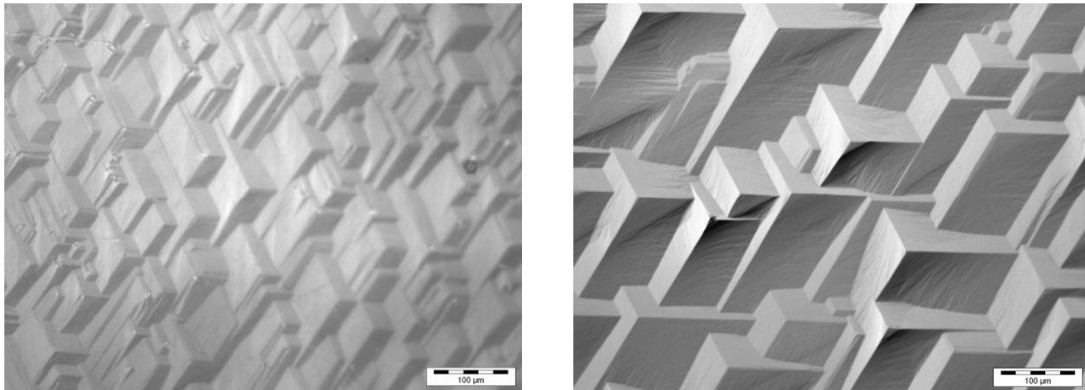


Fig. 2.5 Surface morphology after CVD homoepitaxial growth on top of VLS samples.

2.2.2 CVD on undulant Si

The growth technique of 3C-SiC by CVD on undulant Si substrates is introduced by HOYA company [58]. The schematic is shown in figure Fig. 2.6. Advantages of this technique are elimination of anti-phase boundaries by growth on off-axis Si (001) face (flat parts of the undulation) and stacking faults (SFs) by growth on off-axes with opposite directions (face-to-face flat parts of the undulation) [59]. By this technique, single crystal thick 3C-SiC can be obtained and etching of Si substrates after the growth enables to make free-standing 3C-SiC. The obtained grown layers by this technique still have considerable density of SFs. SFs parallel to the undulation ridge (the [-110] direction) vanish as increase of 3C-SiC thickness as shown in Fig. 2.6(right), because they are narrowing with growth progress. On the contrary, SFs perpendicular with the undulation ridge expand with increase of 3C-SiC thickness. These SFs are parallel to the [110] direction and their density is also decrease with increase of grown thickness due to termination of them by other SFs. As shown in Fig. 1b, there are two inclinations for SFs parallel to the [110] direction. Two SFs with different inclinations can collide with each other

and one of them is terminated by another SF. Typically, 3C-SiC grown on undulant Si substrate have thickness of 150-400 micrometer and 3C-SiC with such thickness has SFs of $10^3 \sim 10^4 \text{ cm}^{-1}$ [60, 61].

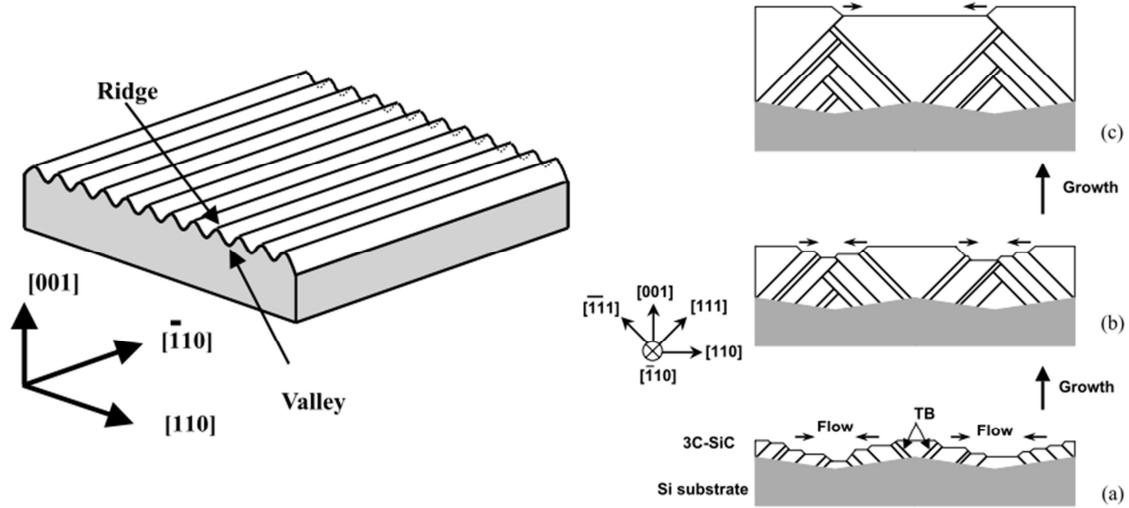


Fig. 2.6 (Left) Schematic structure of the surface of ‘‘Undulant-Si’’. (Right) Model of the elimination of TBs in the 3C-SiC layer on ‘‘Undulant-Si’’ with 3C-SiC growth. The (-111) cross-sectional structure of 3C-SiC changes from (a) to (c) as growth progresses. (After [62])

It has been reported that SFs in 3C-SiC behave as carrier scattering defects. Nagasawa et al. have reported difference of the electron Hall mobilities between the [110] and [-110] directions [3]. The mobility parallel to the [110] direction which is the same direction as high density of SFs is higher than that parallel to the [-110] direction. This indicates that when electrons go across SFs they are scattered resulting in low mobility [62].

2.3 Sublimation Epitaxy (SE)

The sublimation epitaxy method has shown great promises for growth of hexagonal 6H and 4H-SiC layers, as well as cubic SiC. The low cost and high growth rate, in combination with high structural quality and smooth surface morphology, would be beneficial for the fabrication of device-quality

materials. An increase of the productivity and throughput would have a viable advantage for eventual technological developments [63].

The sublimation epitaxy (Fig. 2.7) was realized in a vertical quartz reactor with water cooled stainless steel flanges. The growth was performed in a graphite crucible mounted inside thermally insulating graphite foam and heated by an inductive coil using a RF generator operating at approximately 40 kHz. The temperature was measured on the top and the bottom of the crucible with two-color pyrometers. The temperature gradient was varied by changing the relative positions of the RF coil [64].

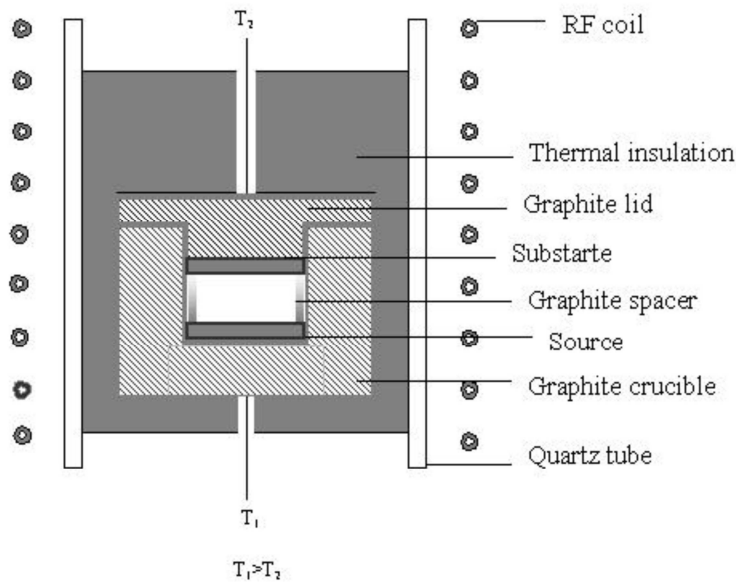


Fig. 2.7 Schematic view of sublimation epitaxy technique. (After [64])

Growth on well-oriented (on-axis) substrates of hexagonal polytypes yields 3C–SiC due to lack of the memory effect of the substrate stacking sequence. The lattice and thermal mismatches between 3C–SiC and 6H–SiC are very small, which is greatly advantageous compared to using silicon substrates. However, the 3C layers grow via two-dimensional nucleation mechanism, which results in extended defects at the nuclei coalescence. More importantly, due to the existence of two possible stacking sequences along the (0001) in the cubic phase, specific defects, double-position boundaries appear in the grown material. Deep insight of the initial stage of heteroepitaxial growth is necessary to minimize these structural defects. Moreover, knowledge about the formation of 3C on hexagonal structure substrates may be beneficial

for growth of 3C inclusion-free 6H-SiC or 4H-SiC homoepitaxial layers. Different temperature ramp-up schemes provide different nucleation conditions. This was applied only to hexagonal substrates, since 3C formation on cubic substrates has a homoepitaxial character. Since 3C-polytype is the first to form under conditions of high supersaturation and Si-rich vapor phase, the most critical phase of the growth process is to allow a complete coverage of the substrate surface by nucleus coalescence without inclusions of the substrate polytype. A change of the initial temperature ramp-up influences the supersaturation condition, for example, a faster ramp-up is expected to give higher supersaturation and, as a result, an increased number of growth centers. By further expanding laterally, the growth centers formed domains of 3C-SiC over the whole substrate surface. As the growth proceeds, the domains grow larger, and the large ones overgrow the small ones (Oswald ripening). Assuming such a mechanism of the layer growth, it is obvious that the initial supersaturation (number of growth centers) and the lateral growth of domains (species surface mobility) are equally important. From this viewpoint, slow ramp-up is preferable because it favors domain enlargement. [63]

For thin layer growth the procedure is performed in a sublimation sandwich system at source temperature of 2000°C with 95 min ramp up from 1200°C and a temperature gradient of 6-8 °C/mm. The growth takes place under vacuum conditions ($<10^{-5}$ mbar) for 30 min [64].

For bulk material growth the procedure is performed in a growth chamber with close space sublimation geometry with inductively heated graphite crucible. The distance between the source and the substrate is 1 mm and the growth takes place under vacuum (base pressure $<10^{-5}$ mbar). The vapor composition (Si/C ratio) and the supersaturation in the growth cell are controlled by three parameters: the temperature difference between the substrate and the source, the C-getter and the utilization of 3C-SiC polycrystalline source material. The experiments were performed at a growth temperature of 1775°C, growth time 30 min and a temperature ramp-up 5 K/min.

2.4 Continuous Feed - Physical Vapor Transport (CF-PVT)

Although the possibility to obtain high quality 3C-SiC was achieved [65] the size of crystals with the use of conventional PVT method was limited. Continuous feed-PVT is a sophisticated technique that offers the intrinsic advantage of combining both the maturity of PVT for single-crystal growth and high temperature CVD for continuous feeding of the high purity polycrystalline SiC source [66].

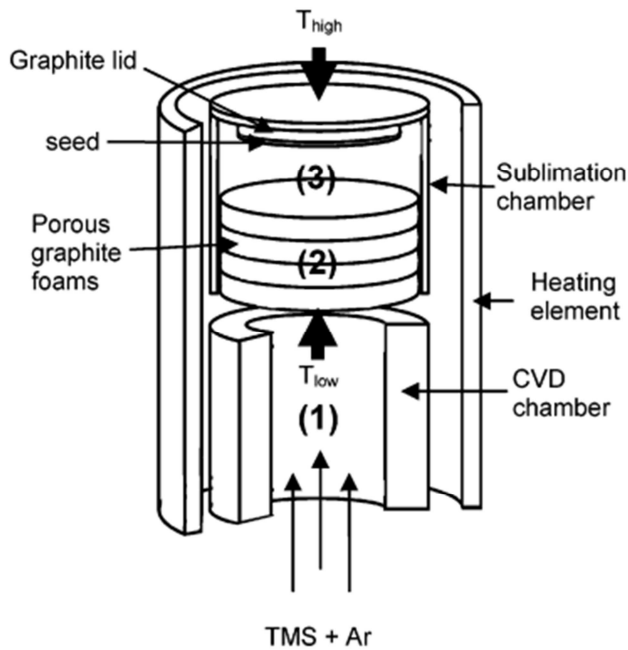


Fig. 2.8 CF-PVT crucible setup. Pyrometric measurement. (1) Feeding zone, (2) transfer zone, and (3) sublimation zone.

The experimental setup is a modified sublimation reactor, with inductive heating and a water-cooled quartz tube [67]. The crucible is totally made of graphite and thermally insulated with graphite felts. A schematic representation of the crucible is presented in Fig. 2.8. It is composed of three main graphite pieces: the heating element, the sublimation chamber, and the CVD chamber, which delimitate the three “reaction zones”. (1) The first one is the feeding zone where the polycrystalline source is formed from tetramethylsilane (TMS) diluted in argon. (2) The second one is the transfer zone consisting of highly porous graphite foam, which supports the CVD deposit and allows SiC transfer to the sublimation area. (3) The third one is the sublimation zone containing the SiC seed stucked on the top of the crucible.

The crucible is indirectly heated as the maximum power dissipation from the induction coil is reached in the heating element. The three reaction zones are thus mainly heated by radiation and convection phenomena. During the process, the monitored parameters are temperature, pressure, and gas flow rates. The growth pressure is always lower than 5 mbar.

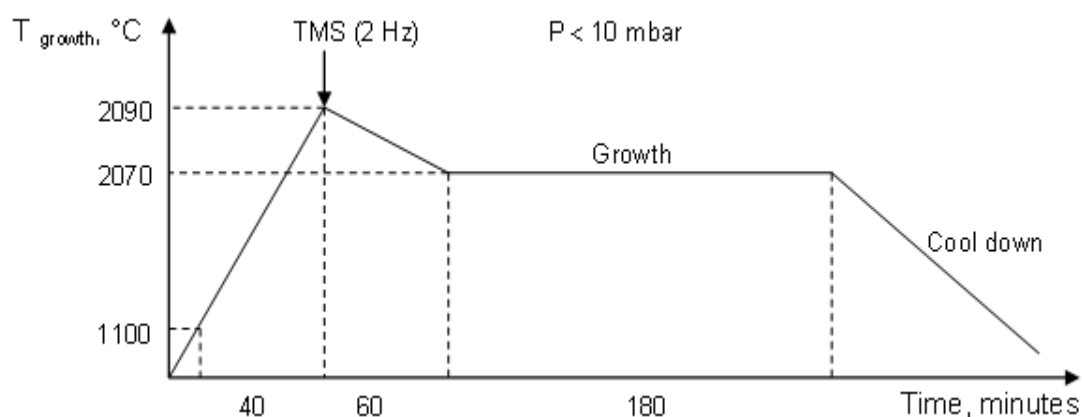


Fig. 2.9 Typical CF-PVT growth procedure. (After [68])

Temperature measurements are performed by optical pyrometers on the top of the crucible (T_{high}) and on the graphite foam in the feeding area (T_{low}). The temperature monitoring is linked to T_{high} . This study was carried out in a temperature range varying from 1850 to 2050 °C (T_{high}). The argon flow rate is 400 sccm. Different TMS flow rates from 16 to 64 sccm, corresponding to TMS/Ar ratios of 0.04 and 0.16. In the following, we will refer to the TMS/Ar ratio. This system could lead to the best SiC deposition yield at high temperature in the CVD area. The use of chlorinated precursors is promising for the CVD step but appeared to be very harmful concerning the SiC transfer by sublimation in both the transfer zone and the sublimation zone. The transfer zone is composed of four similar pieces of graphite foam stacked one over the other. The porosity of the foam is about 97%. The graphite foams are numbered 1 to 4; 1 is the lower foam, which is fed by the CVD step, and 4 is the upper one (Fig. 2.9).

Chapter 3 Carrier Dynamics and optical time-resolved techniques

The characterization of fast electronic properties in semiconductor technology is based in the study of their carrier dynamics. Nonlinear optical techniques of active spectroscopy, in comparison with electrical ones which are limited due to their ohmic conducts and slow response, have the ability to analyze electrical processes by optical nondestructive means since they are based on strong correlation between electrical and optical phenomena.

Since lasers with short and powerful pulses at various operating wavelengths were available, all excitation-dependent material properties are considered as optical nonlinearities. Short pulse lasers allow monitoring of charge carriers motion, creation and annihilation by means of both absorptive and refractive optical nonlinearities on picosecond and femtosecond time-scales. Charge carriers motion can be driven by either the application of an electric field or the creation of a concentration gradient that obeys both quantomechanical and classical laws. Thus, nonlinear optical techniques of active spectroscopy are presented as a bridge between the optical and electronic semiconductors properties as, based on strong correlation between electrical and optical phenomena, potentially they are able to analyze electrical processes by optical means.

The extremely small photon–photon interaction cross-section (10^{-65} cm^2) makes the direct mutual interaction of two light means practically negligible; thus the linear superposition of light is fulfilled in all practical cases. Therefore, any potential nonlinearity is achieved via the nonlinear interaction of light with matter. In this case, both the real and imaginary part of complex refraction index – or else, refractive index n and absorption coefficient α – are now functions of their light intensities I . Even the general description of nonlinear interactions of light with matter based on quantum electrodynamics, this is possible only in the simplest cases with the use of approximations. In a general classification we can classify them in matter resonant (with absorption) or non-resonant (without absorption) interactions with coherent or incoherent

light. In order to describe the non-linear interaction of light with matter – or more precisely for the initial nonlinear modification of matter by light and the subsequent linear response of the changed matter to the light – one can consider three different approaches [69]. In the first case it is used the nonlinear polarization concept based on Maxwell's equations which is useful especially for nonresonant (elastic) interactions in which the light is not absorbed by matter. The second approach for resonant (inelastic) and coherent interactions is based on quantum mechanical density matrix formalism. Though, this formalism is useful for cases with mater structure with discrete energy levels and their phase-dependent occupation during the light wave period, it is not relevant for systems with many energy levels and/or complex light fields. For the description of this last case a third approach where one has to neglect the coherence terms in the density matrices that results in rate equations for the population densities. Besides these well defined cases all kinds of mixed interactions are possible.

In general, if matter is exposed to an intense light flux, resonantly or non-resonantly, nonlinear effects are taking place simultaneously. In the case that matter shows some absorption at incident light beam's wavelength, with absorption coefficient higher than about 10^{-6} cm^{-1} , the share of the non-resonant nonlinear interaction can be neglected. In this case, the mechanism of light-induced changes of optical materials properties is often described by two steps. Initially, the light produces some material excitation which then leads to a change of the optical properties. According to the quantum mechanics, the phase of the light wave that produces the resonant transition from ground to excited state is stored in the relative phase of the wave functions of the two states [70]. The phase relaxation time of excited state usually is much shorter than the decay time of the excited population of the material. Hence, in materials with non-negligible light absorption coefficient the wave signature of excited population is disappeared practically just after the disappearance of operative event, i.e. the excitation light beam. Thereafter, the excited

population is the dominant factor for the changes in material's optical properties.

3.1 Free carriers in semiconductors

As free is defined a carrier being in the vacuum, i.e. without any interaction with its environment. Free carriers in matter are facing complex electric fields formed by lattice ions and other charged carriers of the neighboring atoms. In the base of semi-classical Drude theory, initially applied in metals, free carriers can move “freely” only between two successive elastic collisions with lattice atoms experiencing the matter's complex field. In the case of semiconductors, free carrier is considered an electron (hole) which is not bound to a lattice site, being in conduction (valence) band and so it accelerates under an electric field.

Free carriers in bands can exist through several procedures. When a light beam with photon energy that exceeds the forbidden energy gap of semiconductor is absorbed an electron-hole pair is generated via band-to-band transitions. Lower photon energy beams can generate carrier population in bands via photoionization of deep impurity levels present in energy gap of semiconductor as well. It is also worth to mention that thermal excitation of shallow impurities can create a carrier population in respective bands as temperature increases. In Drude theory a free charged particle is oscillating in the external electrical field of exciting light. The damping of oscillations is inversely proportional to carrier relaxation time which describes the mean time between carrier scattering events. Taking into account a high frequency of optical excitation, Drude theory gives the following expressions for changes of absorption coefficient $\Delta\alpha$ and refractive index Δn , respectively:

$$\Delta\alpha = \frac{\Delta N e^2}{n_0 m_r \omega^2 c \tau_d \epsilon_0} = \Delta N \sigma_{eh} \quad (3.1)$$

$$\Delta n = -\frac{\Delta N e^2}{2n_0 m_r \omega^2 \epsilon_0} = \Delta N n_{eh} \quad (3.2)$$

In Eq. (3.1) and (3.2) ΔN stands for electron-hole concentration, e is the electron charge, n_0 is the refractive index of crystal, ω is the circular frequency of the light wave, ε_0 is the permittivity of vacuum, m_r is the reduced electron-hole pair effective mass, and τ_d is the carrier relaxation time. σ_{eh} and n_{eh} are the one electron-hole pair induced change of absorption and refraction index, respectively.

The description of the behavior of charged carriers in semiconductors is one of the keys of their understanding. Charge carriers mobility and lifetime are among the most important parameters that characterize a semiconductor because they are a sensitive measure of material quality, which in turn, determines device performance. In the following section we will present the principles of motion and recombination for free carriers and their dependence on temperature and concentration, as well as, in semiconductor impurities. We will focus on the *high carrier density*, but below the critical degeneracy concentration of Mott phase transition. We will consider them in the *low electric field* transport regime.

3.2 Carrier dynamics

3.2.1 Carrier transport

Charged carriers in a semiconductive material are able to move as if they were free particles with an effective mass. The cause of it can be an external electric field or a carrier concentration gradient. In the first case we speak about drift carrier mobility and in the second about diffusion mobility. Apart from this, both of them, in the low electric field regime, obey to the same rules. The case of our interest, as a matter of fact, has to deal only with internal negligible electric fields between opposite sign carrier distributions and opposed to their separation - the Debye field. The diffusion process is described by Fick's law with the ambipolar diffusion coefficient D_{amb} to be related to ambipolar carrier mobility μ_{amb} via Einstein's relation:

$$D_{amb} = \frac{k_B T}{e} \mu_{amb} \quad (3.3)$$

Mobility, in turn, is expressed as a linear function of average relaxation time $\langle \tau \rangle$ due to scattering mechanisms (discussed earlier) over the carrier distribution as:

$$\mu_{amb} = \frac{e}{m^*} \langle \tau \rangle \quad (3.4)$$

Since both types of photogenerated carriers are propagating together their ambipolar diffusion coefficient is expressed as a function of their concentration (n, p) and diffusion coefficients (D_n, D_p):

$$D_{amb} = \frac{n + p}{\frac{n}{D_p} + \frac{p}{D_n}} \quad (3.5)$$

For high-level injections ($n \approx p \approx \Delta N$) the ambipolar diffusion coefficient is written as:

$$D_{amb} = 2 \frac{D_n D_p}{D_n + D_p} \quad (3.6)$$

If $D_n \gg D_p$, as it happens in the case of 3C-SiC, then $D_{amb} = 2D_p$. On the other hand, at low-level injections (below the doping level) D_a is approaching the minority carrier diffusion coefficient (Fig. 3.2.1). We can conclude that

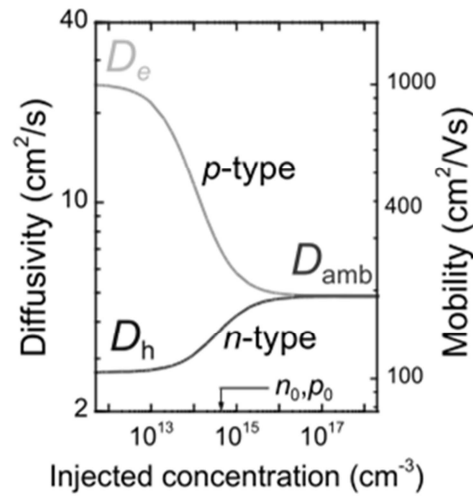


Fig. 3.2.1 Dependence of the carrier diffusivity on excitation density. (After [71])

while minority carriers establish the diffusivity at low-level injections, the carriers with the lower diffusion coefficient (usually holes) dominate the ambipolar case at high-level injections.

3.2.2 Carrier scattering mechanisms

In a semiconductor crystal several different distinguishable charge carriers scattering mechanisms are operating. From now on we consider that charge carriers are represented from electrons. If there is not any interaction between their scattering rates, we can write the net relaxation time according to Matthiessen's empirical approximation rule as:

$$\frac{1}{\tau} = \sum_i \frac{1}{\langle \tau_i(E) \rangle} \quad (3.7)$$

where index i refers to the different scattering mechanisms. Since mobility is direct proportional to relaxation time, we can express it in analogy of Matthiessen's rule. In a general consideration we can distinguish the scattering mechanisms in thermally-induced and residual. The former is describing an ideal crystal, i.e. unperturbed band structure, and is dependent only from temperature. The latter is the consequence of all entities – impurities, defects – present in the host ideal crystal, and apart from temperature is depended from their concentration. More specific, with dependence of the scattering centers, one can categorize them in: a) phonon scattering, b) coulombic interaction, c) interaction with neutral defects, and d) transport in multivalley semiconductors, intervalley scattering.

Phonon scattering be distinguished in acoustic and optical phonon scattering. Acoustic phonons can interact with electrons elastically via deformation potentials or piezoelectric fields. In this case, mobility as a function of temperature is $\mu_{ac} \propto T^{3/2}$ and $\mu_{pe} \propto T^{1/2}$ for deformation potential and piezoelectric field, respectively. Optical phonons can interact with electrons non-elastically via deformation potentials or polarization fields resulting in mobility $\mu_{opt.def.} \propto T^{-5/2}$ and $\tau_{pol.opt.} \propto \exp(\Theta_D/T)$, respectively, for temperatures

well below Debye temperature Θ_D . All phonon related mechanisms become the dominant scattering mechanisms as the temperature increases (typically at and above room temperature).

When the scattering occurs on charged entities, the electrons interact with Coulombic potentials at relatively long ranges since the scattering cross section is in the order of 10^{-13} cm^2 . Theoretically, this problem is treated similar to Rutherford scattering considering a screened Coulomb potential. Mobility in the case of ionized shallow impurities is $\mu_{\text{ion}} \propto T^{3/2}$ and is decrease inversely with the density of scattering centers as Conwell–Weisskopf (classical) and Brooks–Herring (quantum mechanical) models treating [72].

The scattering at dislocations shows relaxation time (or mobility) proportional to temperature, while the scattering on other carriers (electrons or holes) has no significant influence. Since dislocations can contain charge centers they can act as scattering centers. The deformation has introduced acceptor/donor-type defects reducing the mobility in particular at low temperatures (similar to ionized impurity scattering). The temperature dependence of mobility due to dislocation scattering in a semiconductor is given by $\mu_{\text{disl}} \propto T$ [73].

Scattering on neutral lattice defects become important at low temperatures due to free carrier freeze-out and it depends from the size of scattering centers and their concentration, but, it has no temperature dependence. In fact, ionized and neutral impurities are the two faces of the same entity; their concentration are temperature depended since free carriers ionization is a temperature depended effect.

Intervalley scattering has a significant influence in indirect gap semiconductors because they have several satellite minima at the conduction band edge at different crystallographic directions. Phonons with sufficient energy (mainly optical) can provoke intervalley scattering processes resulting in relaxation time reduction. Since, it is governed mainly by optical phonons scattering its temperature dependence has similar behavior with optical phonons.

The lowering of mobility due to transport across grain boundaries is an important effect in polycrystalline and highly defected materials. Since grain/domain boundaries contain electronic traps their filling depends on the doping of the bulk of the grains/domains. Charges will be trapped in the grain/domain boundaries and a depletion layer will be created. At low doping the grains/domains are fully depleted and all free carriers are trapped in the grain/domain boundaries. This means low conductivity, however, no electronic barrier to transport exists. At intermediate doping, traps are partially filled and the partial depletion of the grain/domain leads to the creation of an electronic barrier hindering transport since it must be overcome via thermionic emission. At high doping the traps are completely filled and the barrier vanishes again. Accordingly the mobility goes through a minimum as a function of the doping concentration. The expression for the limitation of the mobility due to scattering at grain boundaries is given as $\mu_{\text{boundary}} \propto T^{1/2} \exp(-\Delta E_{\text{bar}}/kT)$ [74, 75].

The mobility decreases with increasing dopant concentration as shown in Fig. 3.2.2. Thus, for bulk material high carrier density and high mobility are contrary targets. The primary reason of the decrease of mobility with increasing doping level is the increasing role of ionized impurity scattering. At

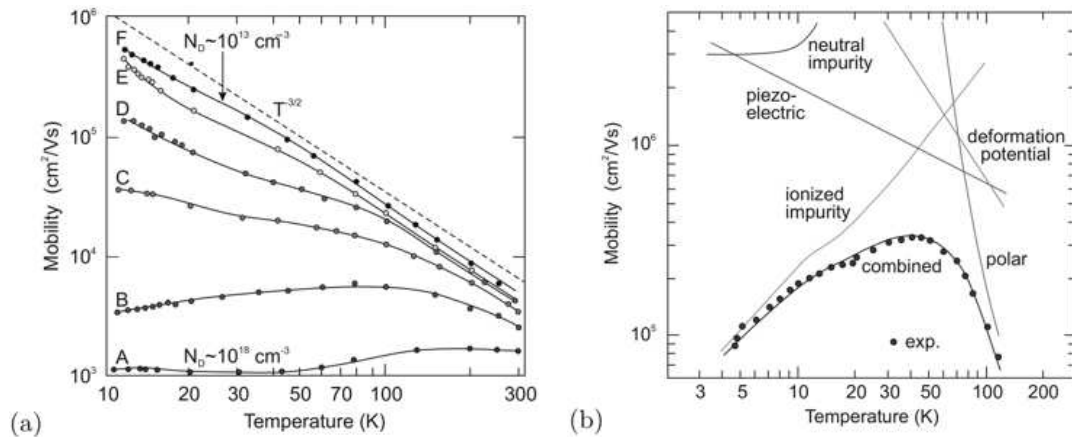


Fig. 3.2.2 a) Temperature dependence of the electron mobility for various doping levels (from $N_D \approx 10^{18}$ for sample A to 10^{13} cm^{-3} for sample F in steps of a factor of ten). Dashed line indicates $T^{-3/2}$ dependence of deformation potential scattering, solid lines are guides to the eye. b) Theoretical mobilities for various scattering mechanisms. (After [76]).

high doping level, it becomes more important at room temperature than phonon scattering [77].

3.2.3 Carrier recombination

Carrier recombination, i.e. electrons and holes, is considered a process by which both carriers annihilate each other. In this process an electron occupies – through one or more steps – the empty (electron) state associated with a so called (electron) hole. Equivalently, a carrier recombination can be considered as a transition in which an electron jumps from a high energy to a low energy state which is located in a different group of levels. Eventually, both carriers disappear in the process releasing energy equal with the energetic difference between the initial and final state. The released energy transfer to environment leads to a possible classification of the recombination mechanisms. Based on the nature of converted energy type we can distinguish them in electromagnetic and mechanical. In the first category belong all recombination mechanisms that result in energy emission in the form of a photon and they called radiative

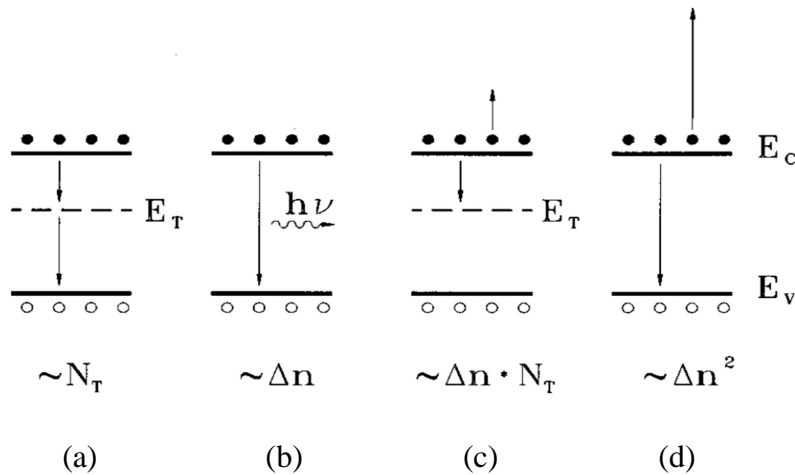


Fig. 3.2.3 Fundamental recombination mechanisms in semiconductors: a) recombination through deep traps (SRH); b) radiative recombination; c) trap-assisted Auger recombination; d) Auger recombination. E_C , E_V and E_T signify the conduction band edge, the valence band edge and a trap energy level, respectively. The respective dependencies of (the inverse of) the carrier lifetime on trap density (N_T) and excess carrier density (Δn) is shown below. (After [78])

recombinations. In the second category the released energy is converted to mechanical. This last non-radiative recombination, as it called, can be result in lattice collective oscillations or to electron kinetic energy.

The effective recombination rate can be expressed as the sum of all recombination rates that can be attributed to independent recombination mechanisms. Expressing recombination lifetime as the inverse recombination rate, the effective lifetime is written as:

$$\frac{1}{\tau_R} = \frac{1}{\tau_{SRH}} + \frac{1}{\tau_{rad}} + \frac{1}{\tau_{Auger}} \quad (3.8)$$

where each of the right hand terms, Shockley-Read-Hall (SRH) or multiphonon recombination, radiative recombination and Auger recombination represent a different recombination mechanism (Fig. 3.2.3).

SRH recombination is characterized by deep-level impurity/trap density, N_T , their energy level, E_T , and capture cross-sections, σ_n and σ_p for electrons and holes, respectively. The released energy is dissipated by lattice vibrations or phonons. The radiative recombination is an electron-hole pair direct transition that energy is released by photons. The radiative lifetime is inversely proportional to the excess carrier density because in band-to-band recombination both electrons and holes must be present simultaneously. Finally, during Auger recombination, the released energy is absorbed by a third carrier and the Auger lifetime is inversely proportional to the carrier density squared. All the above recombination lifetimes, in the general case, are given by:

$$\tau_{SRH} = \frac{\tau_p (n_0 + n_1 + \Delta n) + \tau_n (p_0 + p_1 + \Delta p)}{p_0 + n_0 + \Delta n} \quad (3.9)$$

$$\tau_{rad} = \frac{1}{B(p_0 + n_0 + \Delta n)} \quad (3.10)$$

$$\tau_{Auger} = \frac{1}{C_p (p_0^2 + 2p_0\Delta n + \Delta n^2) + C_n (n_0^2 + 2n_0\Delta n + \Delta n^2)} \quad (3.11)$$

where n_0, p_0 are the equilibrium and $\Delta n, \Delta p$ the excess carrier densities, n_1, p_1 are the thermally excited carriers from impurity/trap levels. τ_n , and τ_p are defined as the electron/hole lifetime determined by recombination centers. B and $C_{n/p}$ are the radiative and Auger for an electron/hole recombination coefficient, respectively.

At this point we have to mention another kind of recombination process: the trap-assisted Auger recombination. This is similar to the SRH process, except that the energy released when the electron (or hole) becomes trapped is transferred to a second electron (or hole) in an Auger process, rather than to a phonon. Trap-assisted Auger recombination rate has, nevertheless, a quadratic dependence on the carrier concentration as in the case of radiative recombination, but, it is proportional to the defect density N_T . Thus, one can express with a single radiative coefficient both radiative recombination and trap-assisted Auger as:

$$B = B_{rad} + C_{TAAR} N_T \quad (3.12)$$

where C_{TAAR} is a coefficient for the trap-assisted Auger recombination process.

Since the injection level is important during lifetime measurements the above expressions can be modified for low-level (ll) and for high-level (hl) injections. In our studies we have been limited to high-level injections when injected excel substantially equilibrium carriers. The equal densities of electrons and holes ($\Delta n = \Delta p$) follow a mutual annihilation during relaxation, and so, the high-level excitation recombination is called bimolecular. In this limit the above expressions are approximated by:

$$\tau_{SRH}(hl) \approx \tau_n + \tau_p \approx \tau_{SRH}^{amb} \quad (3.13)$$

$$\tau_{rad}(hl) \approx \frac{1}{B\Delta n} \quad (3.14)$$

$$\tau_{Auger}(hl) \approx \frac{1}{(C_n + C_p)\Delta n^2} \approx \frac{1}{C_{amb}\Delta n^2} \quad (3.15)$$

At high carrier densities, the lifetime is controlled by Auger recombination and at low densities by SRH recombination. The high carrier densities may be due

to high doping densities or high excess carrier densities. Whereas SRH recombination is controlled by the cleanliness of the material, Auger recombination is an intrinsic property of the semiconductor.

At this point we have to distinguish two different cases of SRH recombination according to semiconductor topology. The first one is the recombination at defect/trap centers in the interior of semiconductor far from surface or interface, and so it is called bulk SRH. The second one is not an additional recombination mechanism, but simply SRH recombination occurring at numerous surface defects like, e.g., dangling bonds. The surface SRH lifetime can be defined as:

$$\tau_s = \frac{S_n(n_s + n_{1s}) + S_p(p_s + p_{1s})}{S_n S_p (p_n n_s - n_i^2)} \quad (3.16)$$

where $S_{n/p}$ is the surface recombination velocity for electrons and holes, respectively. While in the regime of low-level injections the surface recombination velocity is approximated with minority carrier surface recombination velocity, at high-level injection is written as:

$$S(hl) = \frac{S_n S_p}{S_n + S_p} \quad (3.17)$$

Practically, in the general case, surface recombination lifetime is a function of surface/interface recombination efficiency and of carrier transport to the surface/interface from bulk. The general solution is quite complicate and is done numerically or graphically. Due to our experimentally conditions (high-level excitation regime and light penetration depth smaller than sample thickness) the surface recombination lifetime can be approximated by [79]:

$$\tau_s = \frac{d}{S} + \frac{4d^2}{\pi^2 D_{amb}} \quad (3.18)$$

Here, D_{amb} (be denoted also as D_a) is the ambipolar carrier diffusion coefficient, (it will be discussed in next subchapter). Nevertheless, in most cases the requirements for stationary conditions are not fulfilled. In a more general approximation that holds in our cases is that the second term has the dominant role and so we can say that diffusion-limited recombination take

place than the case where the first term had been dominating (surface-limited recombination).

Finally, all recombination processes can be accounted from the following form of two dimensional balance equation:

$$\begin{aligned} \frac{\partial \Delta n(x, z, t)}{\partial t} &= \nabla \left[D_a(\Delta n) \nabla \Delta n(x, z, t) \right] \\ - \frac{\Delta n(x, z, t)}{\tau_R} - B \Delta n^2(x, z, t) - C \Delta n^3(x, z, t) + G(x, z, t) & \end{aligned} \quad (3.19)$$

with the boundary conditions:

$$\left. \frac{\partial \Delta n(x, z, t)}{\partial z} \right|_{z=0} = \frac{S_1}{D_a(\Delta n)} \Delta n(x, 0, t) \quad (3.20)$$

and

$$\Delta n(x, \infty, t) = 0 \quad (3.21)$$

$$\left. \frac{\partial \Delta n(x, z, t)}{\partial z} \right|_{z=d} = \frac{S_2}{D_a(\Delta n)} \Delta n(x, d, t) \quad (3.22)$$

for a semi-infinite and layer of thickness d media, respectively. In the above equations, $G(x, z, t)$ is the carrier generation function, which in the case of spatially in-plane modulation is expressed as $G(x, t) = (\alpha I_0 / h\nu_{\text{ex}}) \exp(-\alpha x) f(t)$ with $f(t) = (1/\tau_{\text{LP}} \pi^{1/2}) \exp(-t^2/\tau_{\text{LP}}^2)$ to be the filling function of laser pulse with τ_{LP} duration. $I_0 = (1-R)$ is the total excitation fluence in the sample with α and R to be the absorption and reflection coefficients, respectively, of excitation pulse with wavelength quantum efficiency $h\nu_{\text{ex}}$ [78].

3.2.4 Carrier trapping

When we generally consider a trap-assisted recombination process we assume that equal amounts of both charged carriers ($\Delta n = \Delta p$) annihilate each other in a single trap level with similar carrier capture cross section for electron and holes ($\sigma_p \approx \sigma_n$). If, however, this condition is not satisfied, as in the cases that defect concentration N_D with different capture cross sections σ_p and σ_n is high relative to the doping or injection densities or when a high concentration N_T of shallow

defect levels is present in addition to the main recombination center, leads to unbalanced carrier densities, resulting in non-exponential carrier decays.

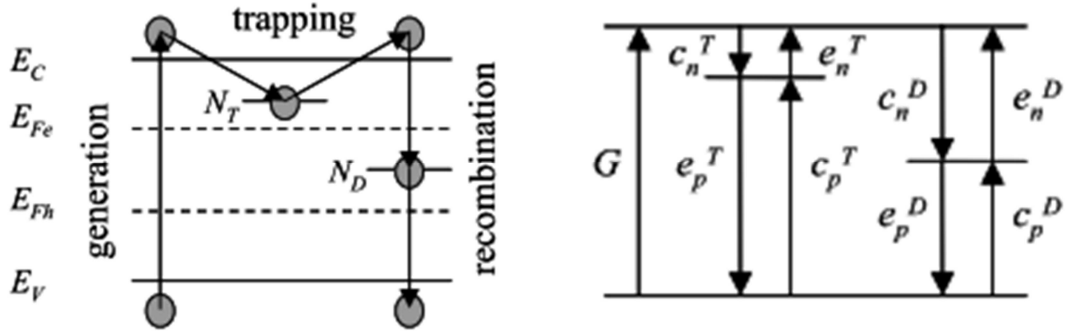


Fig. 3.2.4 Schematic representation of the trapping mechanism. (After [71])

When shallow level defects exist in high concentrations they act as carrier traps which temporarily hold before release them back to the band again. This happens because, at shallow level states, connected mainly with impurities, carrier emission to closer band is much more probable than completion of the recombination by the capture of an opposite sign carrier. The condition that has to be fulfilled is that the shallow level has to lie outside the energy region between the quasi-Fermi levels at the particular excitation intensity [80], as illustrated in Fig. 3.2.4(a), where the complete cycle between carrier generation and recombination is shown. In general, such recombination processes can be described using separate carrier emission e , capture c and generation G rates, as illustrated in Fig. 3.2.4(b) [71]. Consequently, the electron concentration in the e.g. conduction band n , in the trap n_T , and at the recombination center n_D , and the hole concentration in the valence band p obey the following rate equations:

$$\frac{dn}{dt} = -c_n^D (N_D - n_D) + e_n^D n_D - c_n^T (N_T - n_T) + e_n^T n_T + G \quad (3.23)$$

$$\frac{dn_T}{dt} = c_n^T (N_T - n_T) - e_n^T n_T + e_p^T (N_T - n_T) - c_p^T n_T \quad (3.24)$$

$$\frac{dn_D}{dt} = c_n^D (N_D - n_D) - e_n^D n_D + e_p^D (N_D - n_D) - c_p^D n_D \quad (3.25)$$

$$\frac{dp}{dt} = e_p^D (N_D - n_D) - c_p^D n_D + e_p^T (N_T - n_T) - c_p^T n_T - G \quad (3.26)$$

where c and e are the capture and emission rates for carriers, respectively. These quantities differ between the deep recombination center and the shallow trap only in the capture cross-section and the position of the relevant energy level in the band-gap. Theoretical fits these equations on experimental carrier dynamics at different temperatures and at different excitation conditions can provide values for the capture cross-section, the energy position and concentration of traps [81].

3.2.5 Compensation in semiconductors

Limiting ourselves to low temperatures or to wide band gap semiconductors, like SiC, where the intrinsic carrier density can be neglected, and having donors and acceptors simultaneous present, we can consider that some of the impurities will compensate each other. Electrons from donors will recombine with holes on the acceptors. Depending on the quantitative situation the semiconductor can be n- or p-type.

Moreover, with increasing concentration, the distance between impurities decreases and their wavefunctions can overlap, and hence, an impurity band is developed. Since the impurity atoms are not arranged periodically in host semiconductor lattice but they are randomly distributed, the band edges exhibit tails. At high doping concentration, the impurity band overlaps with the conduction band. If compensation is taking place simultaneously, the impurity band is not completely filled anymore and contains opposite type of carriers. In this case, conduction can take place within the impurity band even at low temperature, making the semiconductor a metal. This metal–insulator transition has been discussed by Mott. The critical density for this transition, N_C , can be estimated from the Mott criterion when the distance of the impurities becomes comparable to their Bohr radius, a_D [76]:

$$a_D = \frac{m_0}{m_e^*} \epsilon_r a_B \quad (3.27)$$

where $\alpha_B = 0.053$ nm denotes the hydrogen Bohr radius, m^* the isotropic effective mass, and ϵ_r the dielectric constant. The formation of the impurity band leads to a reduction of the impurity ionization energy. At the critical doping concentration of N_c the activation energy for the carrier concentration disappears. The ionization energy of donor or acceptor decreases with its ionized dopants concentration N_i as [82, 83]:

$$E = E_0 - \alpha N_i^{1/3} = E_0 \left[1 - \left(\frac{N_i}{N_c} \right)^{1/3} \right] \quad (3.28)$$

The constant α is related to impurities compensation degree, K , as [84]:

$$a = f(K) \frac{e^2}{4\pi\epsilon_r\epsilon_0} \quad (3.29)$$

where $f(K)$ is a (dimensionless) function, the exact form of which depends on the details of the concrete mechanism leading to the reduction of the thermal ionization energy. Among several different theoretical models that have been proposed the most successful is based on the concept of electrostatic interaction between the free carriers and the oppositely charged impurity centers originally proposed by Pearson and Bardeen [83] and modified by Debye and Conwell [82]. A similar model proposed by Monecke et al. [85] incorporates also the effects of the relaxation of the distribution of carriers on the impurity centers. A relative approach of different theoretical functions on experimental results is presented in Fig. 3.2.5.

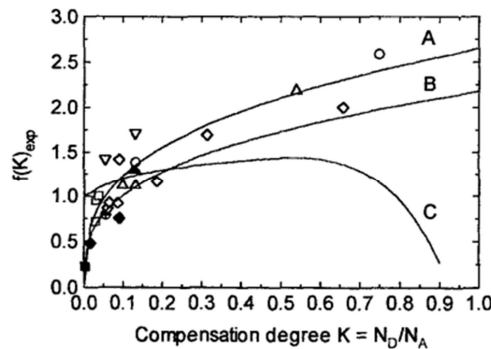


Fig. 3.2.5 Theoretical and "experimental" curves of the function $f(K)$ versus K . Data collected and reanalyzed from the literature. Theoretical curves: A - according to Debye and Conwell, B - according to Monecke. (After [84])

3.2.6 Thermal activation energy of impurities

Thermal activation energy is an empirical parameter characterizing the exponential temperature dependence of a specific experimentally determined quantity. This quantity, which in our case is the charged carrier lifetime, obeys to a simple, but remarkably accurate, formula: the Arrhenius equation. According to this equation we can express the charged carrier recombination rate, which is proportional to inverse charged carrier lifetime, as:

$$R = R_{th} + R_0 e^{\left(\frac{E_a}{kT}\right)} \quad (3.30)$$

where R_{th} is the recombination rate of donor-acceptor pairs and carriers-impurities, and R_0 a pre-exponential factor. Plotting the experimentally determined recombination rate with the inverse absolute temperature in a semi-logarithmic diagram, usually referred as Arrhenius Plot, one is able to obtain by linear fitting the activation energy of the mechanism that causes lifetime changes as temperature increases. Nevertheless, in a real material, more than one, independent processes corresponding to different energetic levels that different impurities have into energy band gap. In this case the resulted exponential decay can be expressed by multi-term decay function in which each term represents a single-exponential decay mechanism associated with a specific energy state:

$$R = R_{th} + R_0 \left(w_1 \exp\left(-\frac{E_a^1}{kT}\right) + w_2 \exp\left(-\frac{E_a^2}{kT}\right) + \dots \right) \quad (3.31)$$

where w_1, w_2, \dots are the weighting parameters and E_{a1}, E_{a2}, \dots are the activation energies for each independent energy level, respectively. As a matter of fact, during evaluation process, the number of parameters is increasing so much that the total uncertainty makes the reliable determination practically impossible or at least questionable. The cases that are able to provide a reliable result are these that one energy state is dominating, i.e. when the level population exceeds substantially from others, or, all the other activation processes are practically over. In the first case the long decay tail, after the R_{th} subtraction, shows single-exponential decay behavior. In the second case, avoiding the

initial part of mixed long slow decay tail, we can consider the single-exponential decay kinetics ascribed to an only energy state.

3.3 Optical time-resolved techniques

The optical time-resolved techniques are based on the changes of dielectric function of the semiconducting materials, or else, on the spatial-temporal modulation of their refractive index and absorption coefficient. As the knowledge of carrier dynamics is the key issue in most technologically materials, nonlinear optical techniques of active spectroscopy, based on strong correlation between the electrical and optical phenomena, provides a possibility for nondestructive, contactless study with high spatial and temporal resolution in a wide spectral and temperature tunable range [86].

3.3.1 Light-induced transient grating (LITG) technique

In LITG technique the matter (e.g. semiconductor) is exposed to a strong interference pattern of light creating in material a light induced grating. The appropriate light source for that has to meet the conditions for a light interference pattern. Laser pulses are perfectly suited and commonly used for a grating recording because of their short duration capability, coherence, high intensity, good beam collimation and wavelength tunability that allows the selective material excitation. For the grating recording two TEM₀₀ beams, which approximate the ideal plane waves, are used. The interference pattern, (as in Fig. 3.3.1), of two plane waves produces spatially periodic light intensity profile:

$$I(x) = I_0 (1 + m \cos(Kx)) \quad (3.32)$$

where I_0 is the sum intensity of pump beams (I_1+I_2), m is modulation depth ($2(I_1+I_2)^{1/2}/(I_1+I_2)$) and $K=2\pi/\Lambda$ is a grating vector. Λ is a grating period which can be varied by changing incident angle of pump beams as $\Lambda=\lambda/(2\sin(\theta/2))$.

The nonlinear absorption and refraction in materials can be considered as the interaction of two light beams having in general consideration distinct

frequencies (ω_a and ω_b) in a nonlinear medium. In such an interaction, two beams can alter each other phase or amplitude, the latter process requiring certain energy resonances. The preceding condition, known as the non-degenerate interaction, is the general case of a simpler degenerate situation, where the beams have the same frequency ($\omega_a = \omega_b$) [70].

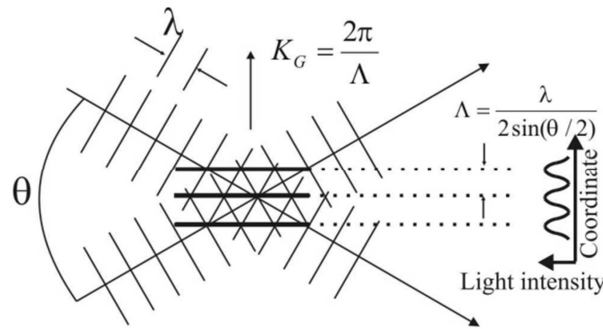


Fig. 3.3.1 Schematic representation of transient grating formation by interference of two coherent laser beams. (After [70]).

There are three main mechanisms of the grating formation: free-carrier (FC) grating, photorefractive (PR) grating and free-carrier absorption (FCA) grating. Since in our experiments the dominant mechanism for the diffraction grating was the free-carrier mechanism, we concentrate exclusively on this one.

As in §3.1 is set out, the induced free carrier distribution result in modulation of complex refractive index (or complex dielectric function). The created spatial modulation of complex refractive index can be measured from the diffraction of probe beam. The diffraction is strongly dependent on the grating thickness d . A rough estimation of grating thickness is made from comparison with grating period: if d is of the order of Λ or smaller, the grating is called thin, otherwise it is called thick. The more precise condition for a grating with arbitrary thickness d can be obtained by dividing the whole grating to smaller thin grating elements. Assuming that the diffraction angle on an elementary grating is small, the phase difference Q between beams diffracted at two neighboring elements is equal to [70]:

$$Q = \frac{2\pi d \lambda}{\Lambda^2 n} \quad (3.33)$$

where λ is the light wavelength in vacuum. If the phase difference is sufficiently small ($Q \ll 1$) the beams from all grating elements interfere constructively. If the phase difference is large ($Q \gg 1$), destructive interference occurs and the total diffracted intensity becomes small. Only in the case of oblique incidence at an angle α and a diffraction angle $\phi = 2\alpha$, which can be considered as reflection of the incident beams at the grating plane, there is no phase difference between all the beams diffracted at the grating planes (Fig. 3.3.2(b)). In such a case strong diffraction can be observed in a thick grating, too.

During LITG experiment the most important experimental quantity which is measured is the diffraction efficiency η of the induced dynamic transient grating, i.e. the ratio between transmitted and diffracted beams $\eta = I_D/I_T$. For thin absorption and refractive index grating the diffraction efficiency of the first diffraction order is given by [70]:

$$\eta = |J_1(\phi)|^2 \quad (3.34)$$

where J_1 is the first order Bessel function with argument $\phi = 2\pi\Delta\tilde{n}d/\lambda$ where \tilde{n} is the complex refractive index and d the grating width. For $\phi \ll 1$ the diffraction efficiency can be approximated as:

$$\eta = |J_1(\phi)|^2 \approx \frac{\phi}{2} = \left| \frac{\pi\Delta\tilde{n}d}{\lambda} \right|^2 = \left(\frac{\pi\Delta n d}{\lambda} \right)^2 + \left(\frac{\Delta\alpha d}{4} \right)^2 \quad (3.35)$$

Since in the spectral region below bandgap the absorption is weak we can omit the free-carrier absorption term, so that:

$$\eta \approx \left(\frac{\pi\Delta n d}{\lambda} \right)^2 = \left(\frac{\pi n_{eh} \Delta N d}{\lambda} \right)^2 \quad (3.36)$$

In the last part, the diffraction efficiency is expressed in terms of induced excess carrier concentration. According this it is clear that the diffraction efficiency is proportional to the square of induced excess carrier concentration. In this way, the probe beam diffraction sensitivity reflects the instantaneous

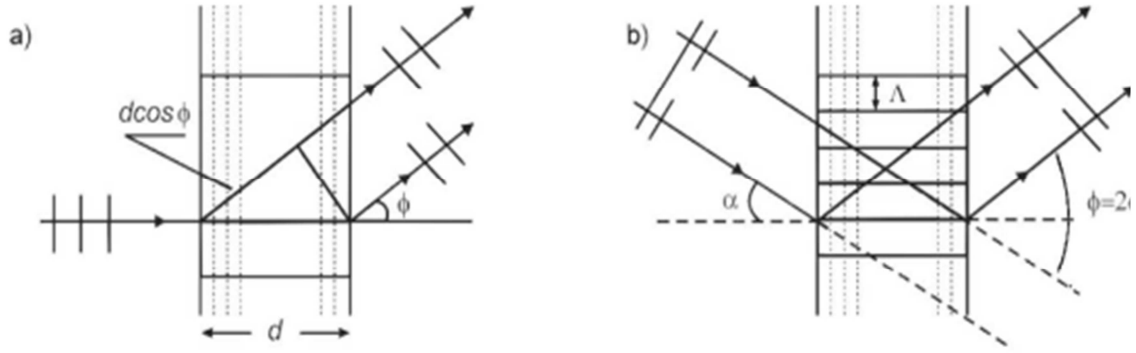


Fig. 3.3.2 Diffraction at a thick grating treated by successive diffraction of the incident beam at thin grating elements: a) normal incidence, b) Bragg diffraction. (After [70])

value of grating modulation, i.e. the difference of carrier density in the grating peaks and valleys. The carrier modulation decays by simultaneous diffusion and recombination with dependence of grating period τ_G as $\eta(t) \sim \exp(-2t/\tau_G)$. The plot of the inverse grating decay $1/\tau_G$ vs. $(2\pi/\Lambda)^2$ allows the determination by linear fit of diffusion coefficient D_a as well as the carrier recombination time, since:

$$\frac{1}{\tau_G} = \frac{1}{\tau_R} + \frac{1}{\tau_D} \quad (3.37)$$

where τ_R is the recombination time and $\tau_D = \Lambda^2/(4\pi^2 D)$ is the erasure time of carrier grating with period Λ by diffusion.

Among the advantages of LITG technique the most important is the sensitivity because of the high signal to noise ratio since the signal is measured in dark field.

3.3.2 Differential transmittance (DT) technique

DT technique is based on absorption change either by free or trapped carriers, or by band gap renormalization effects. It is of widespread use and it is a very general tool applicable to most semiconductor materials and also to devices. It provides an exceptional advantage, as different geometries and very different injection regimes can be realized, and therefore many different materials and recombination mechanisms may be characterized [87]. Concerning DT

technique, the change at imaginary part $\Delta\alpha$ of complex refractive index due to light induced free carrier concentration ΔN as a function of time is written as $\Delta\alpha(t)=\sigma_{eh}\Delta N(t)$, where σ_{eh} is the electron-hole capture cross section of probe beam photons. The free carrier density is decreasing with time only through recombination. Here, carrier in depth diffusivity has no effect on absorption coefficient modulation, and hence, the differential transmittivity is direct proportional to ΔN . The transient transmittivity is $T(t)=T_0\cdot\exp(-\Delta\alpha(t)\cdot d)$, where $\alpha(t)=\alpha_0+\Delta\alpha(t)$ is the excess carrier density modulated absorption coefficient and d is the excited thickness. Generally, the lifetime may be defined using a general recombination rate of excess electron-hole pairs R according to:

$$\tau = \frac{\Delta N}{\Delta R} = -\frac{\Delta N}{(d\Delta N/dt)} \quad (3.38)$$

The lifetime may not be a constant but may be a complicated function of injected carrier density and other parameters. The decay shape could be divided in the non-exponential recombination due to high carrier concentration, while, at slightly lower injections, but still above the doping density, a linear region is observed where a high-injection lifetime may be extracted. Finally, at low injections, the minority carrier lifetime may be derived. In our studies, excitations at high-injection level took place avoiding reach the intense Auger recombination regime.

Chapter 4 Experimental setup

In this chapter it is presented the experimental setups that was required in order to perform optical time-resolved measurements in differently grown 3C-SiC wide-bandgap semiconductor materials. All of them belong to the time-resolved pump-probe methodology. Their principle is based on the time-space evolution of a carrier distribution. One of them can modulate its sensitivity to carrier mobility or recombination while the other one is dedicated to carrier recombination mechanisms.

The core of all setups are mode-locked pulsed lasers, either a Nd⁺³:YLF (mod. PL-2243), or a Nd⁺³:YAG (mod. PL-2143), both been manufactured by “Ekspla” company. They generate a ~7 and ~25 ps duration pulses at the fundamental harmonic of 1053 and 1064 nm, respectively, at fixed 10 Hz repetition rate. The pulses feature good energy stability (<1.5% sd in the fundamental harmonics for both lasers) and high polarization degree. The maximum output pulse energy is ~10 and ~30 mJ in fundamental harmonic, and two or three times lower for second (527/532 nm) and third (351/355 nm) harmonic, respectively. A third Nd⁺³:YAG nanosecond laser (model NL202, Ekspla) is used as probe beam generator for long delay times due its triggering by a picosecond laser.

4.1 Light Induced Transient Grating (LITG)

In Fig. 4.1.1 is depicted the modified LITG setup. This is an evolution of the standard LITG setup. The grating-recording beam of required wavelength is collimated using a telescope, which also decreases the beam diameter from ~6 mm at laser exit down to ~2 mm. The energy of recording beams is attenuated either by polarization rotator ($\lambda/2$ plate) and polarizer (Glan prism) or by varying electronically the triggering time of amplifier flash lamp, what also results in altered output energy of the laser. In a standard LITG configuration a dielectric beam splitter divides pump beam to two parts of approximately

equal energies. These two recording beams are arranged to cross at sample position at an angle θ . The difference in travel paths of the beams is compensated using a pump delay line in one arm of recording beams. The shutter is used to close recording beams periodically, what allows an estimation intensity of scattered light, i.e background. Despite the success of standard configuration, there were always experimental difficulties at temporal and spatial overlap of the two pump and the probe beams since a ~ 10 ps light pulse duration corresponds only in 3 mm in space and their coincidence was difficult to be achieved at a reasonable time. Moreover, the background light originated from scattered light from sample and optics superimposed with background-free diffraction beam leading to spatial interference on detector, or as it is known to heterodyne amplification. Both problems can be solved by the use of a heterodyne detection setup with holographic beam splitter (HBS) which allows a simple deconvolution of diffracted signal and interference term with a background and it simplifies the change of transient grating period Λ . The key element of the setup is a holographic beam splitter (HBS), which can be moved along its grating vector (see Fig. 4.1.1). The deconvolution is achieved by subtracting two decay kinetics, recorded at different HBS positions, which correspond to the opposite phases of interference term. Moreover, the use of HBS simultaneously with collinear propagation of pump and probe beam meets the requirements for reflection Bragg grating (not

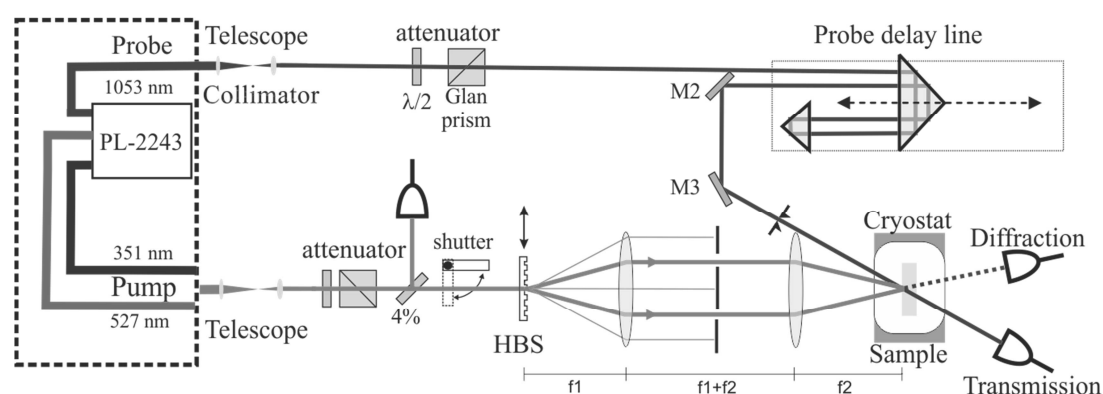


Fig. 4.1.1 Experimental scheme of LITG experiment using holographic beam splitter.

shown in Fig. 4.1.1). The telescope between HBS and sample has, among other, the role of beam diameter modulator and hence the energy flux on sample.

4.2 Differential Transmission (DT)

The DT method is basically a more primitive method and this has a consequence to setup design. It is needed only one pump beam for the carrier injection and a probe beam for carrier monitoring in time. DT technique can be applied in two differed configurations concerning the relative geometry of pump and probe beams.

4.2.1 Collinear configuration

When pump and probe beam incident at the same spot on sample's surface at a small mutual angle we consider it as collinear configuration of DT. Operation of different beam delay equipment allows the monitoring of free carrier time evolution in initial short or long delayed times (Fig. 4.2.1). The optically delayed picosecond probe pulse at 1053/1064 nm was used to monitor the initial fast decay transients of induced free carrier absorption (FCA), while an electronically delayed a 6-8 ns duration pulse at 1064 nm was used for monitoring of the long relaxation tails up to several tenths of microseconds.

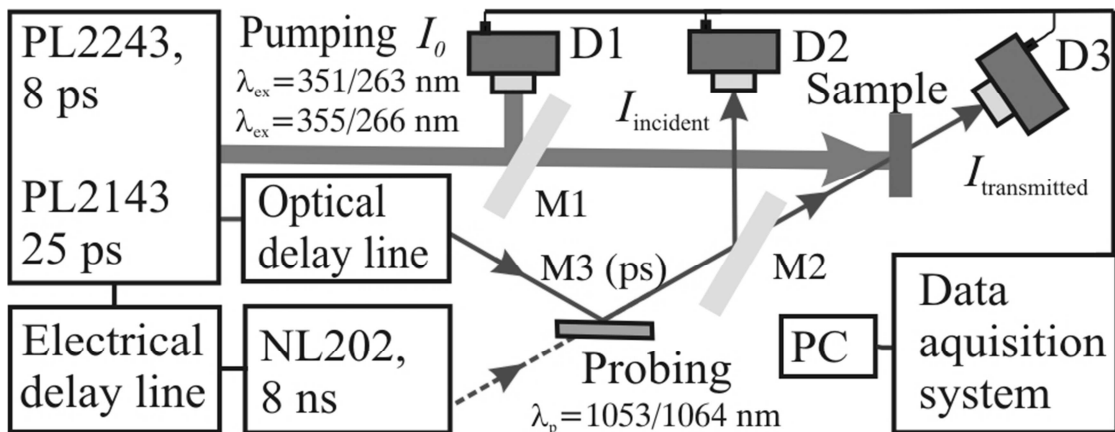


Fig. 4.2.1 DT configuration diagram with optical and electrical delay for the probe beam. (From [88])

The time resolution is related to probe pulse duration in both delay configurations and is approximately 10 ps and 10 ns, respectively.

The following Fig. 4.2.2 shows schematic of the collinear geometry where both excitation and probe beams enter the sample from the same side. The transmitted probe beam is collected by a lens and focused onto a photodetector. The excited area is large compared to typical diffusion lengths in the sample, therefore, the probed sample area is smaller than the excitation area, and may be regarded as laterally homogeneous.

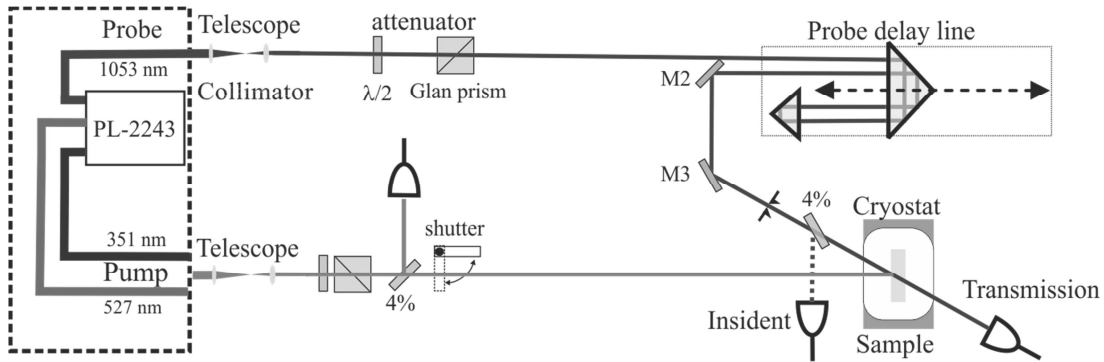


Fig. 4.2.2 Schematic representation of the collinear geometry. (After [89])

4.2.2 Orthogonal configuration

The experimental pump-probe DT setup in orthogonal configuration is shown in Fig. 4.2.3. The probe beam on the left hand side is generated by a 5mW continuous wave (cw) semiconductor laser at 1.54 μm wavelength and is appropriately calibrated using an established calibration procedure [90]. The probe beam is focused on the sample which can be mounted in an open cycle helium cryostat which operates over a 4-500 K temperature range and perform three dimensional motorized translations with μm precision. The transmitted probe beam is collected by a system of optical lenses and detected by a 0.5 ns rise-time photo-receiver, which is subsequently connected to a digital 1 GHz bandwidth oscilloscope and a PC. The spatial resolution of the probe within a sample depends on the probe wavelength, the focal length of the focusing lens and the sample thickness along the probed path. In general, better resolution

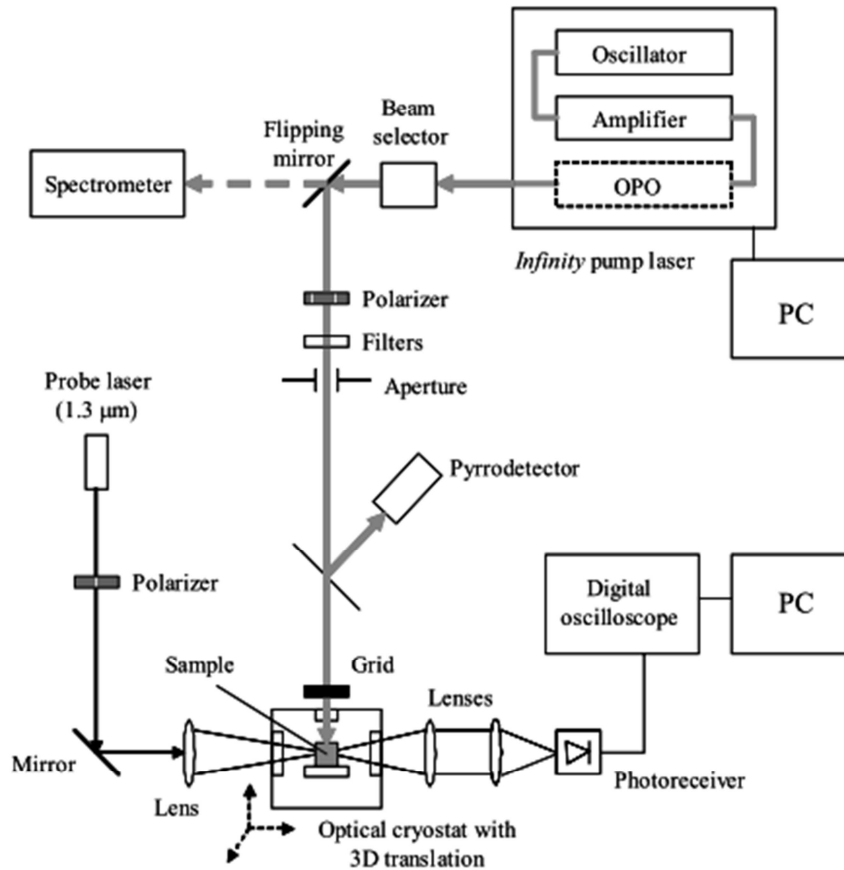


Fig. 4.2.3 Schematic illustration of the experimental pump-probe setup utilizing FCA probing. (After [71]).

could be obtained with shorter probe wavelengths and lenses with short focal length. However, as indicated by the classical Drude model, the magnitude of α_{FCA} scales as λ^2 leading to a lower signal to noise ratio for shorter wavelengths. In the case of low FCA absorption within the sample one also has to avoid multiple reflections and interference effects of the probe. The latter imperfections, however, are highly suppressed if the polarized probe beam meets the surface at the Brewster angle with respect to the surface normal. The pump beam (as Fig. 4.2.3 illustrates) is generated by a pulsed laser (*Infinity*), which is comprised of a specially amplified Nd^{+3} :YAG modulus. The laser pulse is approximately 2 ns duration, while its typical energy is 1-10 mJ and its operation frequency is 10-100 Hz. A special feature of the *Infinity* laser beam is its uniform and wide (~5 mm) intensity profile in all operation harmonics (modes): 1.064, 0.533, and 0.355 μm . Moreover, the *Infinity* laser is extended

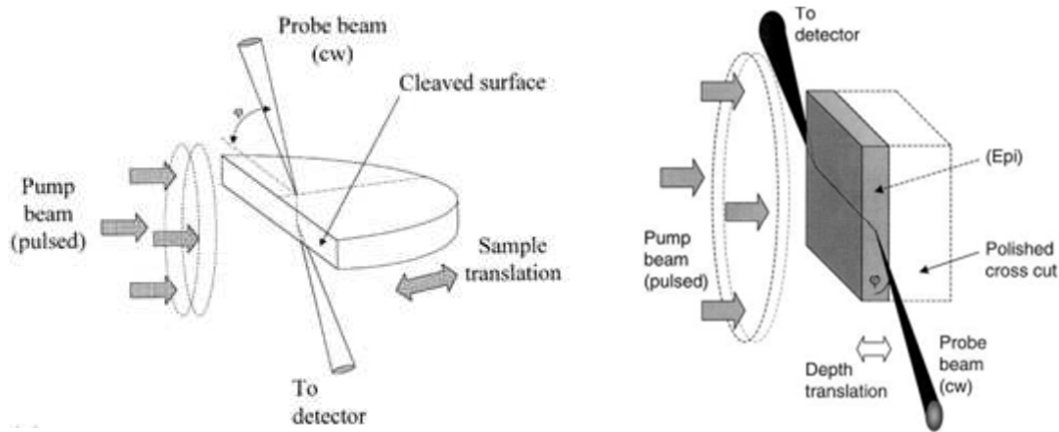


Fig. 4.2.4 Two different scanning arrangements of orthogonal DT configuration. (After [89])

with an optical parametric oscillator (OPO) pumped by one of the modes. With the use of third harmonic of $0.355 \mu\text{m}$ and OPO we obtain by tuning of excitation wavelength close to the band gap of 3C-SiC a $520 \mu\text{m}$ probe beam with a nearly constant distribution of excited carriers along the z-direction of the wafer [91]. The intensity of the beam varies over the spectral ranges employed and is therefore calibrated with a pyroelectric detector. Finally, the polarization of both probe and pump beams can, if needed, be rotated using a Berek polarizer, which is capable of keeping the polarization ratio greater than 1:100.

The main advantage of the orthogonal geometry is the ability to perform depth-resolved measurements. In such a geometry, where the probe beam is scanned across the side surface by moving the sample, it is possible to characterize the effective surface of a sample with the appropriate of probe's beam diameter. For this geometry the samples can also be cut in such a way that the probe beam path is rather extended. This yields a high sensitivity in terms of the concentration detected. Moreover, in this type of orientation a uniform excitation is ensured along the probe beam path.

Chapter 5 Excess carriers decay in 3C-SiC

This chapter consists from two subchapters. The first one is dealing with the carrier lifetime concept in bulk 3C-SiC samples. The second one is dealing with general aspects that relate structural and electrical characteristics of 3C-SiC thin layers. The concept of trapped carriers and, the determination of their impurities concentration and nature are analyzed.

5.1 Excess carrier recombination lifetime of bulk n-type 3C-SiC

5.1.1 Introduction

Excess carrier lifetime is a sensitive indicator of a single crystal quality and cleanliness, while it can determine the performance of devices [92]. Carrier lifetime may impact device operation directly, such as by affecting the turn-off speed of a diode or a thyristor operating at high injections or the leakage current of a pn-junction, or indirectly, such as by affecting the current gain of a bipolar transistor. Thus, a high carrier lifetime is desirable in many cases, whereas a low lifetime favors specific applications. Furthermore, for optically active devices, one is interested in radiative recombination, and other recombination mechanisms must be suppressed to enhance quantum efficiency. In contrast to other polytypes [93, 94, 95, 96, 97, 98], dominant recombination mechanisms in 3C-SiC are poorly understood. Under low-level (LL) excitation ($\Delta n \ll n_0$, where Δn and n_0 are the excess and the equilibrium electron concentrations, respectively), carrier decays in 3C-SiC were obtained by microwave [99] and photoconductivity [100] techniques. Both techniques showed that carrier decay is consisting of the initial fast $\tau_R \approx 1-15 \mu\text{s}$) part and the subsequent slow $\tau_S > 1 \text{ ms}$) tail. The initial part was assigned to the recombination through active recombination levels while the appearance of the tail was attributed to the (minority) carrier trapping by the deep band gap centers. The effect of a high build-in strain [101] between the thin 3C-SiC

epitaxial layers and the Si substrates was not considered in these studies. Under high-level (HL) excitation ($\Delta n \gg n_0$), excess carrier decays were studied using the LITG technique [102, 103]. The high temporal resolution of these experiments has shown fast decays within 1–4 ns. At these high carrier concentrations, an increase of lifetime was registered, something that opposed to the conventional lifetime decrease due to Auger recombination mechanism. In the following, it is presented an investigation of carrier recombination processes in thick, freestanding 3C-SiC samples using the time- and spatially-resolved DT techniques based on free carrier absorption effect. A wide injection range, covering transitioning from LL to HL excitation regimes, was achieved in our experiments and thus allowed to get insight into recombination mechanisms controlling the bulk lifetime of 3C-SiC.

5.1.2 Samples and techniques

Three different 3C-SiC samples, two grown on the Si substrates (samples H1 and H2) and one grown on the 6H-SiC substrate (sample B4), were investigated in this work. Free standing wafers were obtained by removing the substrates with chemical etching and/or mechanical polishing. The growth of bulk sample is described in Ref. [103]. Sample labeling, wafer thicknesses d , and concentrations n_0 at room temperature are provided in Table 5.1.1. In pump-probe experiments were used two different measurement geometries: an orthogonal and a collinear. In the orthogonal geometry, used for excitations up to $2 \times 10^{18} \text{ cm}^{-3}$, the cross-cut side of 3C-SiC wafer was homogeneously excited with a 2 ns duration laser pulse. Nearly constant distribution of excited carriers was achieved along the in-depth z -direction of the wafer by tuning the excitation wavelength close to the band gap of 3C-SiC. The induced excess carrier dynamics was detected by the DT (or FCA) decay, $\Delta\alpha(t,z)$, of the continuous probe beam propagating perpendicularly to the excited lateral surface. Concentration of the excess electron and hole (e-h) pairs was directly proportional to the induced absorption changes: $\Delta n(t,z) = \Delta\alpha(t,z) / \sigma_{\text{eh}}$, where the FCA cross-section $\sigma_{\text{eh}} = 1.4 \times 10^{-17} \text{ cm}^2$ was obtained for the $1.54 \mu\text{m}$ wavelength

probe beam using the established calibration procedure [90]. Scans along the z-direction were obtained while the resolution of the probe beam within the sample was $8 \mu\text{m}$. In the collinear geometry, used for excitations above $2 \times 10^{18} \text{ cm}^{-3}$, both pump and probe beams were directed to the same point on the wafer surface. Excitation was done with a different laser generating 25 ps duration pulses at 351 nm wavelength and probing was done with an optically delayed probe beam at 1.05 μm wavelength. The induced absorption changes, $\Delta\alpha(t)$, were detected by delaying the probe pulses with respect to the excitation pulses where $\sigma_{\text{eh}} = 1 \times 10^{-17} \text{ cm}^2$ was set for the 1.05 μm wavelength. An integrated injected carrier concentration Δn_{IN} values of e-h pairs was calculated using the known photon flux at the sample surface and the known absorption coefficient α of the excitation wavelength. For 351 nm wavelength the absorption depth α^{-1} is about equal to about 5 μm [102, 103].

5.1.3 Results and discussion

Fig. 5.1.1(a) shows carrier decays detected in all three samples at the photo-induced carrier concentration of $\Delta n_{\text{IN}} \approx 10^{18} \text{ cm}^{-3}$. In the H1 and H2 samples the initial part of the decays was almost a single exponent with the excess carrier recombination lifetimes τ_{R} in the order of 100 ns. At longer times, decays diverged into slow milliseconds components, as it is represented in inset of Fig. 5.1.1(a). The initiation of these slow components coincides with the achievement of the saturated concentrations Δn_{S} which is depicted in Fig. 5.1.1(b) with open symbols. In the B4 sample, grown on the 6H-SiC substrate, the peak measured concentration, Δn_{PK} , was much smaller than Δn_{IN} indicating that τ_{R} is lower than the ~ 2 ns duration of the excitation laser pulse. The initial fast decay was again followed by the slow milliseconds component with the Δn_{S} magnitude values substantially higher than in the H1 and H2 samples as in Fig. 5.1.1(b) is denoted with open symbols-dashed lines. Fig. 5.1.1(b) shows Δn_{PK} (solid symbols) and Δn_{S} (open symbols) in the H2 and B4 samples plotted versus Δn_{IN} . In both samples Δn_{PK} was linearly dependent on Δn_{IN} , while Δn_{S} was saturating at higher Δn_{IN} . Gradual saturation behavior is typical

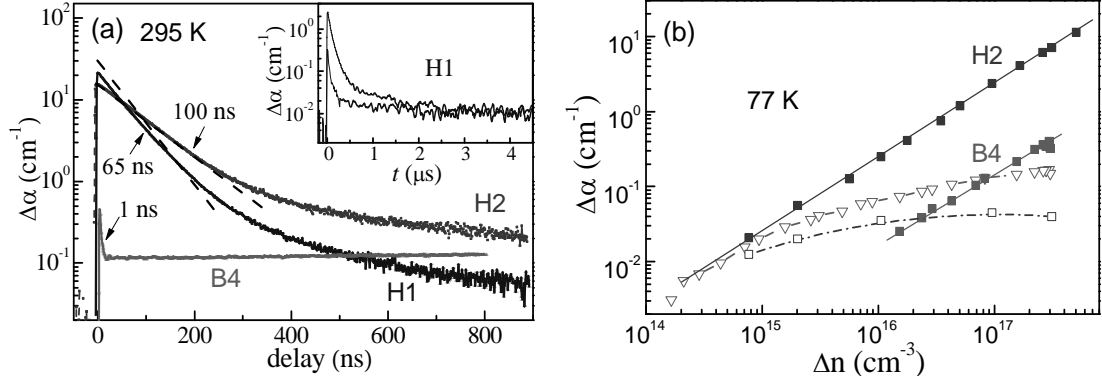


Fig. 5.1.1 a) Transient concentration $\Delta n(t)$ in 3C-SiC samples at injection density of 10^{18} cm^{-3} , when excited by 2.384 eV energy photon pulses at 295 K. Exponential fit is applied to the initial decay. In the inset, two transients on H1 sample are shown for lower injections over a longer time scale. b) Injection dependences of transient concentration magnitude at 77 K excited by 2.53 eV. Peak concentration Δn_{PK} (squares) and saturated concentration Δn_S (triangles) is shown for H2 and B4 samples. Inset shows experimental configuration for measurement under orthogonal and collinear geometries.

for minority carrier trapping by deep band gap centers [96, 99, 100]. The Δn_S tends to reach an upper limit as excitation increases and to be equated to the total density of filled traps, N_T , assuming that the electron is dominating the FCA cross-section, i.e. $\sigma_e \approx \sigma_{eh} = (4.4 \pm 0.5) \times 10^{-18} \text{ cm}^2$ [104]. The N_T values, determined by the change to the absorption coefficient that induces the amount of trapped carriers, $\Delta \alpha = \sigma_{eh} \Delta N_T$, are presented in Table 5.1.1. Since we know from samples providers that all samples under investigation are unintentionally doped by nitrogen impurities at the approximately the same concentration as N_T we can ascribe to dominant carrier traps the nitrogen impurities.

The effect of surface recombination to the measured τ_R values was evaluated using in-depth scans of carrier decays [96, 97]. Fig. 5.1.2(a) shows $\Delta n(t, z)$ profiles detected along the z -direction of the H1 sample at different moments after the excitation pulse $\Delta n_{IN} \approx 3 \times 10^{17} \text{ cm}^{-3}$. No tangible reduction of Δn at 10 μm distance from the surface was observed during the decay times equating several τ_R . The carrier decay diffusion profile evolution was simulated

Table 5.1.1 Sample labeling and basic parameters at room temperature.

Sample	Thickness d (μm)	Equilibrium density n_0 (cm^{-3})	τ_R (ns) ($\Delta n=2\times 10^{17}$ cm^{-3})	Trap density N_T (cm^{-3})
H1 (Si)	255	$(3-5)\times 10^{15}$	55 (spread ± 17)	$(7-10)\times 10^{14}$
H2 (Si)	160	$(1-3.5)\times 10^{17}$	88 (spread ± 42)	5×10^{16}
B4 (6H-SiC)	800	$(1-5)\times 10^{16}$	0.8	1.45×10^{16}

through the one-dimensional model [105] using the measured ambipolar carrier diffusion coefficient value $D_a \approx 3.3$ cm^2/s [103]. The calculations showed that the upper limit of surface recombination rate S is 10^3 cm/s . This value is smaller than the 10^3 – 10^5 cm/s range of rates determined for the mechanically polished surfaces of 4H- and 6H-SiC polytypes [97] and does not significantly affect the measured τ_R values in 3C-SiC at these delay times since only the initial fast decay is governed by surface recombination [106]. Statistical distribution of lifetimes at different sample places was also evaluated using in-depth scans. The vertical bars in Fig. 5.1.2(b) show τ_R distribution in the H1 sample obtained during the 20 μm step along the in-depth direction. The detected distribution was well fitted using the Gaussian function as shown by the solid line. The same Gaussian distribution was characteristic for higher Δn_{IN} as illustrated by the dashed line, something that is attributed to the saturation of carrier trap centers. Statistical lifetime averages and their spreads at the FWHM are provided in Table 5.1.1 for all samples at $\Delta n_{\text{IN}}=2\times 10^{17}$ cm^{-3} . The detected ratio between the average values and their spreads compares to obtained results for other polytypes of SiC [97].

Dominant recombination mechanisms in 3C-SiC were determined from the τ_R measurements at different Δn_{IN} . In order to separate these changes from the statistical τ_R variations within the sample, special care was taken probing samples at the same position. Fig. 5.1.3 shows τ_R (Δn_{IN}) dependence measured in H1 (triangles) and H2 (squares) samples at 295 K (open symbols) and 77 K (solid symbols). The circled symbols in the figure show the precise τ_R value of the initial fast decay of the B4 sample at room temperature, which were

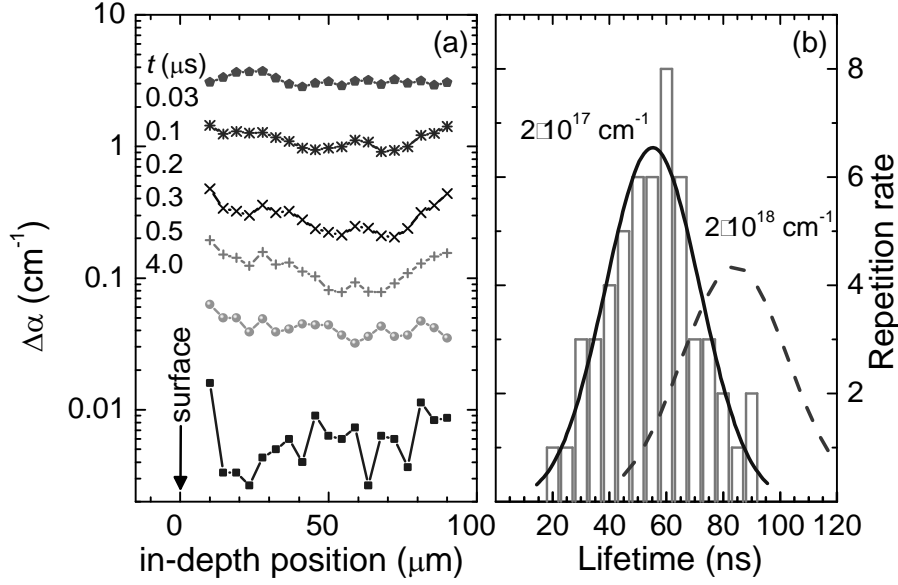


Fig. 5.1.2 a) Z-distributions of $\Delta n(t,z)$ at different times after 2.48 eV photon pulse excitation in H1 sample at 295 K. $Z(0)$ position matches to the excited surface. b) Histogram of τ_R values from different locations and the corresponding Gaussian fit for two indicated injection concentrations Δn_{IN} .

determined by the LITG (or FWM) technique [103]. The steep decrease of lifetime observed in the H2 sample at 295 K above 10^{19} cm⁻³ appeared due to Auger recombination. The $C=2.5 \times 10^{-32}$ cm⁶/s Auger coefficient was extracted from the $C=(\tau_R \times \Delta n^2)^{-1}$ data fits [107]. This value was found thirty times smaller than the one obtained in the 4H-SiC polytype [97]. The result can be explained by the difference in the band structures of the two polytypes. In the direct e-e-h Auger process, the $2E_g(X_{1C}-\Gamma_{15V}) \geq E_g(\Gamma_{1C}-\Gamma_{15V})$ requirement k-vector conservation within the Brillouine zone has to be satisfied [108, 109], where $E_g(X_{1C}-\Gamma_{15V})$ is the indirect band gap and $E_g(\Gamma_{1C}-\Gamma_{15V})$ is the direct gap at the Γ -symmetry point. While this requirement is almost fulfilled in 4H-SiC polytype, there is ~ 1.3 eV deficit in the band structure of the 3C-SiC polytype. Therefore, the weak phonon- and trap-assisted Auger process is the most likely recombination mechanism in 3C-SiC at high injections [110].

In the Δn_{IN} range $5 \times 10^{15} \div 5 \times 10^{18}$ cm⁻³, the τ_R dependency in all samples at room temperature had a V-shape. This dependency became even more pronounced in H1 and H2 samples at 77 K. The standard Shockley–Read–Hall

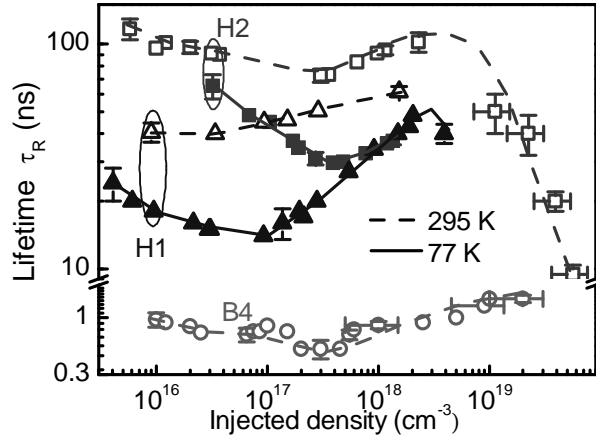


Fig. 5.1.3 Recombination lifetime τ_R vs. excess carrier density in three 3C-SiC samples. Dashed and solid line is the guide for the eye for injection dependences at 295 K and at 77 K, respectively.

(SRH) theory for a single recombination center in a forbidden gap can explain only S-shape (deep center) or a reverse S-shape (shallow center) dependencies [78]. The same theory for two non-interacting deep and shallow centers can explain mixed injection dependency which produces namely the Λ -shape. Such lifetime nonlinearity was demonstrated in p-type Si, where simultaneous recombination through the Fe interstitial impurity and the FeB acceptor-pair was observed [111, 112]. In addition, according to the SRH theory a lifetime peak should occur around the LL/HL transition ($\Delta n \sim n_0$) on Λ -shape injection dependencies. This contradicts the clear shift of the lifetime minima on V-shape in 3C-SiC to the higher Δn_{IN} values with decreasing temperature (Fig. 5.1.3), while the substantial n_0 reduction by factor of 1/20 is measured with decreasing temperature to 77 K in moderately doped n-type 3C-SiC [113]. The only case that justifies the apparent increase of lifetime as excess carrier concentration drops below intrinsic carrier concentration is that minority carriers are trapped, and hence, this is not considered as a SRH recombination process through deep defects [111, 114] as happens when the excess carrier concentration is higher than intrinsic ones. The latter case is strengthened by the experimental observation of almost identical values of peak concentration Δn_{PK} with saturated concentration Δn_S as excitation drops down in Fig. 5.1.3.

It is believed that recombination in 3C-SiC should occur through the defect level similar to the Z_1/Z_2 center detected in 4H-SiC [93, 95, 98]. This center originates from the carbon vacancy-related complexes on the cubic and hexagonal sites and dominates an intrinsic lifetime of the 4H-SiC polytype. Despite the complicated injection dependent nature of the center, which has three possible charge states, the constant HL-lifetime values are observed in 4H-SiC before up to the onset of the Auger recombination [97, 98]. We speculate that the V-shape dependency in 3C-SiC originates from the dynamic capture barrier for the majority electrons due to the lattice relaxation around the different charge states of this defect. In 4H-SiC polytype deep level transient spectroscopy measurements showed that the Z_1/Z_2 center has the large minority hole (recombination) capture cross-section $s_h \approx 10^{-14} \text{ cm}^2$ and two electron capture cross-sections of the order $s_e \geq 10^{-15} \text{ cm}^2$. In 3C-SiC the capture cross-sections are one order of magnitude lower [115]. Using these values and the simple $\tau_{\text{HL}} \approx (v_{\text{th}} \times s_e \times N_{\text{R}})^{-1}$ relation, where v_{th} is the thermal velocity ($\sim 2 \times 10^5 \text{ cm/s}$ at 300 K) and N_{R} is the defect concentration, we estimate that $N_{\text{R}} \approx 10^{14} \div 10^{15} \text{ cm}^{-3}$ in the H1 and H2 samples, and $N_{\text{R}} \approx 10^{16} \text{ cm}^{-3}$ in the B4 sample. These values are by one or two orders of magnitude higher than the ones observed in high quality 4H-SiC epilayers.

5.1.4 Conclusions

Density of carrier traps and recombination centers in n-doped bulk 3C-SiC have been determined from the saturation amplitude of differential transmittance transients and from the initial fast decay, respectively. The dominant carrier traps were ascribed to nitrogen impurities, while the recombination centers to carbon vacancy-related complexes. The apparent increase of lifetime, as excess carrier density was reducing towards to equilibrium carrier density, was attributed to carrier trapping. Moreover, the recombination on surface has shown negligible contribution on the total recombination rate for areas far from surfaces.

5.2 Carrier dynamics in 3C-SiC epilayers grown by sublimation epitaxy on different SiC substrates

5.2.1 Introduction

Several different growth techniques and substrates are used to manufacture 3C-SiC wafers [15, 116]. In all growth methods on Si or α -SiC substrates the formation of defects, either in the interface (misfit dislocations, inversion domain and twin boundaries) or during the growth (other polytype inclusions, stacking faults and twin boundaries) lead to low quality 3C-SiC layers [117]. The main difficulty with Si substrate is the huge lattice mismatch ($\sim 20\%$) [118] and the different thermal expansion coefficients ($\sim 8\%$) between the epilayer and substrate, which results in high defect concentration and wafer bowing. The hetero-polytypic growth of (111) 3C-SiC on (0001) α -SiC with negligible lattice mismatch ($\sim 0.1\%$) and identical thermal expansion coefficient offers a solution to mentioned problems by reducing the density of stacking faults (SF). However, another type of defect is introduced. During the growth of (111) 3C on (0001) 6H substrate two distinguishable orientations of epilayer rotated by 60° with respect to each other have equal probability. This is the origin of double-positioning boundary (DPB) [119]. At this point, a promising technique called Vapor-Liquid-Solid deposition (VLS) [119] gives a chance to develop a hetero-polytypic thin seed layer of 3C-SiC on which it would be possible to grow thicker layers homo-epitaxially by Chemical Vapor Deposition (CVD) [120] or Sublimation Epitaxy (SE) [121] techniques.

5.2.2 Samples and techniques

The samples under study are four (111)-oriented, $18\div 29\ \mu\text{m}$ thick 3C-SiC layers differently grown by sublimation epitaxy [63, 122]. Two layers (S1 and S2) are grown on as-received (sample S1) or re-polished (sample S2) 6H-SiC (0001) wafers. The other two layers are homo-polytypically grown on 3C-SiC (111) seed layers using VLS [123] (sample S3) or sequentially VLS and CVD [124] (sample S4) techniques. All samples, substrates and epilayers, are

presented in Fig. 5.2.1. The growth was performed in a radio-frequency (RF) heated graphite crucible into reactor [64] by sublimation of polycrystalline SiC source and deposition on a cooler substrate. The growth was carried out for 30 min at a source temperature of 2000 °C with 95 min ramp up from 1200 °C and a temperature gradient of 6 °C/mm under vacuum condition ($<10^{-5}$ mbar). To ensure a reasonable growth time the clearance between the source and substrate was kept at 1 mm by graphite spacer.

In order to obtain complementary information on epilayers we carried out Low Temperature Photoluminescence (LTPL) and Secondary Ion Mass Spectroscopy (SIMS) measurements for the determination of impurities density, High Resolution X-Ray Diffractometry (HRXRD) to assess the crystal structure, Nomarski interference contrast microscopy and Atomic Force Microscopy (AFM) operating in the tapping mode to examine the surface morphology, and profilometer to determine the layer thickness. LTPL measurements were taken at 5 K with the FreD laser at 244 nm wavelength with 30 mW power. The experimental conditions were 15 s for the acquisition time for samples S1/S2 and with 12 s time for samples S3/S4, with a grating of 600 gr/mm and slit opening of 30 μm . The laser beam diameter was approximately 100 μm . All epilayers are thin discs on rectangular substrate so the measurements were performed on the diameter of each sample. The SIMS measurements were taken with the Cameca-IMS4f and O^{2+} ion source. The impurity elements of interest were N, Al and B. In Table 5.2.1, we list the parameters for all samples under investigation determined by the above mentioned techniques.

Our study on the influence of SiC polytypic substrate on cubic SiC epilayer using sublimation epitaxy as an alternative growth way shows that surface morphology is strongly related to substrate polytype. The optical microscopy pictures (third column in Fig. 5.2.1) revealed domain character for the layers grown on (0001) 6H-SiC substrates and continuous character for the layers grown on 6H-SiC with (111) 3C-SiC seed layers. In the first case, the surface shows grooves between domains due to decreased local growth rate,

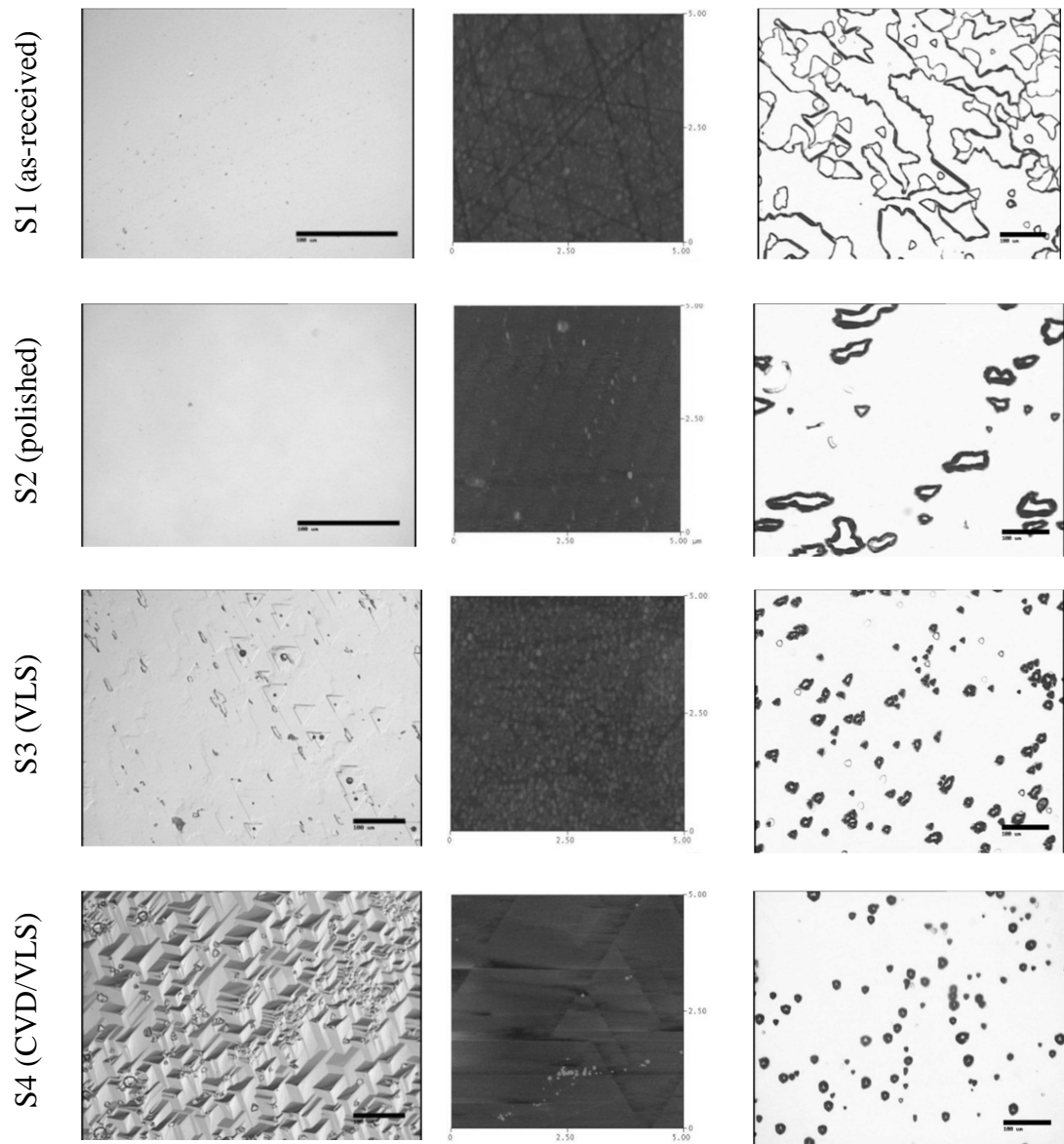


Fig. 5.2.1 Long (left) and short (middle) range roughness of as-received (0001) 6H-SiC substrate (first row), and, after extra polishing (second row). The right column shows their respective epilayer surfaces received by optical microscope.

while in the latter case, a specific pit-like defect appearance due to twinned areas is revealed by (AFM) images [122]. The heteropolytypic growth of 3C on 6H generates high density of twins (double positioning boundaries – DPB) and during SE the fourfold twinning centers have high probability to be formed at interface propagate through the whole layer terminating on the surface [125]. On the other hand, VLS growth mechanism promises vast reduction of twins [126]. It seems that in VLS seeded layers 6H-SiC inclusions are eliminated but

Table 5.2.1 Determined parameters for all (A-D) the 3C epilayers. 6H inclusions, layer thickness, and FWHM are taken from [122]. Dopants concentrations are the average values obtained by SIMS and LTPL.

Layer	S1	S2	S3	S4
Substrate	bare 6H	polished 6H	VLS 3C	VLS+CVVD 3C
6H inclusion (%)	2	0.2	0	0
Layer thickness (μm)	20	29	24	18
FWHM (111) (arcsec)	179	302	144	83
[N] ($\times 10^{17} \text{ cm}^{-3}$)	6	4	5	5
[Al] ($\times 10^{17} \text{ cm}^{-3}$)	5	10	9	9
[B] ($\times 10^{16} \text{ cm}^{-3}$)	0.2	4	2	3

twins still exist. The surface non-homogeneity of sublimation layers grown on VLS seed layers might be attributed to VLS seed layers quality since they were exhibiting some defects and non-wet zones. Thus, the amount of structural defects in these layers is strongly affected by the VLS seed layer.

5.2.3 Results and discussion

DT measurements were performed by 351 nm wavelength excitation generating carriers within entire epilayers but not in the substrate. The probe pulse was delayed either optically (i.e. by increasing the light path with the use of a motorized translation stage) or electrically (i.e. by a delayed triggering of the probe pulse). In the first case a ~ 10 ps duration pulse at 1053 nm wavelength were used with optical delay up to 4 ns, while in the second case a ~ 10 ns duration pulse at 1064 nm wavelength were used with electrical delay up to 200 μs . Applying the optical delay modification we are able to determine the very first “fast” carrier dynamics while with the use of electrical delay modification we are able to detect the very “slow” carrier processes (see Fig. 5.2.2). The term “fast” describes the extinction rate of carriers which are in non-equilibrium thermal conditions into the bands. These non-equilibrium carriers, generated by a short laser pulse, are responsible for the absorption of

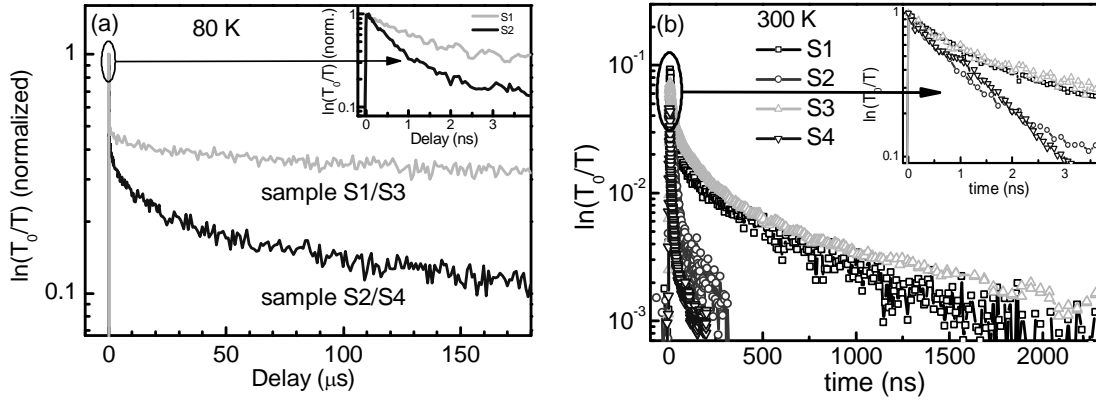


Fig. 5.2.2 DT kinetics of samples S1/S3 and S2/S4 at a) 80 K and b) at 300 K. In insets is presented the initial “fast” decay with ps time resolution.

the probe beam in the infrared range of wavelengths. Their decay lifetimes are ranging between several tenths of picosecond up to several microseconds with dependence mainly from the specific semiconductor material. In our 3C-SiC layers the “fast” decay lasts usually several nanoseconds. The “fast” decay in Fig. 5.2.2 is the peak at the “zero” delay time at the μs delay range, and is presented with more clarification in the insets. During the “fast” free carrier decay some of them fill the empty states into the forbidden band gap due to their ionization from the pump beam photons. These states are closely related to impurities present in the semiconductor lattice structure and we can describe them as carrier trap centers. When the excess non-equilibrium carrier density into bands vanishes only the trapped carriers are able to absorb the infrared wavelengths energy photons from probe beam. Usually, the absorption cross section of impurities is much higher than that of free carriers in the near-IR range of wavelengths [104]. As temperature decreases, the probability of carrier thermal excitation to the respective band is lowering, and hence, the cyclical process trapping-emitting become longer. As a consequence, the apparent lifetime of a trapped carrier is represented by a “slow” decay like in Fig. 5.2.2.

The dependence of τ_{slow} on temperature for all layers was investigated within the 80÷800 K range. In Fig. 5.2.2(a), it is presented the “fast” (in the inset) and the “slow” signal component of DT decay at 80 K for both samples.

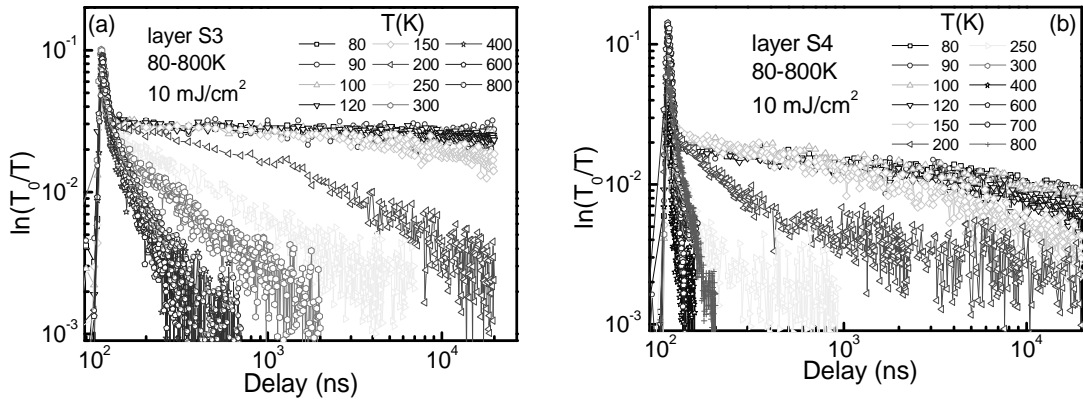


Fig. 5.2.3 Temperature depended DT kinetics for layer a) S3 and b) S4.

In the same way, the temperature dependence of the “fast” and “slow” decay in layers S1/S3 and S2/S4 are similar but not the same. In the case of layers S1/S3, as temperature increases above ~ 120 K, there is a progressive decrease of apparent lifetime due to decrease of trapped carriers concentration (see Fig. 5.2.3(a) for sample S3). On the other hand, in the case of layers S2/S4 the decrease is more prominent with its amplitude to vanishes faster than in layers S1/S3 (see Fig. 5.2.3(b) for sample S4). These two similar behaviors might be described by several distinctive elemental processes taking place in a wide band gap semiconductor material [81]. While the “slow” decay rate reflects the capture and/or emission processes at the traps, i.e. the time constant of the “slow” decay, other elemental processes, taking place at a trap level, influence the ratio of the “slow” decay to the “fast” decay, i.e. the amplitude of the “slow” component. In reality, the temperature dependence of “slow” decay is influenced by more than two elemental processes especially when a multitude of trapping energy levels is present in a compensated compound semiconductor. The increase of decay rate with temperature, which is practically the same for all samples, might be attributed, primarily to the majority carriers (holes) capture rate by the traps, and secondary to emission of trapped minority carriers (electrons) and their subsequent recombination with majority carriers at recombination centers. The above mentioned processes are strongly related with traps energy levels which, in principle, are not close to band levels. Concerning the amplitude of “slow” decay, this might be a

consequence of reduction of trap levels' occupation probability; minority carriers' (electrons) capture cross section is low enough in order to refill the empty states of thermally emitted majority carriers (holes). However, in our point of view, the most realistic interpretation on "slow" decay amplitude is related with recombination centers. The higher amount of recombination centers shifts the point of dynamic equilibrium to lower concentration of long-living trapped carriers. At high temperatures, carriers are thermally emitted from trap levels and thus the recombination rate increases. In an overall consideration of the temperature dependence of experimental DT "slow" decays we can conclude that the recombination centers concentration determines their amplitude, while the energy level of trapping centers their decay rate.

The same DT decay behaviors as at low temperatures have shown all samples at RT (Fig. 5.2.2(b)). It is clear that layers S1/S3 apart from the initial fast decay slope (inset in Fig. 5.2.2(b)) exhibits long decay tails for $\sim 2 \mu\text{s}$ time period, while layers S2/S4 apart from the initial fast decays exhibit weak long decay tails much shorter than S1/S3 layers (inset in Fig. 5.2.2(b)). This fast initial decay in the regime of moderate excitations is representative for the non-radiative recombination of free carriers through deep level recombination centers according to SRH model. Thus, S2/S4 layers contains higher amount of recombination centers than S1/S3 do, since non-radiative recombination rate is proportional to recombination centers concentration. Thus, the longer living carriers in layers S1/S3 are trapped and recombine progressively after their release to vicinal bands. From both diagrams at 80 and 300 K in Fig. 5.2.2 we can conclude that samples S2/S4 have higher concentration of recombination centers than sample S1/S3. As we will discuss later, the trap energy levels which are responsible for the long "slow" decays of DT kinetics are attributed to Al impurities.

We would like to draw attention to carrier lifetime, as it determined from the "fast" part of decay, as a function of temperature, $\tau_{fast}(T)$. The colored open symbols in Fig. 5.2.4(a) show $\tau_{fast}(T)$ for all samples; the dependence is

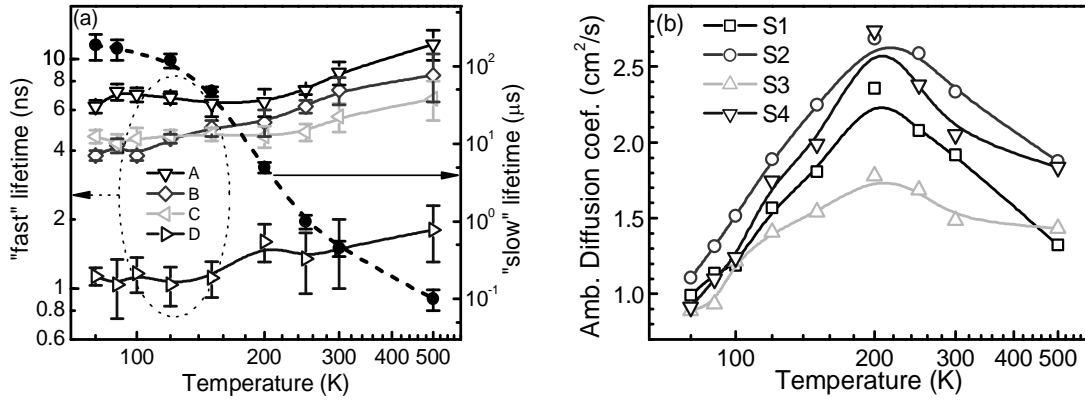


Fig. 5.2.4 Temperature dependence of a) “fast” and “slow” recombination lifetimes, and b) ambipolar carrier diffusion coefficient D_a .

qualitatively similar in all samples. The observed tendency can be attributed to diffusion-limited carrier recombination at extended defects, observed recently in thick SiC and GaN layers [127, 128]. Latter model presumes that lifetime is limited by carrier diffusion to domain boundaries [129, 130]. This process becomes increasingly important above ~ 200 K when carrier mobility reduces due to carrier scattering on acoustic and optical phonons (Fig. 5.2.4(b)). Consequently, free carriers spend more time in inter-structural-defect space before recombine on them, since the recombination on isolated point defects has much lower probability. It seems that the above described model, in our case, does not retain its validity, since SRH recombination processes in SiC performed mainly on deep level recombination states like Z1/Z2 strongly connected with carbon vacancies and interstitials, i.e. intrinsic point defects. Thus, the increase of lifetime at elevated temperatures might be not attributed to the decrease of SRH recombination rate on boundaries but to thermally emitted carriers from traps. Our latter consideration is enforced by experimental results for lifetime at temperatures lower than 200 K where only a small decrease is exhibited when ambipolar diffusivity tends to saturate as temperature drops down and trapped carriers have very small probability to be thermally emitted. Since overall SRH recombination rate is partially dependent on diffusion coefficient, i.e. partially diffusion limited, we can derive that the carrier recombination on extended defects is not the dominant recombination

mechanism, but still is important since the general trend for extended defects, as individual entities, is to gather any kind of point defects on them and hence to increase their recombination effectiveness.

Lifetime values in all layers at RT seems that support the latter result: lifetime is shorter in layers with lower concentration of surface defects. As it is shown in last column of Fig. 5.2.1 layers S2 and S4 exhibit lower concentration of defects than layers S1 and S3 do, respectively. According to the latter, it seems that there is not any pronounced dependence of carrier lifetime on extended defect density. For this reason, DT measurements at RT are performed at several spots in all layers, as a “lifetime mapping”, where nonhomogeneous distribution of structural defects is evident even by a naked eye observation but most thorough layer inspection is done by an optical microscope (see pictures in Fig. 5.2.1 and Fig. 5.2.5). There are distinct macroscopic regions of different opacity on the samples surfaces due to different concentrations of structural imperfections which in the case of samples S1/S3 show groove character of domain boundaries [122]. The obtained τ_{fast} values differ for several times in areas with different concentration of domain boundaries (Fig. 5.2.5(a)). In the case of samples S2/S4 the decay is faster at areas with higher concentration of pit like defects but the effect is not so pronounced as in the case of domain boundaries (Fig. 5.2.5(b)). According to this “lifetime mapping” in all samples, we can derive that areas with higher concentration of structural imperfections increases the carrier recombination rate. The increase of extended defects density on the samples surface results in the recombination rate increment, pointing out that extended defects, in particular domain boundaries contribute significantly to recombination rate but this contribution has rather a secondary role in the overall recombination rate.

Going back to Fig. 5.2.4(b) it is presented the ambipolar diffusion coefficient (D_a) for all samples after the evaluation of the experimental LITG kinetics in the 80-500 K temperature range. We will discuss our results with respect to surface morphology, i.e. domain boundaries (for samples S1/S3) or

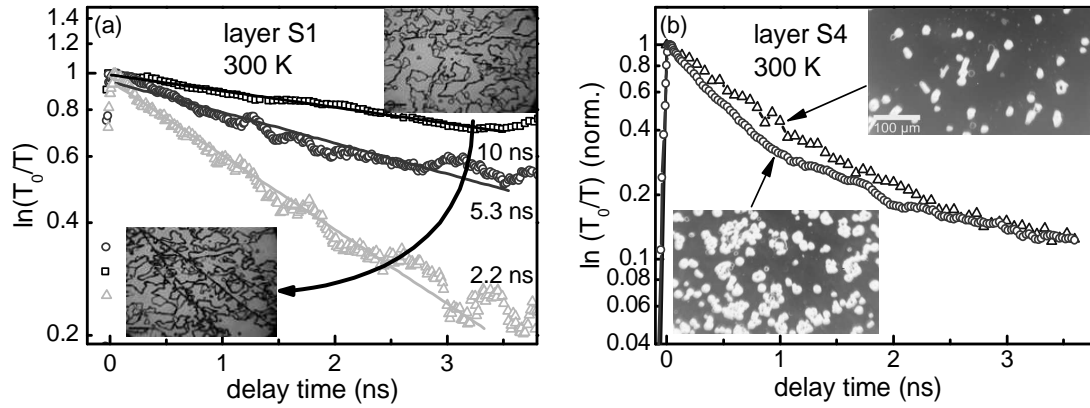


Fig. 5.2.5 DT kinetics at RT as a function of domain boundaries (a), and pits (b), density.

pit-like defects (for samples S2/S4). For samples S1/S2 we can notice that in whole temperature range sample S2 shows higher values of D_a than sample S1 does. If we take under consideration the optical microscopy pictures in transmission mode, depicted in the last column of Fig. 5.2.1, we can see that the domain character for both layers is obvious. Domain grooves on epilayer surface is an indication of domain boundaries, mainly twins, in the interior of epilayer. It was noted [131] that, a strong increase in the concentration of various defects is observed at twin boundaries in 3C-SiC epitaxial films grown on 4H-SiC substrates [132]. Correlating the ambipolar carrier diffusivity (D_a) with the grooves (twins) density we see that S1 layer (with high groove density) exhibits lower D_a than S2 (with lower groove density). It seems that carriers diffuse faster along channels with lower scattering probability, while, the diffusivity across structural defects is reduced since carrier faces the potential barriers that have been introduced by defects in the long range 3C-SiC lattice periodicity. The later plays an important role in carrier mobility as domain boundaries are extended from the interface towards to surface in an almost perpendicular direction, and hence, carriers that diffuse along grating vector have to overcome their potential. Similar consideration we might do for the case of samples S3 and S4. In this case we might claim that the 3C-SiC layer S4 grown by SE on VLS+CVD seed layer contains less extended structural defects than layer S3 grown on VLS seed layer but its recombination

centers are more effective. Thus, even if the apparent electronic properties indicate that the successive growth of thin VLS and CVD layers deteriorates the crystal quality, the deeper reasons remain identified.

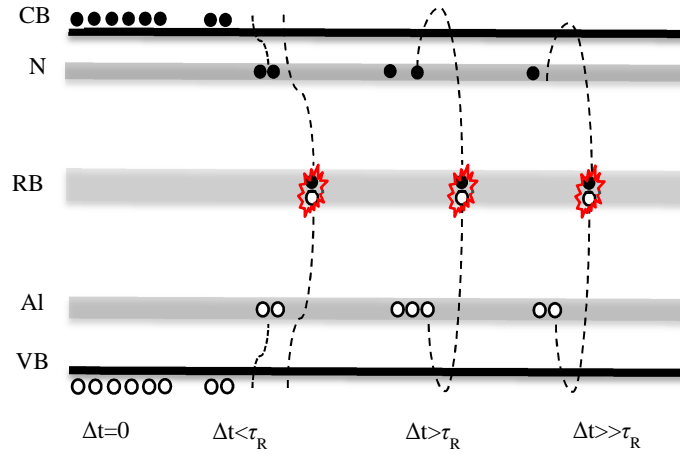


Fig. 5.2.6 Schematic representation of carrier trapping evolution.

As we have already discussed earlier, the temperature effect on long “slow” decay tails shows an impressive quenching as the temperature increases. When temperature is below ~ 120 K and the thermally excited trapped carriers are suppressed, all layers show similar DT transients consisted from a fast and a very slow decay component. While the initial fast free carrier recombination rates remain practically constant as temperature increases, the long “slow” decays become faster with temperature. It is clear that the “slow” decay is described by more than one exponential function where each of them represents an independent mechanism. Fitting with two- or three-exponential functions each one of “slow” decays we may derive information for two or three independent mechanisms related to different trapping centers. However, the uncertainty that is introduced by several experimental parameters cancels any practical use of a multi-exponential fit. In the next paragraphs we will deal with time constant values considering a single exponential fit at delay times where, in a good approximation, we can describe them as single-exponential decays. These single-exponential decays are attributed to a trap energy level into the band gap. Scheme in Fig. 5.2.6 gives a time depended representation of trapped carriers responsible for the “slow” decay component.

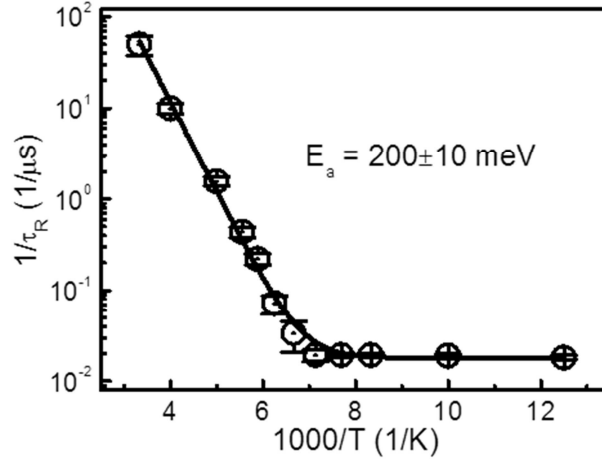


Fig. 5.2.7 Arrhenius plot of trapped carrier lifetime (long tails). The determined thermal activation energy $E_a = 200 \pm 10$ meV is attributed to Al impurities.

Since a dominant impurity state in band gap is responsible for the temperature depended long tails of DT transients, we can determine its thermal activation energy, and hence, its chemical nature. The slow component of the DT transients at $T < 120$ K provide carrier lifetime values up to the order of hundreds of microseconds for layer S3 and several times lower for layer S4. All impurities as temperature increases reduce the average time that they can keep trapped a carrier and hence the DT transient is accelerated [91]. Plotting in an Arrhenius diagram (Fig. 5.2.7) the inverse of mono-exponential long decay lifetimes versus the inverse of temperature we obtain the impurity thermal activation energy to be $E_a = 200 \pm 10$ meV. This value approaches the thermal activation energy of Al impurity in all SiC polytypes [133, 134]. Moreover, even the ionization energy of Al it is not precisely determined it has a value of approximately 270 meV [22]. According to Haynes rule for acceptors the Al-bound exciton binding energy E_{AIBX} is determined by [135]:

$$E_{BAX} = -14.9 \text{ meV} + 0.16E_A \quad (5.1)$$

where E_A is the acceptor ionization energy. For Al acceptor in 3C-SiC the E_{BAX} is approximately 28 meV. Moreover, several theoretical models [84] are proposed on the concentration and compensation dependence of thermal activation energy of impurities in a semiconductor material. The models that have better coincidence with experimental results for semiconductors with high

degree of compensation are based on the concept of electrostatic interaction between the free carriers and the oppositely charged impurity centers [82, 83] and improved by the introduction of the carrier distribution relaxation effect on the impurities centers [85]. Thus, the reduced thermal activation energy is determined according to Debye and Conwell model [82] relation:

$$E_{Al} = E_{Al_0} - \alpha \sqrt[3]{N_{Al}} \quad (5.2)$$

where α is related to compensation degree K as $\alpha=f(K)(e^2/4\pi\epsilon_0\epsilon_r)$, with ϵ_r the static dielectric constant. The reduction of Al thermal activation energy in our layers is 40 meV approximately. In total an energy difference of 68 meV of Al state energy from the top of valence band results that the Al thermal activation energy is approximately 202 meV. This value is in agreement with ours value determined by Arrhenius plot for layer compensation degree $K\approx 1$, since now $f(K)\approx 2.5$ and $\alpha=(4.0\pm 0.5)\times 10^{-5}$ meV, which is valid for acceptors in the frame of Debye and Conwell model [82].

Since the amount of thermally ionized carriers from trapping centers at low temperatures is negligible the resulted modulation absorption coefficient (or differential transmittivity) reflects the concentration of electrically active centers. The induced absorption coefficient modulation, $\Delta\alpha$ (or DT), as a function of induced excess carrier density, ΔN , (excitation) at delay times longer than the free carrier lifetime may derive the amount of carrier trapping centers concentration in the material [91, 104]. This happens because all remaining carriers, after the mutual annihilation, are been trapped and progressively have filled the available trapping sites in layer's volume. If, in the general case, we consider a semi-infinite layer, the site filling can be described by a log-log diagram of DT signal ($\ln(T_0/T)$) vs. excess carrier concentration (ΔN), usually called exposure characteristic (EC). In this diagram, the $\ln(T_0/T)$ vs. ΔN curve can be distinguished in two ranges: a linear and a logarithmic. In the linear range, site filling is following the excitation since all induced free carriers are progressively trapped at sites. In logarithmic

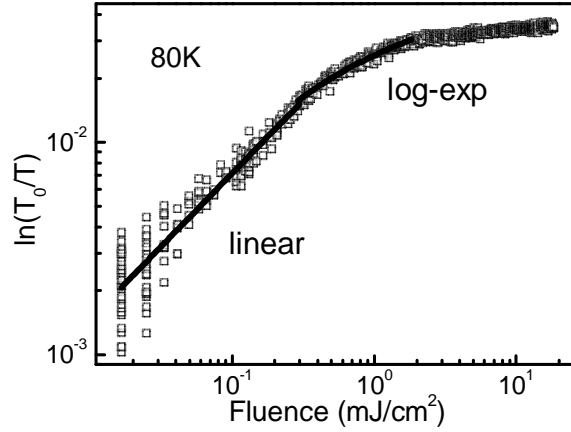


Fig. 5.2.7 Determination of electrically active traps by fitting with eq. (3) (linear left part) and (4) (logarithmic and exponential right part).

range, the excess carrier concentration is exceeding the trap density and hence some of them recombine.

When a layer with finite thickness d is under consideration, then the DT signal is a function with several parameters, like, layer's trap filling, interface recombination velocity and energy band gap mismatch, and substrate nature. In this case, analytical calculations are becoming very complicated and approximations are needed. In the simplest case, which satisfies the specific 3C/6H interface conditions, we can consider that the trap filling into 3C layer's finite thickness is the dominant phenomenon that modulates absorption coefficient and all other influences have to be avoided. Hence, the DT signal can be described by a couple of equations for linear and non-linear ranges as:

$$\ln\left(\frac{T_0}{T(t)}\right) = \sigma_{trap} \int_0^d \Delta N(z, t) dz \quad \text{for } \Delta N_0 < P_{trap} \quad (5.3)$$

for the linear range, and

$$\ln\left(\frac{T_0}{T(t)}\right) = \sigma_{trap} \times \frac{P_{trap}}{\alpha} \times \left(1 + \ln\left(\frac{\Delta N_0}{P_{trap}}\right) - \exp\left(-\alpha \times \left(d - \frac{\ln\left(\frac{\Delta N_0}{P_{trap}}\right)}{\alpha}\right)\right) \right) \quad (5.4)$$

for $\Delta N_0 \geq P_{trap}$

Table 5.2.2 Determined parameters for all (S1/S2/S3/S4) 3C-SiC layers: layer

thickness, average Al concentration obtained by SIMS, average value of free carrier lifetime (τ_R), as well as, carrier capture cross section (σ_{trap}) and electrically active traps concentration (P_{trap}) obtained for surface lower and higher defected areas.

Layer		S1	S2	S3	S4
[Al] (by SIMS) ($\times 10^{17} \text{ cm}^{-3}$)		5	10	9	9
σ_{trap} ($\times 10^{-17} \text{ cm}^2$)	Less defects	3.4	2.7	2.5	3.0
	More defects	2.2	2.5	2.0	1.6
P_{trap} ($\times 10^{17} \text{ cm}^{-3}$)	Less defects	3.7	8.2	7.8	8.6
	More defects	5.6	9.3	8.6	9.1

for the non-linear range. ΔN_0 is the initial generated free carrier density, α is the absorption coefficient of excitation wavelength, σ_{trap} is the probe beam photon absorption cross section, and P_{trap} is the electrically active traps concentration. Moreover, as longer the material is from “semi-infinite layer” criterion, i.e. smaller thickness, so the non-linear part of exposure characteristics (EC) deviates from the logarithmical increase described by the eq. (4) and tends to saturation. The trap density derived by the above described method is strongly correlated to the electrically active impurities centers, donors and/or acceptors. Special attention has to be taken for the appropriate temperature regime in order the trapped carriers to have negligible probability for thermal excitation. A representative fitting process by the above equations on the experimentally obtained EC at 80 K is given in Fig. 5.2.7. The same process was applied at all samples for both, lower and higher, defected areas on the surfaces. The results are depicted in Table 5.2.2. The determined values of electrically active traps concentrations of all samples are in very good agreement with the average Al doping concentration determined by SIMS. The latter leads us to consider Al (ionized) impurities as the dominant carrier (hole) traps. The slightly higher values of carrier traps that are determined at higher defected areas than at lower ones, in all layers, might be a consequence of Al atoms tendency to diffuse and aggregate on them.

5.2.4 Conclusions

The carrier trap concentration in a 3C-SiC layer with finite thickness was determined by fitting the DT exposure characteristics recorded at low temperatures, where the carriers remain trapped for a longer time than the lifetime of free carriers. Traps nature was ascribed to aluminum impurities.

Domain boundaries in 3C-SiC even they contribute to trap-assistant recombination rate it seems that they have not the dominant role as other recombination centers.

Chapter 6 Carrier dynamics of differently grown 3C-SiC layers

This chapter is related to MANSiC project [136] since the majority of samples under investigation have been grown by its partners. The scientific aim of the MANSiC project was to develop a full technology based on high quality 3C-SiC thin or bulk material grown by different techniques. The simultaneous growth from different regions leads to a common problem – a nucleation of twin structures with formation of defects at their boundaries, what remains one of the main difficulties in 3C-SiC heteroepitaxy growth. In order to achieve the aim of single-domain layer a well-established VLS (vapor-liquid-solid) technique with remarkable results was accepted as a promising tool for a partial solution to this problem [123, 137, 138]. 3C-SiC layers grown by VLS technique, in turn, were used for further layer thickening with the application of several growth techniques like chemical vapor deposition (CVD), sublimation epitaxy (SE) and continuous-feed physical vapor transport (CF-PVT). In parallel, the same techniques were used for the direct growth on 6H-SiC polytype without the seed VLS layer. Our task, among the other characterization techniques, was to give a feedback to growth specialists in order to improve material quality.

This chapter is divided into six subchapters. Each one of the first five subchapters is dealing with a special feature of growth process which influences the electronic properties of epilayer: pre-growth purification, twins density, growth temperature, substrate type, seed layer. The last one deals with the tendencies of electronic properties of 3C-SiC grown by all available techniques.

6.1 Reflections of VLS growth conditions on epilayer properties

6.1.1 Introduction

One of the questions that arise during the growth of 3C-SiC is if the nitrogen-induced 3C stabilization is effective whatever the growth technique is used. The answer is probably negative. As it is reported, N has low incorporation during CVD [124, 139] or CF-PVT [66] techniques. This means that the nitrogen incorporation is not essential to stabilize the cubic phase. On the contrary, when the growth conditions are not favoring the cubic phase, like in the case of VLS process, high concentrations of N impurities ($\sim 10^{20} \text{ cm}^{-3}$) in the interfacial layer help to avoid the homoepitaxial growth [56].

It is believed that the most significant parameter affecting 3C stabilization in VLS process is the out-gassing of the crucible, as used in as it is called “ultra-high purity” (UHP) procedure [56]. This means that the nitrogen atoms released by the crucible are very important for the formation of 3C-SiC polytype. The stabilizing effect of N_2 impurity should thus occur during the early stages of growth, i.e. nucleation and islands enlargement. This is confirmed by the detection of a highly doped 3C interfacial layer, even for layers grown with simple “high purity” (HP) procedure, comparing with the low doping in the upper part of the layer. As a general rule, each time 3C-SiC is obtained by VLS growth the first hundreds of nm contains always a high amount of N impurities. As a consequence, the true VLS growth, starting upon adding propane in the gas phase, should happen only after the most important step governing 3C stabilization. It is believed that the final polytype proportion inside the grown layer is simply an image of the one on sample surface at the moment when propane is added inside the reactor. On the other hand, it is reported [48] that an effect of polytypism of SiC is the appearance of transition layers during the growth. Some times in the initial steps of the growth of one polytype on top of another, as is the case of growth of the cubic polytype on top of hexagonal substrates, there have been observed a transition step of a homoepitaxial layer and then achieving the cubic polytype. In some other cases

this happens with an addition of another polytype, just after the homoepitaxial step, that has a smaller band gap than the substrate polytype but higher than the cubic polytype, before finally reaching the cubic polytype.

6.1.2 Samples and techniques

In order to study the effect that has the UHP procedure in comparison with the simpler HP on electrical properties of thin n-3C-SiC(111) layers grown on Si-face 6H-SiC(0001) substrate by VLS technique we have performed measurements using optical pump–probe techniques like LITG and DT. The non-conventional vapor-liquid-solid (VLS) technique using Si-Ge melt is described extensively in Ref. [68]. The growth conditions and the main characteristics of the samples are summarized in Table 6.1.1. The layers properties were complementary investigated by other optical means. The thickness of the 3C-SiC layers was deduced from the interference fringes of the reflectivity μ -IR spectra. The layers morphology and surface quality have been characterized by Nomarski optical microscopy, while the polytype identification were performed by μ -Raman spectroscopy equipped with an Ar laser beam ($\lambda=488$ nm) with a spot of few μm^2 . A co-focal configuration was used to reduce the contribution of the substrate to the measured signal. In addition, doping concentration was determined by low temperature photoluminescence (LTPL) spectroscopy and secondary ion mass spectroscopy (SIMS) [140].

Table 6.1.1 The growth conditions and results obtained on these samples.

Sample	Growth procedure	Growth temperature (°C)	Thickness (μm)	[N] (cm^{-3})	[Al] (cm^{-3})
VU1 (VLS158)	UHP	1300	5.0 \pm 0.3	1.5 \times 10 ¹⁸	1 \times 10 ¹⁵
VU2 (VLS171)	UHP	1350	7.5 \pm 0.3	\sim 10 ¹⁸	\sim 10 ¹⁶
VH1 (VLS180)	HP	1300	8.0 \pm 0.5	1.5 \times 10 ¹⁸	2 \times 10 ¹⁵
VH2 (VLS105)	HP	1350	6.0 \pm 0.5	7 \times 10 ¹⁷	6 \times 10 ¹⁵

6.1.3 Results and discussion

In Fig. 6.1.1, the experimental results of SIMS measurements performed by MANSiC partners (Montpellier University II, France) are presented. In these diagrams is presented the in-depth concentration of several impurities for VU1 and VH1 samples. We can notice that N concentration exhibits an increase of more than two orders of magnitude (from $\sim 10^{18}$ to more than 10^{20} cm^{-3}) at the first hundreds of nanometers from the interface. The rest area up to the surface is showing almost a constant in-depth N distribution. The same procedure was applied at other points on each sample revealing an inhomogeneous lateral distribution (not shown) of impurities in all samples. SIMS results in all samples have shown a small decrease in N concentration far from the interface regions for the layers grown after the UHP procedure with respect those been grown by HP one, an obvious consequence of purification procedure. Nevertheless, the effect of HP/UHP procedure on N concentration at the first hundreds of nanometers from the interface is not clear. The fact of N incorporation in the early stage growth processes must be regarded as one of the parameters that contribute to the overall nucleation process, as well as to the island enlargement, since the obtained quality of the overgrown layer is determined from the transition layer between two polytypes. Although the mechanisms of entire process are unknown up to now, we might extract a conclusion about the contribution of purification procedure on the overgrown layer.

The determined the free carrier lifetime, τ_R , of sample VU1 grown by UHP procedure is longer in all temperatures (10-320 K) than that of sample VH1 grown by HP procedure (Fig 6.1.2(a)). This is also confirmed from room temperature free carrier lifetimes obtained by DT measurements for both samples (Fig. 6.1.2(b)). The small dispersion in values between the two diagrams in Fig. 6.1.2 is attributed primarily to the inhomogeneity of samples and secondary in experimental conditions. Despite the distribution in N concentration and in epilayer thickness laterally on samples the average lifetime values of sample VU1 exceed those of VH1 sample. As the free carrier

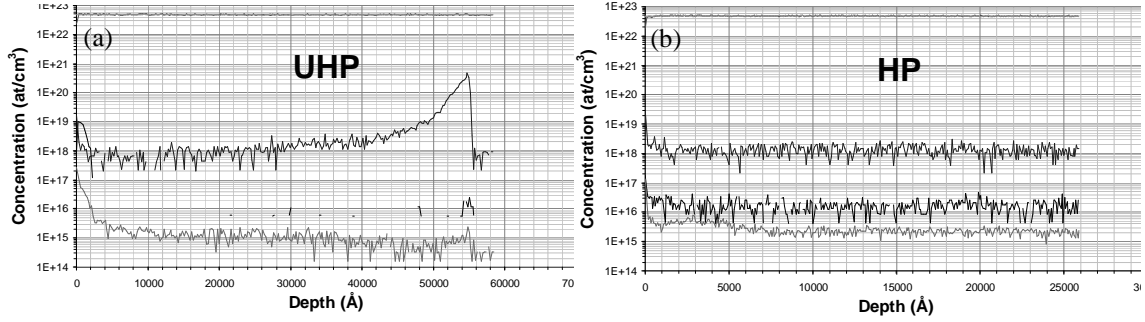


Fig. 6.1.1 SIMS measurements on VLS layers. a) UHP layer and b) HP layer

lifetime is a sensitive parameter that characterizes the material structural quality we can deduce that UHP procedure results in higher quality material than HP does. Moreover, we have to consider the contribution of transition layer to the overall 3C-SiC layer lifetime. The apparent lifetime is lower than the actual in this layer. This happens because of the higher contribution to the overall lifetime of highly doped ($\sim 10^{20} \text{ cm}^{-3}$) and defected interface [130]. The thinner the layer is the higher the interface contribution, as in the case of sample VU1.

Further measurements with DT technique have been done at RT in the 2-10 mJ/cm^2 excitation range for more samples grown by both procedures: two grown by UHP (VU1 and VU2) and two by HP (VH1 and VH2) technique. In Fig. 6.1.2(b) is plotted the average – after short mapping – lifetime with excitation for several samples. Since the amount of recombination centers is related to crystal lattice imperfection, we can deduce that UHP layers (VU1, VU2) have better quality than HP layers (VH1, VH2). This is justified by the fact that at low excitation regime (2 mJ/cm^2) the UHP layers exhibit higher lifetime values than HP layers. Moreover, as excitation increases, lifetime increases for both UHP layers but remains almost constant for HP layers. The given dependence of carrier lifetime on excitation energy density is attributed to the gradual saturation of carrier trapping centers [102]. This indicates that HP layers exhibit higher concentration of them than UHP ones.

In Fig. 6.1.3 is demonstrated the temperature dependence of ambipolar carrier mobility obtained from ps LITG measurements. Both layers have been

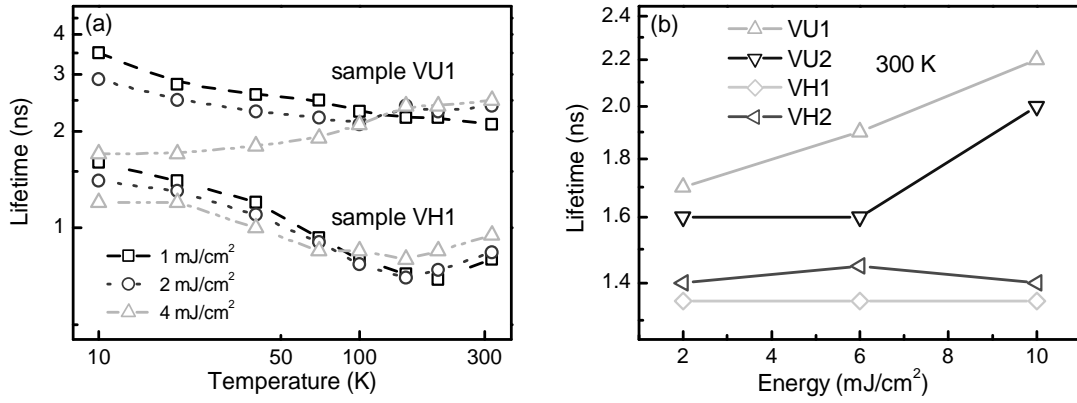


Fig. 6.1.2 a) Free carrier lifetime as a function of energy and temperature for an UHP (sample VU1) and a HP (sample VH1) obtained by LITG technique. b) Free carrier lifetime as a function of excitation at RT for UHP (samples VU1, VU2) and HP (samples VH1, VH2) obtained by DT technique.

excited at the same energy densities (1-4 mJ/cm²). At lower temperatures (<100 K) the HP layer (Fig. 6.1.3(b)) shows a saturation with excitation energy density. On the other hand, at the same temperature range, UHP layer (Fig. 6.1.3(a)) increases progressively its values with excitation energy density. This effect is attributed to ionized impurities screening from the induced excess free carriers [72]. As in the case of free carrier lifetime in the previous paragraph, the interfacial, highly doped area, still has a significant contribution to carrier transport. From the ambipolar carrier mobility at these temperatures we can deduce that UHP layer shows slightly higher values than HP when ionized impurities are completely screened. At higher temperatures (>100 K) the carrier scattering from lattice acoustic deformation phonons is more pronounced in HP sample resulting in faster reduction of ambipolar free carrier mobility. This last is a further indication about the superiority concerning the layer lattice structure. According to the simple relation $1/\mu=1/\mu_{\text{lattice}}+1/\mu_{\text{impurities}}$ [141] that describes the free carriers' mobility in a semiconductor and since $\mu_{\text{impurities}}$ is approximately the same for both samples we can deduce that the μ_{lattice} determines the total mobility at temperature higher than 100 K. The above experimental results in ambipolar carrier diffusivity for UHP and HP

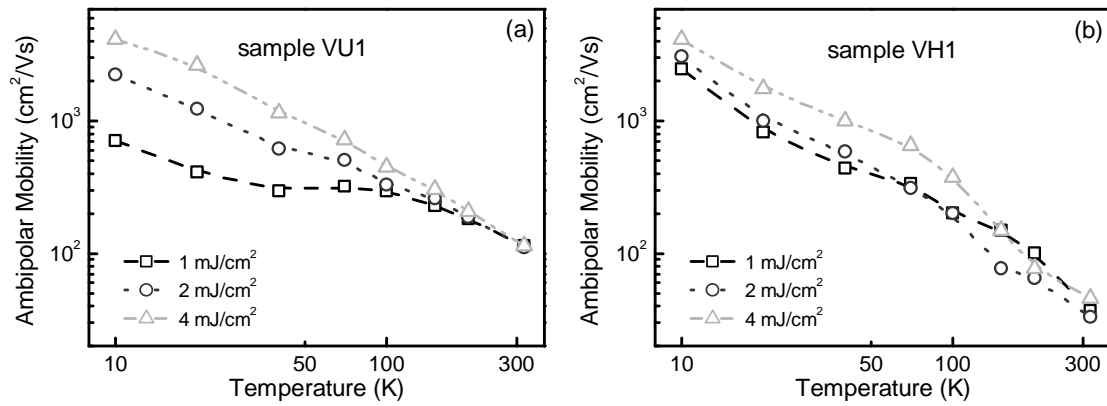


Fig. 6.1.3 Temperature depended ambipolar carrier mobility for an UHP (sample VU1) and a HP (sample VH1) VLS layer. Both cases are also a function of excitation energy density.

layers in 10-320 K temperature range indicate that the UHP layer has optimized structural properties with respect the HP one.

6.1.4 Conclusions

Thin 3C-SiC layers grown by VLS technique after UHP procedure have better electrical quality (contain less defects), which is indicated by 30-150 % longer carrier lifetime and two times higher mobility if compared to those produced after HP procedure.

6.2 Electronic properties of high growth rate sublimation epitaxy of 3C-SiC

6.2.1 Introduction

The following paragraphs aim to reveal the effect that has on growth by high rate sandwich SE [63] on Si face on axis 6H-SiC substrate, both the temperature and nitrogen atmosphere on free carrier lifetime and ambipolar mobility of overgrown bulk layers.

6.2.2 Samples and techniques

Two series of samples are grown at vacuum (10^{-5} mbar) and at N_2 (1 mbar), respectively. Table 6.2.1 provides the information about growth temperature and rate as well as resulted layer thickness and doping. The 3C-SiC was always dominant in the vacuum case and it also shows the strong dependence between the growth temperature and the percentage of 3C coverage (Fig. 6.2.1). The 3C coverage increased to 97% at growth temperature of 1875 °C. On the other hand, in the N_2 containing cases, the 6H-SiC was dominant and the coverage percentage of 6H was more than 90% at similar growth temperatures. Moreover, the growth rate is much higher for layers grown in vacuum, and hence they have more than two orders of magnitude lower N impurities concentration, than layers grown in N_2 background ambient. It worth to notice that the increase of growth rate with temperature results in higher 3C-SiC coverage, and nitrogen is not favoring the cubic polytype growth. The former is possibly a result of metastable conditions that 3C-SiC growth needs and the latter is coming in contrast with the suggested model that declares that nitrogen improves the 3C-SiC polytype quality [126]. Despite that growth rate is increasing with temperature grain size becomes smaller.

Table 6.2.1 Growth conditions and N and Al doping concentrations obtained from LTPL spectra

Sample	Thickness (μm)	Growth T ($^{\circ}\text{C}$)	Atmosphere	Growth rate ($\mu\text{m}/\text{h}$)	[N] (cm^{-3})
SC1 (SE070)	155	1775	Vacuum (10^{-5} mbar)	310	9×10^{16}
SC2 (SE074)	238	1825		476	7×10^{16}
SC3 (SE076)	410	1875		820	2×10^{16}
SH1 (SE071)	26	1775	N_2 (1 mbar)	52	3×10^{19}
SH2 (SE073)	45	1825		90	3×10^{19}
SH3 (SE077)	100	1875		200	3×10^{19}

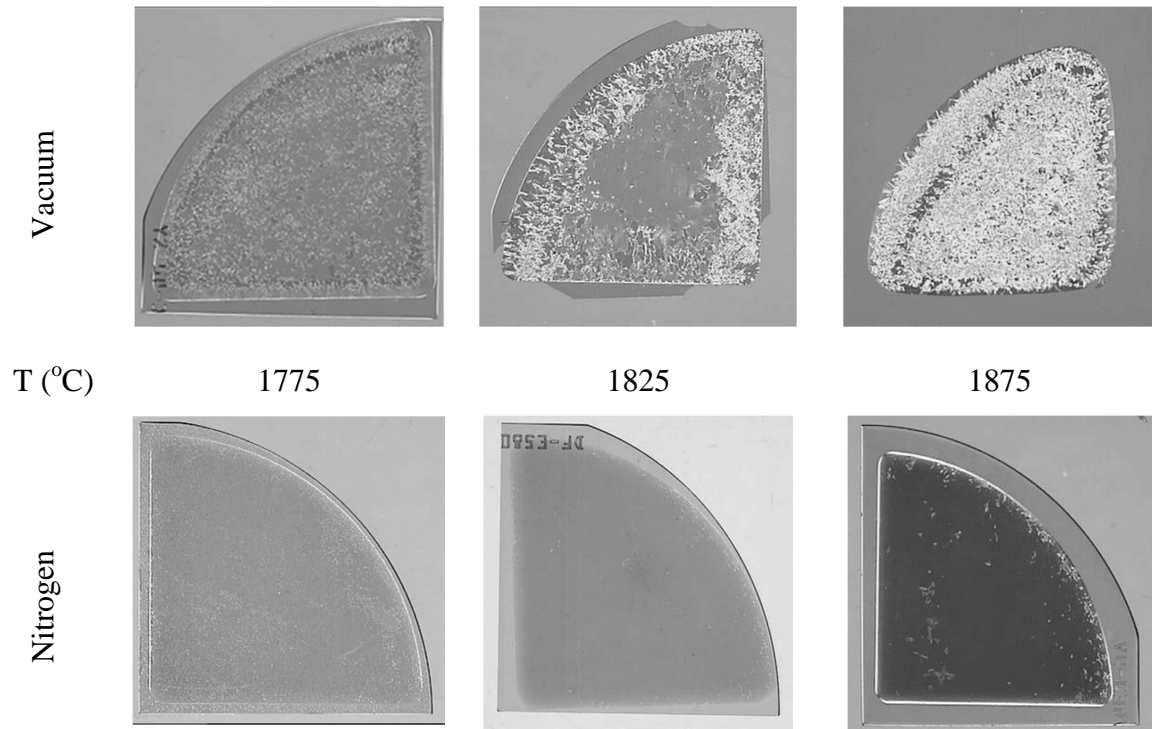


Fig. 6.2.1 Transmission micrographs of all samples under study. (from R. Vasiliauskas)

DT and LITG measurements have been done at room temperature (RT) and in the 80–800 K wide temperature range. For interband carrier injection we used a 10 ps duration $\text{Nd}^{+3}:\text{YLF}$ pulsed laser at 351 nm wavelength which creates an ambipolar carrier plasma in a $\sim 5\mu\text{m}$ penetration depth from sample surface. An optically delayed picosecond pulse at 1053 nm was used to measure the decay transients up to ~ 4 ns. A liquid nitrogen cooled cryostat operating at 80–800K temperature range was used for low-high temperature measurements.

6.2.3 Results and discussion

In Fig. 6.2.2 is presented the determined free carrier lifetimes for both series of layers, in vacuum and in N_2 ambient. The ps DT measurements at RT resulted in excitation independence carrier lifetimes in more than one order of magnitude excitation energy density range ($0.5\text{--}10 \text{ mJ/cm}^2$) at the high excitation regime. We also notice that lifetime increases with the growth temperature. Since free carrier lifetime is a sensitive parameter for material

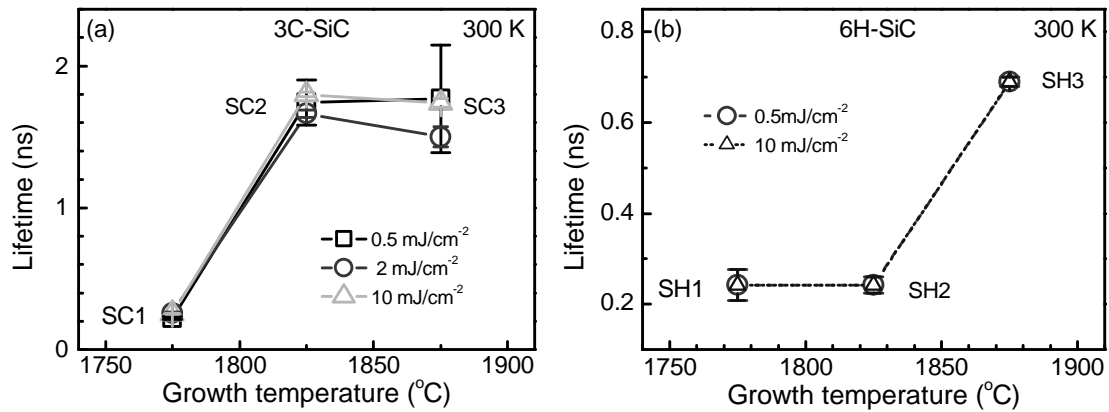


Fig. 6.2.2 Free carrier lifetime of SE 3C-SiC layers grown (a) in N₂ atmosphere and (b) in vacuum, as a function of growth temperature.

quality we can conclude that the higher growth temperature results in better crystalline quality both for mixed 3C+6H and pure 6H layers. In the case of mixed polytype layers grown in vacuum the optimum 3C-SiC growth conditions are when temperature is higher than 1825 °C but not exceed 1875 °C. At this temperature range the free carrier lifetime seems to saturate while grain size starts to decrease. In any case, lifetime values that correspond to optimum temperature conditions are approximately equal to the lower ones that layers grown by the same technique at higher temperature (2000 °C) but with one order of magnitude lower growth rate [122]. This difference in growth rate is a consequence of temperature gradient between source (powder) and target (seed) and in the case of sample SC3 was three times higher. In the case of the growth in N₂ ambient we can only notice that lifetime increases with the growth temperature but we cannot determine any temperature where lifetime saturates because of limited sample growth temperature that are available. In this case we see that growth rate increases as happens in the case of growth in vacuum but is still much lower from the respective temperatures.

As SC3 is the sample with the higher coverage of 3C on 6H substrate we have study its non-equilibrium carrier dynamics by applying a picosecond LITG technique in 80-800K temperature range. As diagram in Fig. 6.2.3(a) shows, lifetime exhibits a small decrease as temperature increases from 80 K to

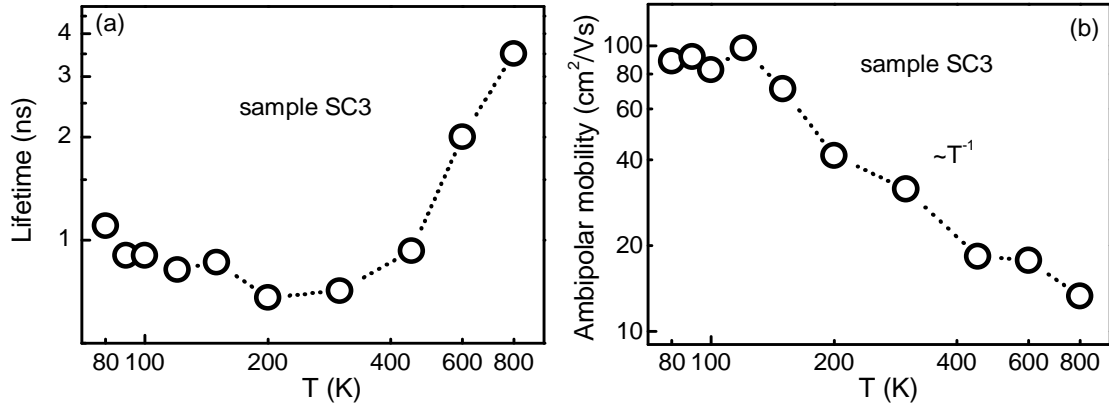


Fig. 6.2.3 Temperature dependence of a) free carrier lifetime and b) ambipolar mobility, at 0.5 mJ/cm^2 excitation energy density of sample SC3.

RT and a substantial increase as temperature increases above 400 K. At the same time ambipolar mobility in Fig. 6.2.3(b) saturates at approximately 120 K and has a plateau up to 80 K, probably due to carrier scattering on ionized impurities. In any case, both lifetime and mobility of sample SC3 are much lower than those of low rate sublimation layers (see section 5.2.3). More precise, at 300 K carrier lifetime is approximately 0.8 ns and ambipolar mobility $30 \text{ cm}^2/\text{Vs}$. The discrepancies that have been observed between data in Fig. 6.2.2(a) and Fig. 6.2.3(a) are due to structural inhomogeneities across the surface. At temperatures higher than 300 K there is an increase in lifetime with temperature while there is a decrease in ambipolar mobility. This observed tendency can be attributed to diffusion-limited carrier recombination at extended defects, like domain and grain boundaries where intrinsic point defects like Z1/Z2 are gathered [47]. The role of extended defects is revealed by the increase of ambipolar mobility in whole range of temperatures with excitation when the ionized impurities have been totally screened by the excess free carrier plasma (Fig. 6.2.4(b)).

Moreover, we have done an excitation dependence study of ambipolar diffusion coefficient D_a at low-high temperature measurements. The results are presented in Fig. 6.2.4(a). D_a shows an exponential increase as the temperature drops down from RT. As one can see, the increase is a not only a function of

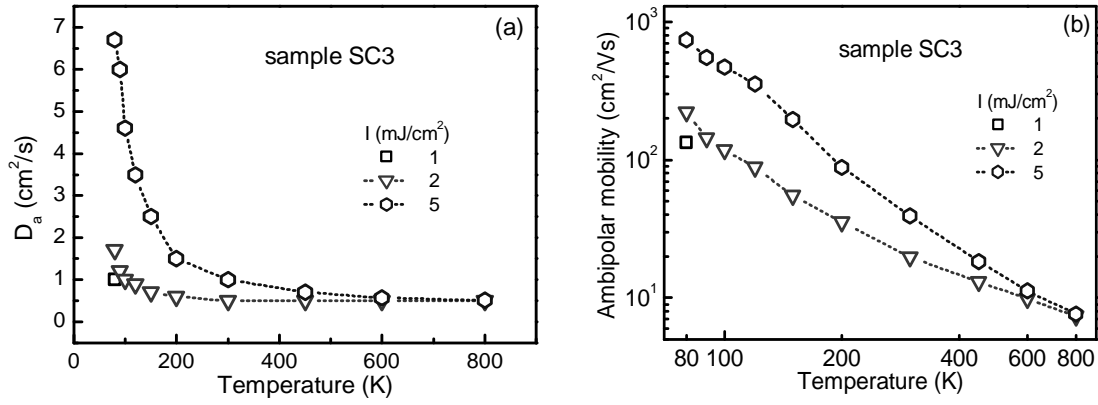


Fig. 6.2.4 Dependence of a) ambipolar diffusion coefficient and b) ambipolar mobility on temperature in sample SC3 at two excitation densities. There is an extra experimental point for 1 mJ/cm² at 80 K.

temperature but is also depends from excitation energy density, or else, from excess carrier concentration. This could be explained by the fact that at low temperatures the carrier plasma becomes more degenerated at the same carrier density, as effective density of states decreases. At temperatures lower than approximately 200 K the Fermi integrals ratio sharply increases and as $D_a(N)=D_{a0}[F_{1/2}(\eta)/F_{-1/2}(\eta)]$, where $\eta=(E_f-E_c)/kT$ is the argument in Fermi integrals, and hence lead to the increase of carrier diffusion coefficient [142].

6.2.4 Conclusions

1850 °C is the optimal temperature for the high growth rate of heteropolytypic sublimation epitaxy of (111) 3C-SiC on (0001) 6H-SiC in vacuum, in terms of the longest carrier lifetime. Effective lifetime is governed by diffusion-limited carrier recombination processes at extended defects, like domain and grain boundaries where intrinsic point defects like Z1/Z2 are gathered.

6.3 Study of homoepitaxial CVD 3C-SiC on VLS seed layer

6.3.1 Introduction

In this work we present the photo-electrical properties of 3C-SiC(111) layers grown homoepitaxially by CVD on VLS seeds in relation with their structural properties, doping features and applied growth parameters. In order to achieve this we applied time-resolved optical techniques such as the differential transmittance (DT) and light induced transient grating technique (LITG).

6.3.2 Samples and experimental techniques

The 3C-SiC layers were produced in two steps. The first step was the heteroepitaxial deposition of 3C-SiC(111) on on-axis 6H-SiC(0001) Si-face substrates using VLS approach based on Si-Ge melt at 1400-1250 °C [68, 123].

Homoepitaxial growth on such seeds was performed in a vertical CVD reactor under atmospheric pressure at 1500-1600 °C. The precursor gases were SiH₄ and C₃H₈ diluted in H₂ [143]. Some growth parameters are given in Table 6.3.1. The morphology and surface quality of the layers were characterized by the Nomarski optical microscopy (Fig. 6.3.1). The polytype identification and the evaluation of carrier concentration were investigated by μ -Raman

Table 6.3.1 Parameters of CVD homoepitaxial growth procedure and some characteristics of the grown layers.

Samples	Growth	Thickness [μm]	RMS	Doping level
	Temp. ($^{\circ}\text{C}$)	VLS+CVD	[nm]	[cm^{-3}]
CL1 (SG125)	-	0.2 + 3.3	-	5×10^{16}
CL2 (VLS42)	1500	1.8 + 5.2	-	8×10^{16}
CL3 (VLS50)	1500	1.8 + 6.4	-	5×10^{16}
CL4 (VLS86)	1500	1.8 + 6.2	-	7×10^{17}
CN1 (E621)	1600	3 + 10.5	12.3 ± 5.4	5×10^{17}
CN2 (E623)	1550	3 + 10.5	18.6 ± 7.4	$< 10^{15}$
CN3 (E625)	1550	3 + 10.5	1.8 ± 0.5	4×10^{17}

spectroscopy. Moreover, other techniques were used for the layers doping determination (LTPL, SIMS) and thickness (μ -IR). The 3C-SiC epilayers' roughness (RMS) was measured by atomic force microscopy. The structural properties of sample CN1 were also investigated by X-ray diffraction (XRD) reciprocal space mapping, as explained in [144].

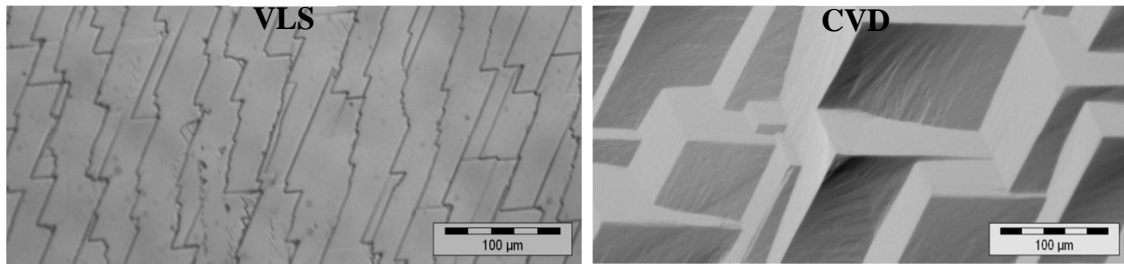


Fig. 6.3.1 Typical surface morphology of 3C-SiC(111) layers grown by a) VLS mechanism and b) thickening by CVD.

6.3.3 Results and discussion

Samples CL1, CL3, CL4

The RT free carrier lifetimes for the three (CL1, CL3, CL4) heterostructures as a function of excess carrier density ΔN are depicted in Fig. 6.3.2(a). There was a good agreement in lifetime values obtained by LITG (full symbols) and DT (open symbols) techniques. Carrier lifetime for sample CL3 provided nearly constant value of $\tau_R \approx 3.8$ ns, while for sample CL4 lifetime increased from 2.6 to 4.4 ns with increasing excess carrier density.

We note that these measurements were performed at high injection conditions, when electron and hole densities are equal and therefore, extending the Shockley-Read-Hall (SRH) model, carrier lifetime can be represented as $\tau_R \approx \tau_e \gg \tau_p$ [145]. According to this model, the lifetime should not be dependent on excitation at given high injection conditions ($\Delta N \gg n$) (i.e. at condition of trap saturation). Indeed, this model was found to be valid for samples CL3 and CL1 that have the lower free carrier concentration. For the sample CL4 (with higher carrier concentration), the trap saturation regime was achieved at

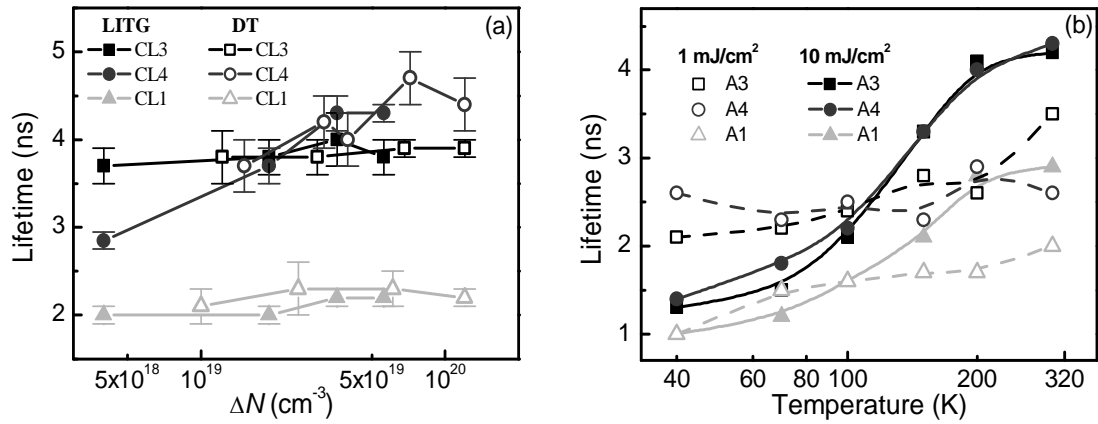


Fig. 6.3.2 Free carrier lifetime as a function of a) excess carrier density, and, b) temperature at 1 and 10 mJ/cm². Full and open symbols in diagram (a) indicate values obtained by LITG and DT techniques, respectively.

$\Delta N \geq 5 \times 10^{19}$ cm⁻³. Concerning the sample CL1, its τ_R values were constant (~2 ns) in all excitation range. We note that carrier dynamics in this – rather thin – layer (~3.5 μ m) was influenced by the short lifetime of 6H-SiC substrate ($\tau_R \approx 1.1$ ns) since the pump beam created carriers both in the epilayer and the substrate.

Carrier lifetime dependences on temperature and excitation are depicted in Fig. 6.3.2(b). At lower excitation (1 mJ/cm²), the carrier lifetime remained nearly constant with increasing temperature and pointed out that high injection conditions are valid within this temperature range (as the n value decreases at lower temperatures). However, at high excitation (10 mJ/cm²), the lifetime increased for all samples at RT and especially for the sample CL4, in agreement with the results in Fig. 6.3.2(a) indicating the gradual saturation of carrier trapping centers [102]. At high excitation conditions ($\Delta N > 10^{19}$ cm⁻³), τ_R value gradually decreased with lowering temperature and reached the value of ~1 ns in all samples. This might be a consequence of carrier thermal emission limitation from trapping centers. On the other hand, it can be a consequence of the enhanced carrier diffusivity at high injection levels [103]: the diffusion may bring the carriers from the photoexcited CVD layer into the heavily doped substrate where they recombine by Auger mechanism and provide values as short as ~1 ns. We also note that VLS growth of 3C-SiC seed layer on highly

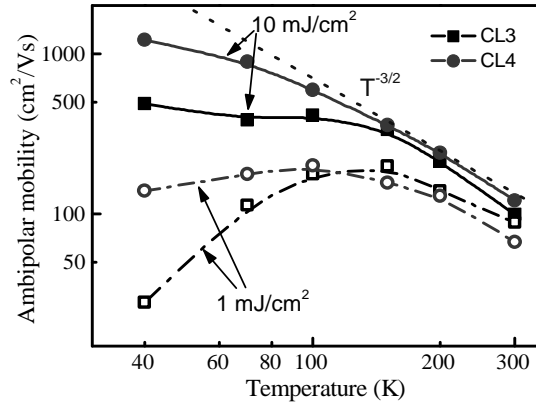


Fig. 6.3.3 Ambipolar carrier mobility of CL3 and CL4 layers as a function of temperature at 1 and 10 mJ/cm² excitation energy densities.

doped 6H-SiC substrates usually results in a highly N-doped layer which, in turn, may also contribute to fast carrier recombination.

The temperature dependence of D_a and bipolar mobility $\mu_a = eD_a/kT$ revealed the different carrier scattering features in CL3 and CL4 layers (Fig. 6.3.3), especially in $T < 150$ K range. The significantly lower μ_a value in A3 at 40÷60 K pointed out to presence of efficient scattering centers. These centers can be related to high density of ionized impurities or charged defect clusters. When excitation increases μ_a increases one order of magnitude as Fig. 6.3.3 shows. This is a consequence of screening of charged impurities by induced high excess carrier concentration. At $T > 150$ K μ_a decreases with temperature as $\propto T^{-3/2}$ due to carrier screening on acoustic phonons. In general, the μ_a values in sample CL3 are lower than these of CL4 in the same excitations. Since LTPL measurements have determined a higher N concentration in CL4 than in sample CL3 we can deduce that, most probable, ionized impurities and structural defects that contribute to the carriers scattering exhibit higher concentrations in sample CL3 than in CL4.

Samples CN1, CN2, CN3

By measuring the fast DT decay, the non-equilibrium carrier lifetime was determined versus excitation and temperature. At room temperature, the carrier lifetime increased with excess carrier density in each sample. The highest

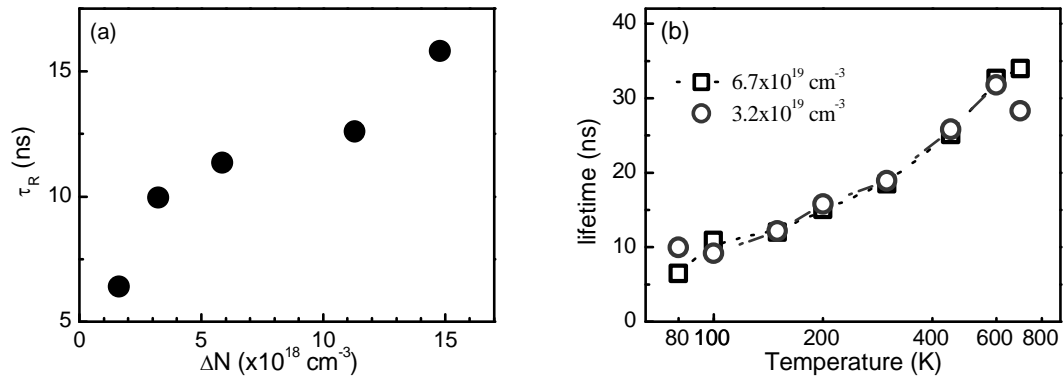


Fig. 6.3.4 a) Fast components of carrier lifetime dependence on excess carrier density at room temperature, measured using ps pump and delayed ps probe laser pulses. b) Temperature dependence of carrier lifetime determined from long decay tails of DT. Measurements were performed on sample CN1.

lifetime values were found in sample CN1 (Fig. 6.3.4(a)), while the lowest ones of 7 ns were obtained for sample CN2 (not shown). A monotonous increase of lifetime with temperature was observed also in 80-700 K temperature range for sample CN1 (Fig. 6.3.4(b)).

Since in the case of sample CN2 the carrier lifetime was rather short, only samples, CN1 and CN3, were studied by LITG technique. The carrier diffusion coefficient was slightly higher in the sample CN1 than in sample CN3, as it is shown in Fig. 6.3.5(a). The temperature dependence of the ambipolar mobility, $\mu_a = eD_a/kT$ is shown in Fig. 6.3.5(b) at the excess carrier density of about $7 \times 10^{17} \text{ cm}^{-3}$. In 150-700 K range, the ambipolar mobility decreases with temperature. This decrease can be described by a power $\mu_a \propto T^\gamma$ dependence, where an index γ value varies between -1.6 and -1.8, depending on the sample. This behavior in the 200-700 K temperature range is the consequence of carrier scattering by acoustic phonons which provides a typical $\gamma = -3/2$ value. Thus the additional scattering on extended defects can be assumed as insignificant. At 300 K, the ambipolar mobility values were found to be $115 \text{ cm}^2/\text{Vs}$ (sample CN1) and $95 \text{ cm}^2/\text{Vs}$ (sample CN3). Below 150 K, the scattering on ionized impurities started to contribute and led to nearly constant μ_a value on sample B3, while on sample CN1 a slight increase was still observable. The small enhancement of the ambipolar mobility in the range of $T < 150 \text{ K}$ shows

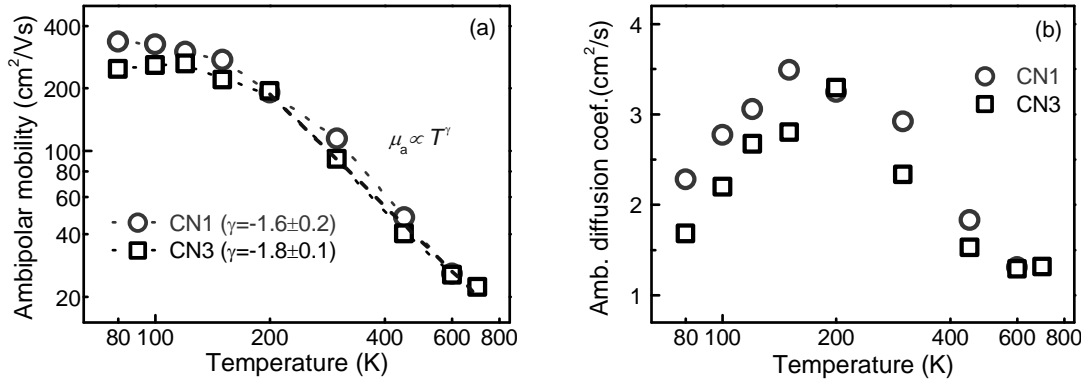


Fig. 6.3.5 Temperature dependence of a) carrier diffusion coefficient and b) carrier ambipolar mobility at $\Delta N = 7 \times 10^{17} \text{ cm}^{-3}$ carrier injections value, on the samples CN1 (○) and CN3 (□).

reduced scattering by points and extended defects on sample CN1, compared to sample CN3. By increasing the excess carrier density to $1.8 \times 10^{18} \text{ cm}^{-3}$, the overall tendency remained the same. However, the carrier-density dependent decrease of mobility, observed in 80-150 K range, is due to effect of band gap renormalization, which has been previously detected on high quality 3C-SiC layers [130].

The diffusion coefficient was higher on sample CN1 than on sample CN3 as it is shown in Fig. 6.3.5(b). Since the obtained results from optical measurements suggested that sample CN1 has the best quality among all the samples studied here, this sample was characterized by reciprocal space mapping of XRD. The results allowed determining a stacking fault (SF) density of $\sim 1.3 \times 10^4 \text{ cm}^{-1}$. This rather moderate value is coherent with TEM measurements performed on similar 3C samples [88]. Interestingly, no twinning of the 3C material was detected.

The comparison with our previously reported results, obtained from transient grating technique on 3C-SiC [146], suggests that the recorded values of carrier lifetime and ambipolar mobility are higher. This can be attributed to better growth conditions of the CVD layer, and more specifically to the higher growth temperature. On the other hand, lifetime increase with carrier injection level (Fig. 6.3.4(a)) indicates gradual saturation of carrier trapping centers, and this feature is typical for thin 3C-SiC layers [146]. In general case, carrier

lifetime is expected to decrease at carrier densities above 10^{19} cm^{-3} due to impact of nonlinear recombination. For example, lifetime decrease from 50 ns to ~ 6 ns was measured at $\Delta N = 10^{19} \text{ cm}^{-3}$ in 200 μm thick epitaxial 3C-SiC layers due to Auger recombination [147]. Consequently, the impact of trap saturation is the dominant nonlinear recombination mechanism in the measured $\tau_R(\Delta N)$ dependence (carrier injection range of $\Delta N = 3\text{-}30 \times 10^{18} \text{ cm}^{-3}$) at the given thin layer (sample CN1). At slightly higher carrier injection level ($\Delta N = 3.2\text{-}6.7 \times 10^{19} \text{ cm}^{-3}$) the impacts of these two phenomena are comparable (Fig. 6.3.4(b)).

It is worth to mention that gradual increase of lifetime in 150-700 K range (Fig. 6.3.4(b)) and its correlation with $D_a(T)$ was recently observed in 3C epitaxial layers grown either on on-axis 4H or on undulant Si substrates [147]. Moreover, the observed $D_a(T)$ and $\tau_R(T)$ correlation indicates a relationship between the recombination and the diffusion processes (in Fig. 6.3.2(b) and Fig. 6.3.5(b)) due to carrier surface recombination. This tendency was confirmed now on the studied $\sim 10 \mu\text{m}$ thick layer (sample CN1), when the impact of surface recombination is higher.

As a feedback to the growth conditions, the carrier parameters determined in this work show clearly that the best 3C-SiC material quality is obtained at the highest CVD growth temperature. This confirms the trend already seen by TEM study on other samples where lower crystalline defect density was found at higher CVD growth temperature [88].

Lifetime vs. CVD layer thickness

In the following, we attempt to reveal the relation of surface and bulk recombination mechanisms as the thickness of a CVD increases. In the beginning we correlate thin ($\sim 10 \mu\text{m}$) CVD layers grown on VLS layer presented in the previous paragraphs and later we extend this correlation to other CVD layers grown on other substrates. In the first case we have use the CL2, CL3 and CN3 samples of Table 6.3.1. In the second case we include samples have been grown by HOYA company.

The effective free carrier lifetime, obtained at moderate excitation energy densities in order to avoid non-linear recombination mechanisms, shows strong dependence on layer thickness. In Fig. 6.3.6(a) it is plotted the effective free carrier lifetime as a function of CVD layer thickness. As one can notice, lifetime exhibits a linear dependence on CVD layer thickness. The fitting by a linear function results in a proportionality factor of (1.9 ± 0.1) at $5\div 11\ \mu\text{m}$ range of CVD layer thickness. This means that within the initial few micrometers of a CVD layer there is a linear increase of effective free carrier lifetime as $\tau_R \propto (1.9\pm 0.1) \times d_{\text{CVD}}$. Since at layers with low effective free carrier lifetime the surface recombination has a limited contribution, we assume that the non-radiative recombination through the deep defect states in the band gap (SRH) is the dominant recombination mechanism. It is reported that these deep level energy states in the band gap are related to carbon vacancies (V_C) [115, 148]. Thus, we can conclude that the recombination centers, closely related to carbon vacancies (V_C), reduce their concentration with the layer thickness by a factor of 1.9 ± 0.1 .

A more extended correlation of effective lifetime with CVD layer thickness on different substrates from our studies and literature [88, 102, 147] is presented in Fig. 6.3.6(b). In this log-log diagram, the effective lifetimes are plotted as a function of their CVD layer thicknesses. Lifetime values have been extracted by fitting by a single exponential decay function on experimental DT decays. All DT kinetics were obtained at moderate excitation intensities ($\sim 5 \times 10^{17}\ \text{cm}^{-3}$) in order to eliminate the contribution of non-linear recombination mechanisms in the overall effective free carrier lifetime. The initial fast increase of lifetime progressively saturates to values of approximately 100 ns for very thick layers $> 200\ \mu\text{m}$ (see Fig. 6.3.6(b)).

Surface recombination velocity possesses an important role in layers with long lifetimes, and hence low concentration of recombination centers in bulk [88, 148], since carriers are able to reach surfaces where they recombine. Since the excitation/penetration depth is approximately $5\ \mu\text{m}$, carriers in a layer with low recombination rate are able to diffuse up to surface where they recombine.

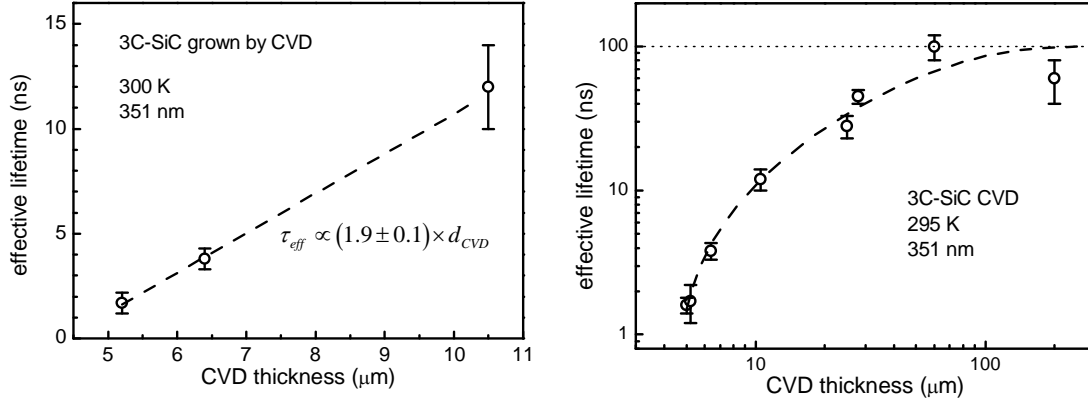


Fig. 6.3.6 a) Lifetime dependence of CVD homoepitaxial layers on VLS seed layers. b) Lifetime vs CVD thickness for 3C-SiC layers grown on different substrates.

As the total effective carrier lifetime (τ_{eff}) in a layer is determined from its bulk and surface lifetime, τ_R and τ_S , respectively as:

$$\frac{1}{\tau_{eff}} = \frac{1}{\tau_R} + \frac{1}{\tau_S} \quad (5.5)$$

we can deduce that recombination at the surface is the determinative recombination term for the overall effective lifetime at the vicinal to surface volume as the CVD layer thickness increases above 100 μm.

6.3.4 Conclusions

Carrier lifetime in thin (up to ~10 μm) 3C-SiC layers grown on seeded 6H-SiC increases linearly with the layer thickness, indicating the reduction of recombination center density as layer thickness and growth temperature increase. Further increase of CVD layer thickness (>100 μm) results in saturation of carrier lifetime due to domination of surface recombination process.

6.4 Electronic properties of bulk 3C-SiC grown by sublimation techniques

6.4.1 Introduction

In this subsection we investigate with optical time-resolved pump-probe techniques the carrier dynamics of bulk 3C-SiC grown by continuous feed physical vapor transport (CF-PVT) and sandwich SE technique on bare and seeded 6H-SiC substrate. Our aim is to attempt to find out the influence of VLS seed layer to electronic properties of overgrown bulk 3C-SiC as well as the exciton signature in carrier recombination and transport processes. For this reason we have studied four different samples been grown on 6H-SiC, 3C-SiC (2) and graphite with different growth configuration setups.

6.4.2 Samples and techniques

The CF-VPT growth method, as a modified sublimation technique, is possible to apply for the growth of bulk 3C-SiC crystals both in seeded and spontaneous configurations. In our studies, one sample of each CF-VPT configuration was available. The CF-PVT process combines high temperature chemical vapor deposition (CVD) for the in situ formation of the polycrystalline SiC source and physical vapor transport for the single crystal growth. The crucible is divided in two regions (CVD region and sublimation region) by porous graphite foam. The porous foam acts as a support for CVD SiC deposition and thus as a source for the sublimation step. The high purity polycrystalline SiC source was fabricated from tetramethylsilane.

The first sample (B4 (BOU435)) was an 800 μm thick bulk 3C-SiC crystal grown homopolytically on 3C-SiC (111) seeded 6H-SiC (0001) substrate. The growth of the 3C-SiC sample was performed in the CF-PVT reactor described in details in Ref. [67]. The seed consists of a (111) oriented 3C-SiC thin layer deposited on a Si-face (0001) 6H-SiC substrate by the VLS method in a Si-Ge melt [119]. The nucleation step of the CF-PVT layer was carried out under a silicon-rich gas phase by placing 0.334 g silicon piece inside the porous foam. This amount was chosen as an intermediate value

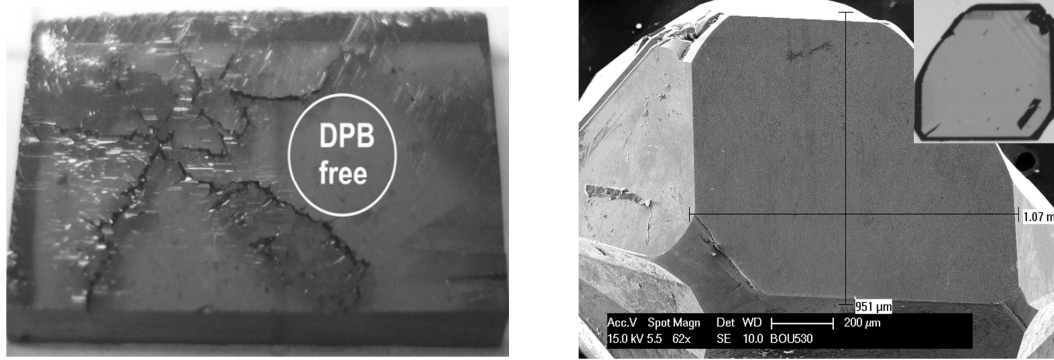


Fig. 6.4.1 a) As-grown 3C-SiC (sample B4) with some large domains free of DPB. The size of the sample is $5 \times 9 \text{ mm}^2$. b) 3C-SiC crystal on graphite and the $100 \mu\text{m}$ thick slab (sample B5) with (100) face orientation after subtraction by etching (inset).

between the formation of silicon droplets at the seed surface and a lack of silicon which could lead to graphitization. By melting during the heating step, Si "impregnates" the graphite foam to form a Si-rich SiC source. For this experiment, the growth temperature was $1980 \text{ }^\circ\text{C}$ and the pressure 1.4 torr . Under such conditions, a 3C-SiC wafer with large DPBs-free domains has been obtained (Fig. 6.4.1(a)). For this kind of sample, DPB free domains only exhibit micro-twins lamellae and stacking faults. Already, the low temperature photoluminescence (LTPL) spectra collected at 5 K in the DPB-free crystal present an excellent resolution of near band edge (NBE) excitonic features, with multiple bound exciton complexes (MBEC) resolution up to $m=5$. This appears only on high quality 3C-SiC material. Moreover, the nitrogen impurities concentration was determined to be $(1-5) \times 10^{16} \text{ cm}^{-3}$. A more detailed structural investigation on such a sample is given in Ref [149].

In the case of sample B4 we have applied a picosecond transient grating technique to investigate carrier dynamics in the given 3C-SiC wafer. Large thickness of the crystal allowed investigation of nonequilibrium carrier dynamics at surface and bulk excitation conditions. We used for excitation a 10 ps duration pulses at 351 nm or 527 nm wavelength with quantum energies of 3.53 eV or 2.35 eV , i.e. above the band gap of the 3C-SiC (2.36 eV at 300 K) or at the band gap. Correspondingly, the free carriers were photoexcited either in a thin surface layer of about $\alpha^{-1}=4.5 \mu\text{m}$ or in a thick layer of $\alpha^{-1}=300\text{--}500$

μm . In the latter case, the 6H-SiC substrate was not excited, as its band gap (3.0 eV) is larger than the used quantum energy at 527 nm. The free carrier grating decay was monitored by a delayed probe beam at 1053 nm. The studies were performed in a wide range of excitation energy density I and temperature $T=10\text{--}300$ K.

The second sample (B5 (BOU530)) was a 100 μm thick bulk 3C-SiC crystal grown by CF-PVT spontaneous nucleation on graphite we applied a picosecond DT and LITG technique. Spontaneously nucleated 3C-SiC crystals were grown by the CF-PVT technique [150, 151] using TMS (Tetra-Methyl-Silane) as precursor for the in-situ formation of the polycrystalline SiC source. The growth temperature was 2070 $^{\circ}\text{C}$ and the reactor pressure approximately 1 torr. Up to now, and independent of the purity of TMS, CF-PVT always resulted in very high purity material [131, 152]. The unintentional doping level of nitrogen (N) in the sample was determined by the use of LO mode of room temperature Raman spectrum. According to Yugami [153] calibration curve and fitting of LO at 972 cm^{-1} we derived carrier concentration around $1.1 \times 10^{17}\text{ cm}^{-3}$. In Fig. 6.4.1(b) pictures obtained by optical microscope of as grown 3C-SiC crystal on graphite and the 100 μm thick slab with (100) face orientation after subtraction by etching (inset).

Fast and slow kinetics in a wide temperature and excitation range have been obtained for sample B5 by optical and electrical delayed DT technique. In all measurements, nonequilibrium carriers were injected by an above-bandgap optical pulse of a Nd:YLF pulsed laser with 10ps pulse duration. Through the free carrier absorption (FCA) or free carrier grating diffraction (FCD) of a below-bandgap optical pulse, the excess carriers reduce the transmission or diffraction efficiency of the probe beam. The resulted transmission and diffraction transients reflected the concentration of the decaying nonequilibrium carriers, and thus the carrier lifetime and diffusivity [78, 86].

The rest two samples have been grown by sandwich SE technique on repolished and on VLS (111) 3C-SiC seeded (0001) 6H-SiC, respectively. The first one (FS50 (SE-050) (Fig. 6.4.2(a)) was grown on repolished (0001) 6H-

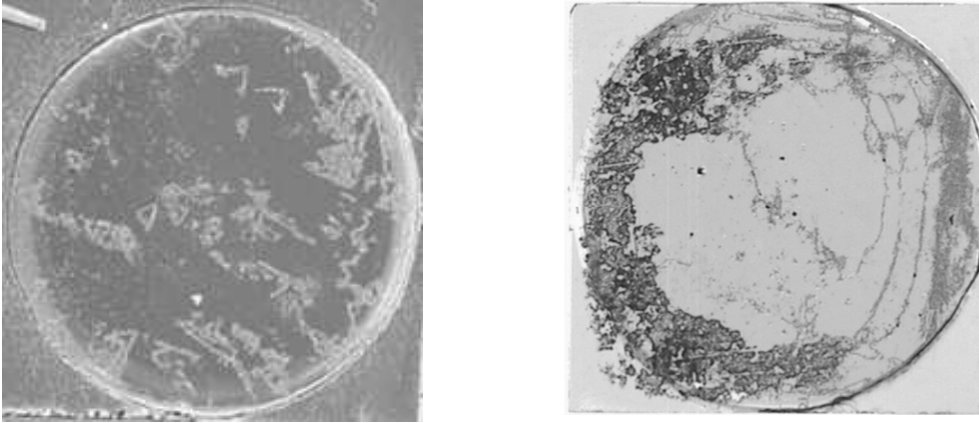


Fig. 6.4.2 Pictures of as-grown samples a) FS50 and b) FS24. Their diameter is ~10mm.

SiC substrate at 1775 °C. Its thickness was 200 μm and its nitrogen and aluminum concentration have been determined by LTPL was $[\text{N}] \sim 10^{16}$ and $[\text{Al}] \sim 10^{15} \text{ cm}^{-3}$, respectively. The second one (FS24 (SiSn-24)) was grown on (111) 3C-SiC VLS seed layer on (0001) 6H-SiC substrate at 1775 °C (Fig. 6.4.2(b)). Its thickness was 170 μm and its nitrogen and aluminum concentration have been determined by LTPL was $[\text{N}] \sim 2.4 \times 10^{16}$ and $[\text{Al}] \sim 4.5 \times 10^{15} \text{ cm}^{-3}$, respectively. In Fig. 6.4.2 one can see that there is not uniform distribution of structural defects on the surface for both samples. Our measurements have been taken at the less defective areas in order to reduce the laser beam spreading.

These two samples (FS50, FS24) have measured by LITG at 80-800 K temperature range. The excitation was the 351 nm wavelength of $\text{Nd}^{+3}:\text{YLF}$ with 10 ps pulse duration. The excitation energy density was 0.2 mJ/cm^2 .

6.4.3 Results and discussion

Samples B4 and B5 (CF-PVT)

Decay of the free carrier grating was monitored at various excitation energies providing ambipolar plasma density in range from $\sim 10^{17} \text{ cm}^{-3}$ up to $\sim 10^{20} \text{ cm}^{-3}$. From the measured grating decay kinetics at various periods Λ we determined the ambipolar diffusion coefficient D_a and carrier lifetime τ_R values. These

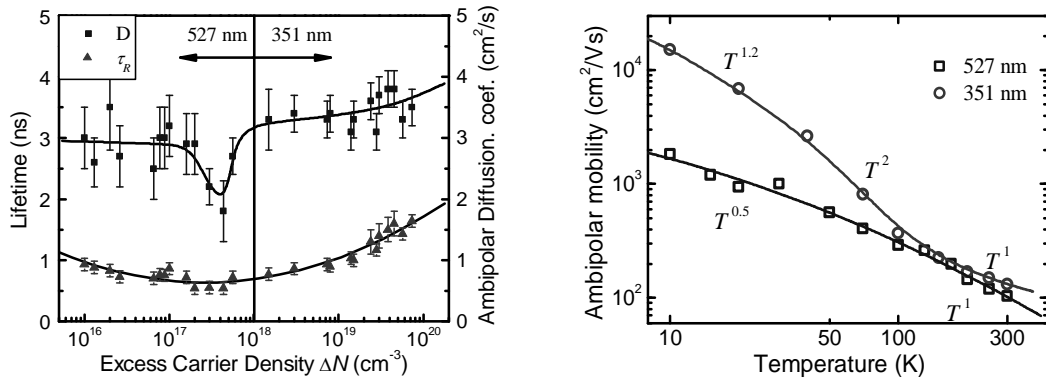


Fig. 6.4.3 a) Dependencies of the bipolar diffusion coefficient D and carrier lifetime τ_R on excess carrier concentration in B4. b) Temperature dependence of ambipolar carrier mobility at bulk (squares) and surface (circles) excitation conditions with excess carrier density of 5×10^{16} and 1×10^{18} cm⁻³, respectively.

parameters for varying excitation energy and wavelengths pointed out being dependent on photo-excited carrier density (Fig. 6.4.3(a)). The tendency of diffusion coefficient at lower carrier density (for $N < 10^{18}$ cm⁻³) is to decrease with the subsequent gradual increase of at higher excitations (for $N > 10^{18}$ cm⁻³). We attributed the small decrease of D_a value to nonequilibrium carrier transport through the spatially modulated carrier plasma at conditions of band gap renormalization, and the subsequent increase of the D_a value to the decreasing carrier scattering probability in the high density plasma, when its concentration approaches a threshold of degeneracy (Mott transition concentration). This feature was observed earlier for undoped, high structural quality 4H-SiC [154, 155] but not for an epitaxial VLS/CVD-grown 3C-SiC layer [102]. In the latter case, low temperature PL measurements in this 3C layer revealed a high density of nitrogen ($\sim 5 \times 10^{18}$ cm⁻³ [140]) which strongly contributed to the carrier scattering and masked the density-dependent effect on mobility. The 2-fold increase of carrier lifetime with excitation (Fig. 6.4.3(a)) at high carrier density was observed earlier in the VLS-grown 3C epitaxial layer [102] and might be caused by a saturation of carrier trapping centers. On the other hand, simultaneous increase of D_a and τ_R values pointed out to decreasing rate of carrier recombination in degenerate plasma.

The temperature dependence of ambipolar mobility $\mu_a = eD_a/kT$ (Fig. 6.4.3(b)) indicated high values of mobility below RT (e.g. 370 cm²/Vs and 300 cm²/Vs at 100 K at higher and lower carrier density, respectively) which exceed the previously reported ones for epitaxial 3C-SiC (e.g. the μ_a value peaked up to 250 cm²/Vs at 100 K) [102]. In 100-300 K range, the dependence $\mu \propto T^{-k}$ revealed the expected phonon and extended defect contribution to carrier scattering with $k \approx 1$ for surface and bulk excitation. In the range $T < 100$ K, where only the scattering by point and extended defects is expected with quite low k value ($k \leq 0$), we observed the unusual high k value ($k > 1$ at higher carrier density and $k = 0.5$ at lower carrier density). This behavior for higher carrier density (determined at 351 nm excitation) is probably caused by essential increase of carrier diffusion coefficient in highly degenerate plasma, especially at low T . The latter peculiarity indicated the dominant contribution of carrier-density dependent but not structural defect-density governed scattering mechanisms. The similar dependence of μ_a vs. T was determined at 527 nm excitation, i.e. for grating in a bulk with lower carrier density. As this kind peculiarity was not earlier observed in highly-excited 3C-SiC epilayers, we conclude that the given bulk crystal has quite high structural quality. Indeed, the NBE excitonic features in LTPL spectra as well as structural characterization also indicated the high crystalline quality of CF-PVT-grown bulk cubic SiC [149]. To conclude, these data indicated dominant contribution of the carrier-density dependent but not structural defect-density governed scattering mechanisms. This tendency, in general, points out to low electrical activity (or low density) of extended structural defects.

LITG and DT measurements in 10-300 K temperature range and at different excitations have been done on sample B5. As it is presented in Fig. 6.4.4 free carrier lifetime exhibits values of ~ 2 ns in whole temperature range (10-320 K) with no excitation dependence for temperatures higher than 50 K. The rapid lifetime increase, as excitation intensity decreases below the 0.5 mJ/cm² in temperature range below 50 K will be discussed later. The free carrier lifetime of this crystal is two times higher than of homoepitaxial one

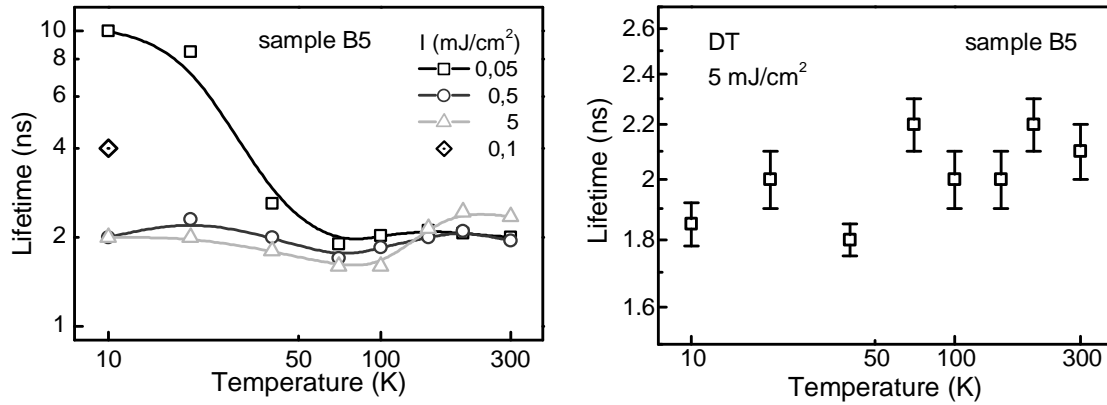


Fig. 6.4.4 Temperature dependence of lifetime of sample B5 obtained by a) LITG at different excitations, and, b) DT technique.

(sample B4) grown by the same technique on VLS seed layer in the same excitation range (see Fig. 6.4.3(a)). This is an indication of lower concentration of recombination centers; both isolated intrinsic point defects, usually carbon vacancies, and aggregated point defects on extended structural defects.

In Fig. 6.4.4(a) we can notice an increase of lifetime with the reduction of excitation as the temperatures decreases below 50 K. Similar behavior has shown sample A. We can attribute this to the thermal ionization of nitrogen bound excitons (NBE) to free exciton when the excited free carrier density is similar to carrier traps concentration strongly related to nitrogen impurities. Unfortunately, our setup detection limit and sample limitations prevent us from further reduce of excitation energy density in order to verify the lifetime value of NBE in 3C-SiC (160 ns) reported in [156].

Ambipolar carrier mobility as a function of temperature in the 10-320 K range is plotted in Fig. 6.4.5(a). Its values at temperatures above 100K are slightly higher than those of CF-PVT on VLS sample in Fig. 6.3.3(b), but not higher for temperatures below 100 K. Below that temperature (100 K) we can notice the effect of excitation energy density on the ambipolar carrier mobility, or in other words, to induced excess carrier density. In low enough excitations the free carrier mobility almost vanishes due to scattering of moving carriers on ionized impurities into the semiconductor lattice structure. As excitation progressively increases, the photoexcited excess carriers increases the

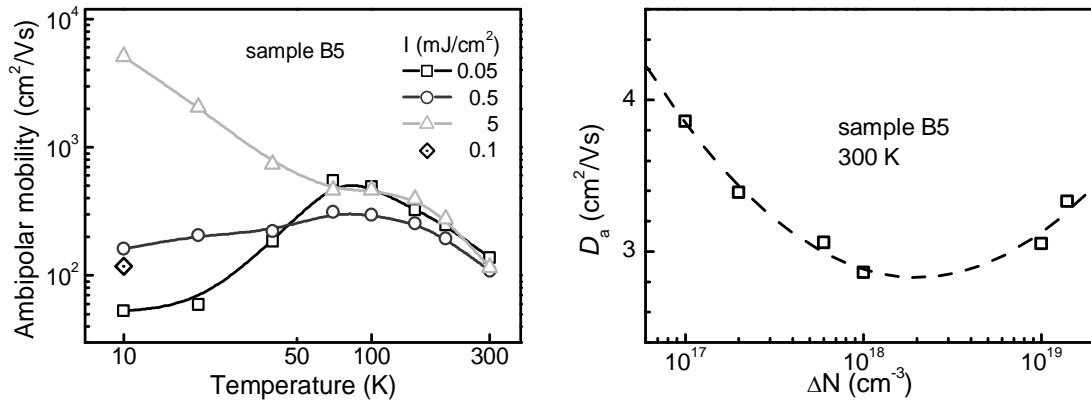


Fig. 6.4.5 a) Temperature dependence of ambipolar mobility of sample B5 at different excitations. b) RT ambipolar mobility as a function of excess carrier density.

screening of ionized impurities and hence their scattering efficiency diminishes.

In Fig. 6.4.5(b) is plotted the ambipolar diffusion coefficient (D_a) as a function of excess carrier density (ΔN). As far the ΔN is below the Mott density its increment results in reduction of D_a . As in the case of sample B4, we attributed this small decrease of D_a to nonequilibrium carrier transport through the spatially modulated carrier plasma at conditions of band gap renormalization. When ΔN is above Mott density the probability of carrier scattering is decreased with subsequent increase of the D_a value. Theoretical studies [157] based in many-body effects on other semiconductors have shown the same excess carrier dependence of ambipolar diffusion coefficient as our experimental results does. It is also proposed [158] that, as the excess carrier

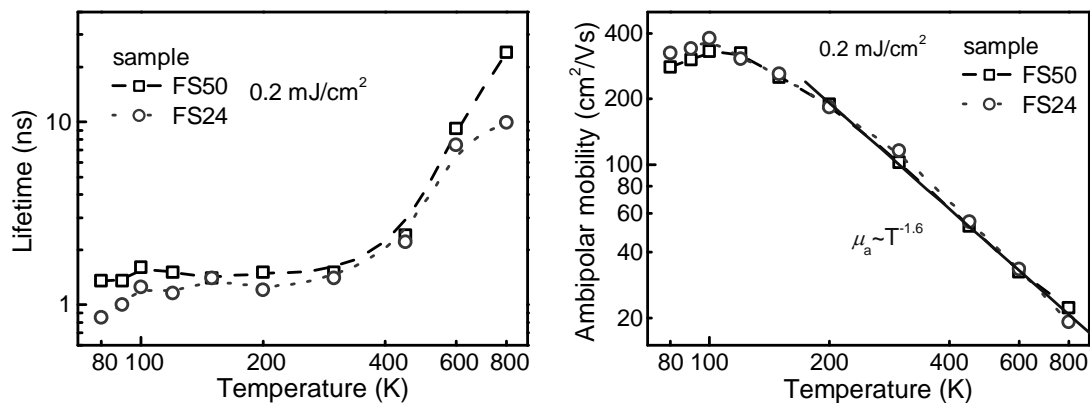


Fig. 6.4.6 Temperature dependence of a) free carrier lifetime, and b) ambipolar carrier mobility of samples FS50 and FS24 at 0.2 mJ/cm² excitation energy density.

density increases above critical Mott density the exciton density increases, and now there is a shift in the method of conduction: excitons start to participate to carrier diffusion but not to charge diffusion since excitons are neutral. In principle, one can imagine a situation with $D_{ex} > D_a$ because neutral excitons may not be scattered by charged impurities. This is in contrast to the reduction in effective ambipolar diffusion constant that results when rigid band gap narrowing is assumed.

Samples FS50 and FS24 (SE)

In Fig. 6.4.6 that follows it is presented the temperature dependence of free carrier lifetime and ambipolar mobility at moderate excitation intensity 0.2 mJ/cm^2 . Both free carrier lifetime and ambipolar mobility in both samples exhibit similar values.

Free carrier lifetime is $\sim 1.6 \text{ ns}$ at room temperature while for higher temperatures shows a steep increase with slightly different values for at these two samples. This increment at temperatures higher than the room temperature with respect to decrease of ambipolar mobility due to scattering on deformation acoustic phonons ($\mu_a \propto T^{-3/2}$) indicates that the carrier lifetime is diffusion limited. Even carrier lifetime exhibits values typical for bulk layers grown by SE technique the ambipolar mobility reaches high enough values of $\sim 120 \text{ cm}^2/\text{Vs}$ at RT. At lower temperatures ($< 150 \text{ K}$) the effect of carrier scattering on ionized impurities is obvious since the excess carrier density ($\sim 6 \times 10^{17} \text{ cm}^{-3}$) is not high enough to screen ionized impurities.

As a result, we may claim that the existence of VLS seed layer as far as it concerns the carrier lifetime and ambipolar mobility close to the surface of these two bulk layers have no detectable effect.

6.4.4 Conclusions

Spontaneous nucleation of 3C-SiC on graphite by CF-PVT technique results in a crystal with twice longer carrier lifetime compared to those nucleated on 6H-SiC substrates by CF-PVT or SE techniques, no matter seeded or not, while

ambipolar mobility is the same for all of them. Moreover, the thin 3C-SiC seed layer on 6H-SiC substrate seems to have no significant effect on electronic properties of the overgrown by SE bulk 3C-SiC.

6.5 Comparison of the electronic properties in variously grown 3C-SiC

In this last part we consider the obtained carrier lifetime and ambipolar mobility with respect of their impurities concentration, layer thicknesses and growth temperatures from all layers presented in chapters 5 and 6, at room temperature, and at moderate high excitations in the vicinal to surface area, where non-linear effects have not any significant contribution.

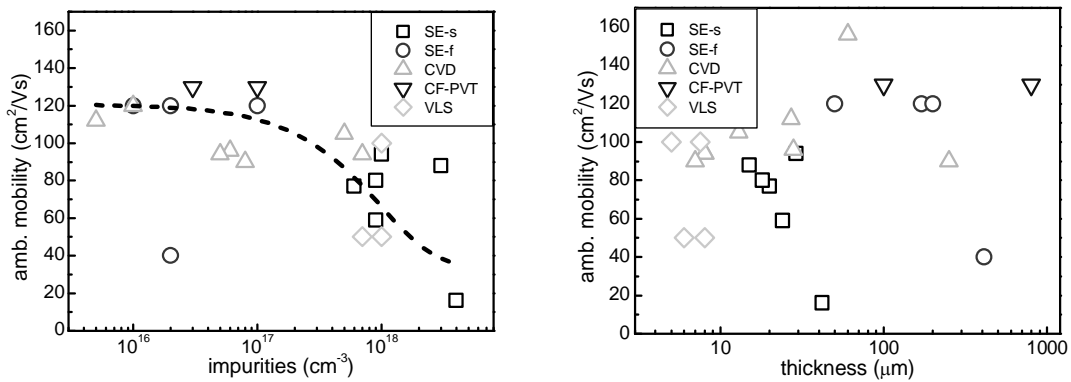


Fig. 6.5.1 Ambipolar carrier mobility as a function of a) impurities concentration, and b) layer thicknesses for 3C-SiC layers at RT and moderate high excitation levels.

Ambipolar mobility values as a function of their impurities concentration are depicted in Fig. 6.5.1(a). As the dashed line indicates, ambipolar mobility decreases as impurity concentration increases. This specific tendency is described previously for Si [159] and SiC polytypes [160] as a consequence of carriers scattering on ionized impurities. Moreover, ambipolar mobility shows a tendency to increase slightly as layer thickness increases most probably due to reduction of scattering processes related to structural imperfection.

On the other hand, and independently from growth technique, carrier lifetime seems that has not any specific dependence on layer doping or thickness, as in Fig. 6.5.2 is depicted. This means that the growth conditions, at

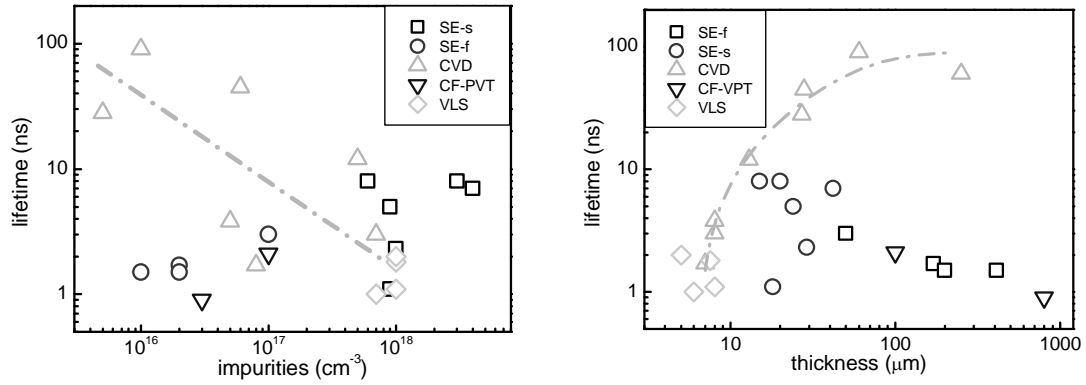


Fig. 6.5.2 Effective lifetime as a function of a) impurities concentration, and b) layer thicknesses for 3C-SiC layers at RT and moderate high excitation levels.

each separate technique, are those that can potentially determine lifetime in 3C-SiC layers. In these two diagrams we can noticed that only 3C-SiC layers grown by CVD technique exhibit a clear dependence on impurities concentration and layer thickness. Thus, suitable optimization of growth parameters may control carrier lifetime. For example, it seems that growth temperature slightly lower than 1600 °C result in layers with high carrier lifetimes, as well as ambipolar mobility (see Fig. 6.5.3).

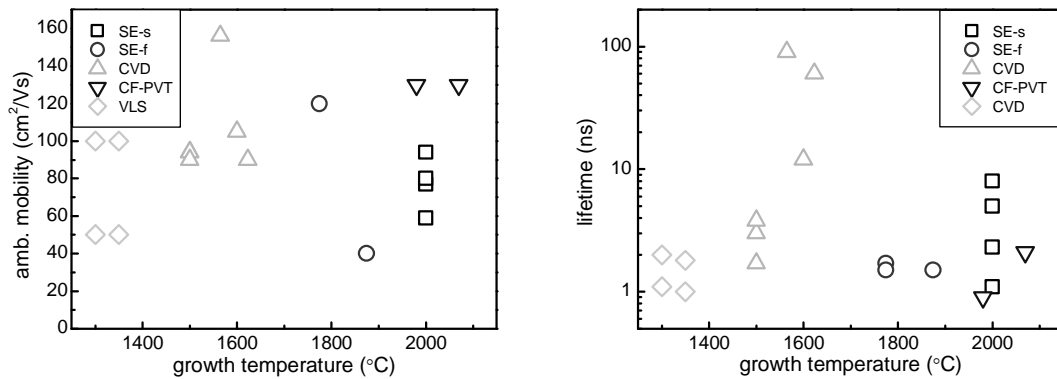


Fig. 6.5.3 Ambipolar mobility (a) and lifetime (b) of 3C-SiC layers grown by several different techniques as a function of growth temperature.

On the other hand, if low values of lifetime are required for high frequency applications, but with high ambipolar mobilities, CF-PVT growth technique is the most promising one.

Chapter 7 The influence of substrate surface morphology on 3C-SiC electronic properties

This chapter deals with the influence of substrate on the lifetime and diffusivity of carriers in 3C-SiC epilayers grown by different techniques and it is divided into two subchapters. The first one deals with anisotropy of ambipolar carrier diffusivity in CVD layers and the second one with the carrier lifetime dependence on substrate roughness in SE layers.

7.1 Defect induced anisotropy in diffusivity of homoepitaxial 3C-SiC

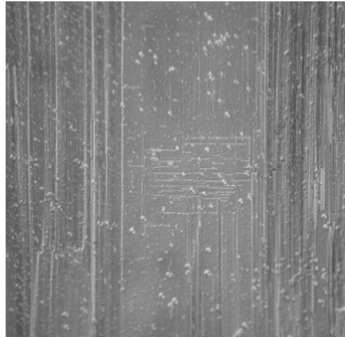

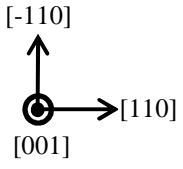
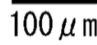
7.1.1 Introduction

The ability of the same compound to exist in more than one crystalline form is referred as polymorphism, while, the one dimensional polymorphism, i.e. when crystalline forms have the same atomic plane in common and differ only in their stacking sequence along the direction normal to plane, is called polytypism. As stacking fault (SF), a fundamental planar defect, has low formation energy in SiC, various kinds of SFs may easily occur as a result of changing the stacking sequences with respect to the matrix [52] resulting in more than 200 known polytypes in SiC. However, the effects of SFs on carrier dynamics in SiC have not been investigated extensively up to now, especially in the case that 3C-SiC is the host matrix. In this subchapter we discuss the effects on carrier transport and recombination properties due to oriented formation of grooves on homoepitaxially grown 3C-SiC by CVD technique.

7.1.2 Samples and experimental techniques

The samples under investigation are two 3C-SiC homoepitaxial layers grown by chemical vapor deposition (CVD) on highly doped (100) 3C-SiC commercial substrates produced by HOYA corp. [161]. Their thicknesses, nominal concentrations of nitrogen impurity, density of surface grooves and

Table 7.1.1 Sample information on groove and pit density as well as on N concentration. Diffusion coefficients, as well as, rough estimation of SRH recombination time are presented.

Sample	HG1	HG2
Surface photographs after etching at 400°C for 2 min obtained by optical microscope ([161])		
		
		
Thickness (μm)	23-30	28
[N] (cm^{-3})	4×10^{15}	6×10^{16}
Grooves (cm^{-2})	1.6×10^5	1.5×10^6
Pits (cm^{-2})	2.4×10^5	8.2×10^5
Leakage current (A/cm^2)	$\sim 10^{-4}$	$> 10^{-3}$
D_a (Normal) (cm^2/s)	2.2	1.6
D_a (Parallel) (cm^2/s)	3.3	2.5

pits, as well as leakage current density are enlisted in Table 7.1.1. Both samples have been etched with KOH at 400°C for 2 minutes in order to show up their structural defects as pictures in Table 7.1.1 present. The etched surface for both the samples show circular pits and parallel grooves. In sample HG1 some grooves align in the horizontal direction and the rest of grooves are in the vertical direction while in sample HG2 all grooves align in the horizontal direction. These grooves most probably originate from stacking faults aligned in [110] and [-110] directions [162]. As it is clear, sample HG2 shows higher values of all parameters mentioned above than those in sample HG1.

We apply picosecond LITG and DT technique to investigate carrier dynamics in the given two 3C-SiC layers. Since the absorption depth in 3C-

SiC is $\sim 5 \mu\text{m}$ for 351nm wavelength, it is ensured that only the epilayer and not the substrate is excited.

7.1.3 Results and discussion

Ambipolar carrier diffusivity and effective lifetime for 1 and 10 mJ/cm^2 (or 3.5×10^{18} and $35 \times 10^{18} \text{ cm}^{-3}$ excess carrier density) are extracted as is illustrated in Fig. 7.1.1(a). In Fig. 7.1.1(b) it is depicted the ambipolar carrier diffusion coefficient (D_a) for both layers for two mutually perpendicular directions, when the transient grating vector is normal (further denoted as N) or parallel (P) to the groove alignment. Note that the ambipolar carrier diffusion direction coincides with the transient grating vector direction. Summarizing the obtained results in Fig. 7.1.1(b) it is clear that in the case of P-geometry the D_a is substantially higher than in the case of N-geometry for both samples within the entire excitation range. We attribute this to the potential barriers that stacking faults introduce to energetic band structure. Carriers that diffuse parallel to the grooves experience less scattering than those diffusing across the potential barriers. The potential barrier creation might originate from SF local structure within crystal lattice, which can be considered as a quantum barrier [50]. In a similar case in GaN the anisotropic conductivity is explained by carrier scatterings by basal SFs [163]. From the obtained values in N- and P-geometry

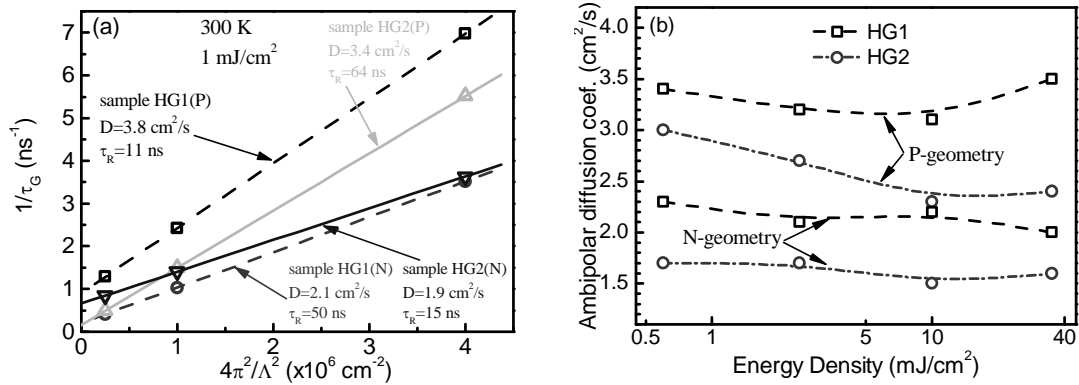


Fig. 7.1.1 a) Determination of values of ambipolar diffusion coefficient D_a and effective recombination lifetime $\tau_{R,eff}$. b) Excitation dependence of D_a in N- and P-geometry for both layers.

for both samples we derive that the increasing grooves density, and hence SFs concentration, results in the reduction of ambipolar diffusion coefficient. Furthermore, current-voltage (I-V) measurements with Ni Schottky contacts suggest that the lower impurities concentration and SF density lead to better electrical characteristics for homoepitaxial 3C-SiC layers [161].

The results of last paragraph drive us to consider about the driving force that generates SFs during homoepitaxial growth by the same growth technique, i.e. CVD. For this reason, we investigated whether anisotropy in ambipolar carrier diffusivity is present in two free standing 3C-SiC layers grown by CVD on Si undulant surface [59]. These layers have been grown by the same technique and grower as the substrates of samples HG1 and HG2. Since in the case of free standing layers there is no predefined reference orientation on layer surface, we rotated the sample in steps starting from an arbitrary position. The obtained LITG decay times for small grating periods were used in order to monitor the possible change in D_a . The use of small grating period values for the study of D_a anisotropy is justified from two reasons. The first one is related to the principles of LITG technique. The variations of the grating period Λ leads to different contribution of the diffusion in grating decay rate, where, the smaller the grating period is, the shorter time is needed for carriers to diffuse towards grating minima and to compensate the induced modulation.

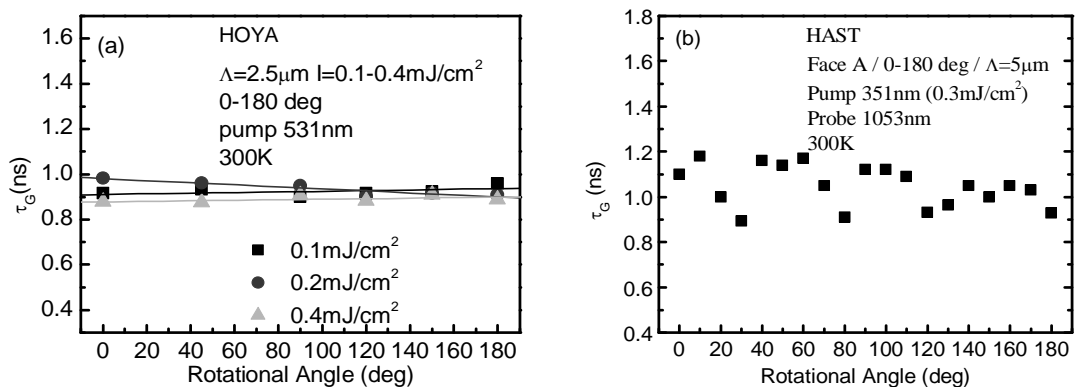


Fig. 7.1.2 Grating decay time as a function of rotation angle for a) HOYA and b) HAST free standing 3C-SiC commercial wafers at RT.

Consequently, the use of small grating period approximates the diffusion contribution on carrier dynamics minimizing the recombination contribution. The second reason is that in our study we are not interested in the absolute D_a value but rather in its relative change with the rotation angle. The results of LITG measurements for both layers reveal that there is no evidence of D_a anisotropy (Fig. 7.1.2). This means that either there is no a preferential direction for the structural defects that are responsible for the introduction of potential barriers into bands, or there is no sufficient amount of such defects capable to influence effectively the ambipolar carrier diffusivity.

In additional, DT measurements in both layers at RT have shown that carrier lifetime exhibit similar values with the substrate material. Despite the progressively increasing uncertainty, as lifetime values exceed ~ 10 ns, we have determined them to be ~ 28 and ~ 45 ns for layer HG1 and HG2, respectively. This means that the increase of grooves, pits and N impurities density – by one order of magnitude, three times and one order of magnitude, respectively – results in the apparent duplication of lifetime, or at least does not reduce it. This peculiar result contradicts to the established trend which considers that defects accelerate recombination processes. Impurities, first of all, although we believe that have minor contribution to carrier recombination processes in 3C-SiC, there is no any prove that determines its exact contribution. Pits being the surface projection of dislocations in the layer bulk are confirmed that readily contribute to trap-assisted recombination processes. SFs in 4H-SiC have shown different behavior from other – point, linear, and volume – defects, demonstrating interesting phenomena of either decreasing or increasing carrier lifetime, which depend on the SF-related energy levels [164]. In the case of 3C-SiC the – usually thin – quantum barrier in conduction band is rapidly evacuated from free carriers by their diffusion to lower potential neighboring bands. Apart from this, the Fermi energy level in the non-degeneracy regime is below the conduction band minimum of a SF, and hence, closer to equilibrium conditions. These two facts have a consequence to vast reduction of recombination processes into a SF. All the previous arguments concerning SFs

drive us to assume that SFs in 3C-SiC do not contribute to carrier recombination processes but their negligible volume percentage do not affect the overall layer recombination rate. Moreover, it is possible that the intentionally formed SFs contribute to lattice stress relaxation in the inter-SF space and hence suppress the defects density in it. A similar growth process, called epitaxial lateral overgrowth (ELO), is applied for the GaN crystal lattice optimization. In total, carrier lifetime in samples HG1 and HG2 retaining the values that have been observed to layers as their substrates reveals that the complexity of multi-parametric relation that determines the overall lifetime has to be solved by extended combination of structural and optical methods.

7.1.4 Conclusions

The ambipolar diffusion coefficient along the arrays of ordered grooves exhibits higher values than across them due to introduction of the potential barriers caused by SFs which have been formed by intentional treatment of 3C-SiC substrate. Moreover, the increasing density of grooves that results in diffusivity reduction has unspecified effect on lifetime values.

7.2 On the substrate roughness correlated carrier lifetime

7.2.1 Introduction

As we already mentioned in § 5.2.1, the hetero-polytypic growth of (111) 3C-SiC on (0001) α -SiC with negligible lattice mismatch (~0.1 %) and identical thermal expansion coefficient offers a solution to mentioned problems by reducing the density of stacking faults (SF), while another type of structural defect (double-positioning boundary) appears since two distinguishable orientations of epilayer rotated by 60° with respect to each other have equal growth probability. The promising Vapor-Liquid-Solid deposition (VLS) technique [119] gives a chance to develop a hetero-polytypic thin seed layer of 3C-SiC on which it would be possible to grow thicker layers homo-epitaxially

by Chemical Vapor Deposition (CVD) [120] or Sublimation Epitaxy (SE) [121] techniques.

In this subchapter we study the influence of 6H- and 3C-SiC substrate roughness on the overgrown 3C-SiC epilayer. At the beginning, we study separately the cases of surface polytypic nature, i.e. hexagonal and cubic SiC polytype. Later, we consider all carrier lifetimes under the same structural characteristic, i.e. short range substrate roughness.

7.2.2 Samples and experimental techniques

The sample under study are presented extensively in §5.2.2. Here, we only mention the parameters that we use for this investigation, i.e. FWHM of HRXRD rocking curves at (111) crystallographic direction and RMS of short range roughness of epilayers. The crystal structure was assessed by HRXRD, using Philips X'Pert MRD triple axis diffractometer equipped with a symmetric 4×Ge220 monochromator and symmetric 3×Ge220 analyzer using Cu radiation. Reciprocal space maps (RSM) of the diffracted intensity close to the 111 Bragg peak were recorded. The surface morphology was examined by optical microscope with Nomarski interference contrast and AFM-operating in the tapping mode using Si tips [122].

Bulk lifetime is determined by numerical modeling of DT experimental data in a wide range of excitations. Because of poor layers homogeneity multiple series of measurements are necessary in order to determine the error in lifetime values.

Table 7.2.1 Determined parameters for all (S1/2/3/4) the 3C epilayers. XRD FWHM and RMS roughness are taken from [122]. Lifetimes have been determined at RT.

Layer	S1	S2	S3	S4
Substrate	6H (bare)	6H (polished)	3C/6H (VLS)	3C/6H (VLS+CVD)
FWHM (111) (arcsec)	179	302	144	83
substrate RMS roughness (nm)	2.69	0.52	1.01	0.41
Lifetime (@RT) (ns)	8±3	2.2±1	4.5±2	1.1±0.5

7.2.3 Results and discussion

The low growth rate SE on bare and polished (0001) 6H-SiC substrates, denoted as S1 and S2, respectively, have shown a substantial difference in lifetime values. In Fig. 7.2.1(a) is plotted the bulk lifetime of S1 and S2 layers as a function of their substrate roughness (RMS) in $5 \times 5 \mu\text{m}$ area. As we can see the bulk lifetime increases with the substrate short range roughness. Since in the case of heteroepitaxial growth the initial nucleation of 3C-SiC starts on terraces we assume that the longer terraces results in lower density of double positioning boundaries [165]. On the other hand, the sublimed 1-2 μm of substrate during temperature ramp-up deteriorates the surface optical quality which has been achieved by polishing [166]. Moreover, there exists a general consideration on resulted crystal quality close to surface after polishing processes. It seems that the whole process, even if optimizes the surface flatness and reduces its roughness, creates structural imperfections in the vicinal layers, which in turn transfer them to the overgrown layers. The latter consideration is supported by the substantial reduction of bulk carrier lifetime with the increase of FWHM at (111) crystallographic direction, as in Fig. 7.2.1(b) is depicted.

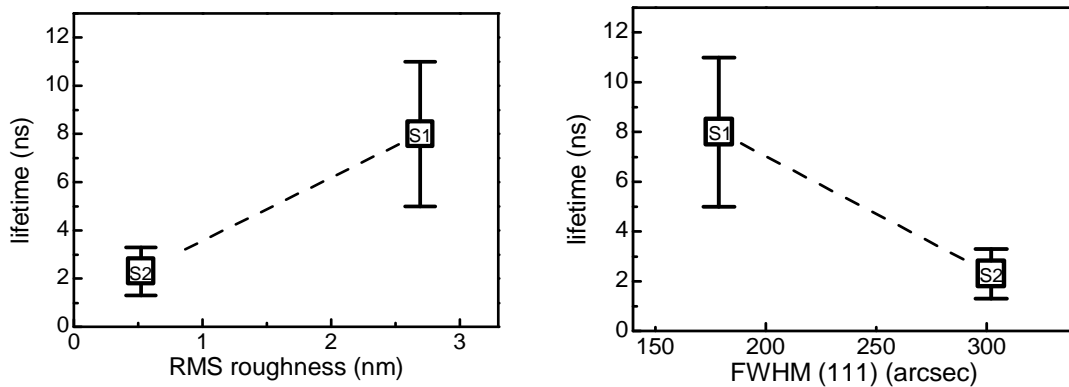


Fig. 7.2.1 Bulk free carrier lifetime as a function of a) substrate RMS roughness obtained by AFM and b) epilayer lattice HRXRD rocking curve FWHM at (111) crystallographic direction.

A similar discussion about the correlation of free carrier lifetime with surface roughness might be extended for samples S3 and S4 that are grown homoepitaxially on thin 3C-SiC seed layers. In latter case, the less rough surface hinders the growth rate since the surface imperfections are energetically favorable for initial nucleation [122]. The lower growth rate on 3C-SiC VLS layer increases the twinning complexity and it is accompanied by formation of other high angle boundaries [167]. It is reported that although a VLS seed layer decreases twin density, it also results in lower material quality if compared to layers grown directly on 6H-SiC substrates [168]. This could be an explanation to initial incoherency with our arguments from previous paragraph on the increase of lifetime with HRXRD rocking curve FWHM. An alternative approach on the subject is that even the concentration of structural defects in sample S4 is lower than those in sample S3, they contain higher amount of non-coherent twin boundaries denoted as $\Sigma=9$ [125]. This type of twin boundary observed in layers grown by SE is wider and hence contains higher amount of structural imperfections than a coherent twin boundary which denoted as $\Sigma=3$. The latter might be the reason for the more effective carrier annihilation at the boundaries of a defect-free volume where carriers can diffuse under lower scattering potentials.

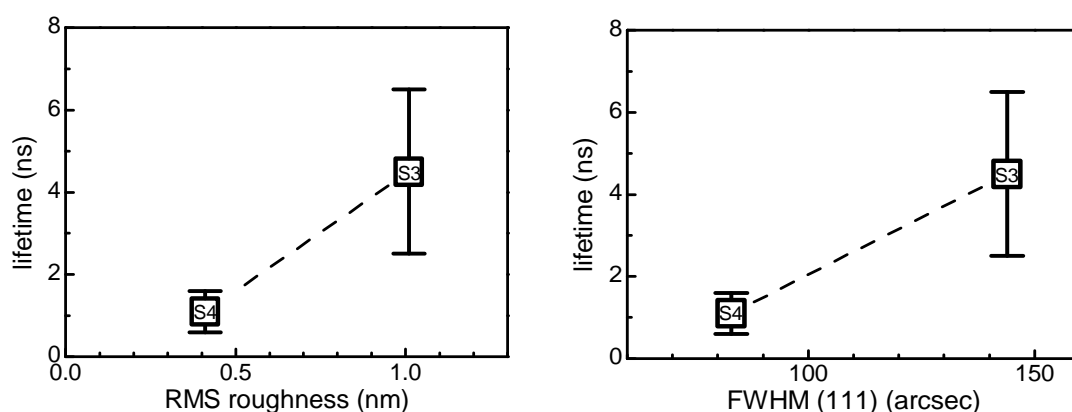


Fig. 7.2.2 Bulk free carrier lifetime as a function of a) substrate RMS roughness obtained by AFM and b) epilayer lattice HRXRD rocking curve FWHM at (111) crystallographic direction.

Regardless the areas and mechanisms which are involved in carrier annihilation, we can summarize the results of Figs. 7.2.1(a) and 7.2.2(a) in in Fig. 7.2.3. In this diagram it is visible that bulk lifetime increases with the short range RMS substrate roughness. This experimentally observed tendency of an electronic property, as lifetime, might be a consequence of homo- and hetero-polytypical nucleation mechanisms of 3C-SiC on SiC substrates by sublimation epitaxial technique. Apart from the fact that epilayer's bulk lifetime increases with short range RMS roughness separately in homo- and hetero-polytypical growth, both cases seem to follow approximately the same relation between lifetime and roughness.

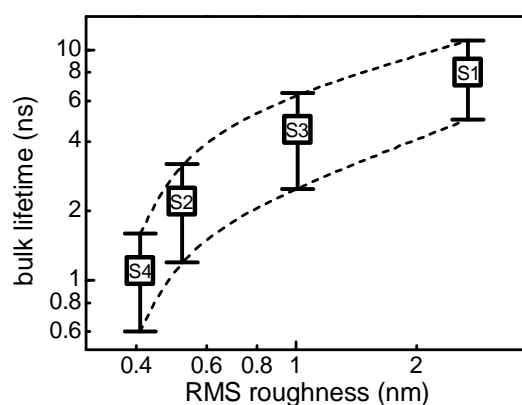


Fig. 7.2.3 Bulk lifetime of 3C-SiC layers grown by sublimation epitaxy as a function of their substrates short range RMS roughness.

7.2.4 Conclusions

Optical differential transmission measurements on cubic SiC layers grown by sublimation epitaxy reveal a monotonous increase of bulk carrier lifetime with short range roughness of SiC substrate, regardless of the polytype. The reasons for this are closely related to 3C-SiC nucleation mechanisms on SiC substrates by sublimation epitaxy.

Prospects

During my PhD studies a number of scientific issues have been investigated. Some of them are already published, some will be published in the near future, and some required further investigation.

As far it concerns 3C-SiC material, it worth to correlate electronic and structural properties of the ultrathin nucleation layers which are critical for the further crystal growth. Nevertheless, further studies have to be continued on differently grown layers assisting the development of high quality 3C-SiC.

As far it concerns carrier dynamics of indirect wide band gap semiconductors, as 3C-SiC is, non-radiative recombination mechanisms and non-equilibrium carrier transport in the regime of degeneracy appear to be promising fields for fundamental research as well as for materials engineering. Several entities, like impurities, intrinsic point and extended defect structures, that contribute differently on carrier dynamics can be determined.

References

- [1] J.J. Berzelius, *Ann. Phys.* **1**:(1824) p.169
- [2] E.G. Acheson, *On Carborundum*, *Chem. News* **68**:(1893) p.179
- [3] U.L. Corborundum <http://www.cumi-murugappa.com/emd/>
- [4] H. Moissan, *Nouvelles recherches sur la météorité de Cañon Diablo*, *Comptes rendus* **139**:(1904) p.
- [5] H. Moissan, *Compt. Rend. Acad. Sci. Paris* **140**:(1905) p.
- [6] G.W. Pierce, *Crystal Rectifiers for Electric Currents and Electric Oscillations. Part I. Carborundum*, *Physical Review (Series I)* **25**(1):(1907) p.31-60
- [7] H.J. Round, *A note on carborundum*, *Electrical World* **49**:(1907) p.309
- [8] H. Baumhauer, *Zeit. Krist* **50**:(1912) p.33
- [9] J.A. Lely, *Darstellung von Einkristallen von Silicium Carbid und Beherrschung von Art und Menge der eingebauten Verunreinigungen*, *Berichte der Deutschen Keramischen Gesellschaft* **32**:(1955) p.229-236
- [10] D.R. Hamilton, *Silicon carbide: a high temperature semiconductor*, Pergamon Press: (1960) p. 521
- [11] V.P. Novikov, *Ionov* **VI**(6b):(1968) p.9-12
- [12] I. Swiderski, W. Proskurowski and T. Niemyski, *Preparation of semiconducting silicon carbide single crystals*, *Journal of Crystal Growth* **5**(1):(1969) p.59-64
- [13] Y.M. Tairov and V.F. Tsvetkov, *Investigation of growth processes of ingots of silicon carbide single crystals*, *Journal of Crystal Growth* **43**(2):(1978) p.209-212
- [14] J.T. Kendal, *Silicon Carbide: A High Temperature Semiconductor*, Pergamon Press: (1960) p. 521
- [15] S. Nishino, J.A. Powell and H.A. Will, *Production of large-area single-crystal wafers of cubic SiC for semiconductor devices*, *Applied Physics Letters* **42**(5):(1983) p.460-462
- [16] J.C. Phillips and G. Lucovsky *Bonds and Bands in Semiconductors*. New Jersey, Momentum Press (2009)

- [17] H. Jagodzinski, *Eindimensionale Fehlordnung in Kristallen und ihr Einfluss auf die Röntgeninterferenzen. I. Berechnung des Fehlordnungsgrades aus den Röntgenintensitäten*, Acta Crystallographica **2**(4):(1949) p.201-207
- [18] D. Perrone, "*Process and characterisation techniques on 4H - Silicon Carbide*", PhD Thesis, (2007)
- [19] M.B.J. Wijesundara and R.G. Azevedo *Silicon Carbide Microsystems for Harsh Environments*. New York, Springer (2011)
- [20] H. Morkoc, S. Strite, G.B. Gao, M.E. Lin, B. Sverdlov and M. Burns, *Large-band-gap SiC, III-V nitride, and II-VI ZnSe-based semiconductor device technologies*, Journal of Applied Physics **76**(3):(1994) p.1363-1398
- [21] K. Takahashi, A. Yoshikawa and A. Sandhu (Eds.), "*Wide Bandgap Semiconductors - Fundamental Properties and Modern Photonic and Electronic Devices*" Berlin Heidelberg, Springer-Verlag (2007)
- [22] E. Janzen, A. Gali, A. Henry, I. Ivanov, B. Magnusson and N. Son, *Defects in SiC*, in "*Defects in Microelectronic Materials and Devices*", CRC Press (2008)
- [23] R. Hull Properties of Crystalline Silicon, Institution of Engineering and Technology.
- [24] Z.C. Feng (Ed.), "*III-Nitride Devices and Nanoengineering*" London, Imperial College Press (2008)
- [25] P. Masri, *Silicon carbide and silicon carbide-based structures: The physics of epitaxy*, Surface Science Reports **48**(1-4):(2002) p.1-51
- [26] R.S. Ramsdell, American Mineralogist **32**:(1947) p.64-82
- [27] S.E. Saddow and A. Agarwal (Eds.), "*Advances in Silicon Carbide Processing and Applications*" Norwood, Artech House, Inc. (2004)
- [28] S.E. Saddow (Ed.), "*Silicon Carbide Biotechnology: A Biocompatible Semiconductor for Advanced Biomedical Devices and Applications*", Elsevier (2012)
- [29] A.A. Lebedev and V.E. Chelnokov, *Wide-gap semiconductors for high-power electronics*, Semiconductors **33**(9):(1999) p.999-1001
- [30] C.I. Harris and A.O. Konstantinov, *Recent developments in SiC device research*, Physica Scripta **1999**(T79):(1999) p.27
- [31] E.W.S. Caetano, E.F. Bezerra, V.N. Freire, J.A.P. da Costa and E.F. da Silva, *Ultrafast electron drift velocity overshoot in 3C-SiC*, Solid State Communications **113**(9):(2000) p.539-542

- [32] F. Ciobanu, G. Pensl, H. Nagasawa, A. Schoner, S. Dimitrijević, K.Y. Cheong, V.V. Afanas'ev and G. Wagner, *Traps at the interface of 3C-SiC/SiO₂-MOS-structures*, in "Silicon Carbide and Related Materials - 2002", P. Bergman and E. Janzen (Eds.), Zurich-Uetikon, Trans Tech Publications Ltd, **433-4**: 551-554 (2002)
- [33] S.E. Saddow and A. Agarwal (Eds.), "Advances in Silicon Carbide Processing and Applications", Semiconductor Materials and Devices Series Boston, Artech House (2004)
- [34] D.K. Schroder *Semiconductor material and device characterization*. New Jersey, John Wiley & Sons, Inc. (2006)
- [35] A. Schöner, M. Krieger, G. Pensl, M. Abe and H. Nagasawa, *Fabrication and Characterization of 3C-SiC-Based MOSFETs*, Chemical Vapor Deposition **12**(8-9):(2006) p.523-530
- [36] V.M. Polyakov and F. Schwierz, *Formation of two-dimensional electron gases in polytypic SiC heterostructures*, Journal of Applied Physics **98**(2):(2005) p.023709-023706
- [37] A. Fissel, *Artificially layered heteropolytypic structures based on SiC polytypes: molecular beam epitaxy, characterization and properties*, Physics Reports **379**(3-4):(2003) p.149-255
- [38] M.V.S. Chandrashekhar, C.I. Thomas, J. Lu and M.G. Spencer, *Observation of a two dimensional electron gas formed in a polarization doped C-face 3C/4H SiC heteropolytype junction*, Applied Physics Letters **91**(3):(2007) p.033503-033503
- [39] A.A. Lebedev, D.K. Nel'son, B.S. Razbirin, I.I. Sadashev, A.N. Kuznetsov and A.E. Cherenkov, *Study of the Properties of a Two-Dimensional Electron Gas in p--3C-SiC/n+-6H-SiC Heterostructures at Low Temperatures*, Semiconductors **39**(10):(2005) p.1194-1196
- [40] B.S. Richards, A. Lambertz, R.P. Corkish, C.A. Zorman, M. Mehregany, M. Ionescu and G. M.A., *3C-SiC as a future photovoltaic material*. Photovoltaic Energy Conversion, Osaka, Japan, IEEE, **3**: (2003) p. 2738-2741
- [41] G. Beaucarne, A.S. Brown, M.J. Keevers, R. Corkish and M.A. Green, *The impurity photovoltaic (IPV) effect in wide-bandgap semiconductors: an opportunity for very-high-efficiency solar cells?*, Progress in Photovoltaics: Research and Applications **10**(5):(2002) p.345-353
- [42] A. Luque and A. Martí, *Increasing the Efficiency of Ideal Solar Cells by Photon Induced Transitions at Intermediate Levels*, Physical Review Letters **78**(26):(1997) p.5014-5017

- [43] J. Lorenzi, G. Zoulis, M. Marinova, O. Kim-Hak, J.W. Sun, N. Jegenyés, H. Peyre, F. Cauwet, P. Chaudouet, M. Soueidan, D. Carole, J. Camassel, E.K. Polychroniadis and G. Ferro, *Incorporation of group III, IV and V elements in 3C-SiC(111) layers grown by the vapour-liquid-solid mechanism*, Journal of Crystal Growth **312**(23):(2010) p.3443-3450
- [44] A.A. Lebedev, *Influence of native defects on polytypism in SiC*, Semiconductors **33**(7):(1999) p.707-709
- [45] H.H. Woodbury and G.W. Ludwig, *Electron Spin Resonance Studies in SiC*, Physical Review **124**(4):(1961) p.1083-1089
- [46] H. Itoh, M. Yoshikawa, I. Nashiyama, S. Misawa, H. Okumura and S. Yoshida, *Radiation induced defects in CVD-grown 3C-SiC*, Nuclear Science, IEEE Transactions on **37**(6):(1990) p.1732-1738
- [47] P.B. Klein, R. Myers-Ward, K.K. Lew, B.L. VanMil, J.C.R. Eddy, D.K. Gaskill, A. Shrivastava and T.S. Sudarshan, *Recombination processes controlling the carrier lifetime in n⁻4H-SiC epilayers with low Z_{1/2} concentrations*, Journal of Applied Physics **108**(3):(2010) p.033713-033711
- [48] G. Zoulis, "*Structural and Optical Characterisation of SiC*", PhD Thesis, (2011)
- [49] H.P. Iwata, U. Lindefelt, S. Öberg and P.R. Briddon, *Theoretical study of planar defects in silicon carbide*, Journal of Physics: Condensed Matter **14**(48):(2002) p.12733
- [50] H.P. Iwata, U. Lindefelt, S. Öberg and P.R. Briddon, *Stacking faults in silicon carbide*, Physica B: Condensed Matter **340–342**(0):(2003) p.165-170
- [51] U. Lindefelt, H. Iwata, S. Öberg and P.R. Briddon, *Stacking faults in 3C-, 4H-, and 6H-SiC polytypes investigated by an ab initio supercell method*, Physical Review B **67**(15):(2003) p.155204
- [52] H. Iwata, U. Lindefelt, S. Öberg and P.R. Briddon, *Localized electronic states around stacking faults in silicon carbide*, Physical Review B **65**(3):(2001) p.033203
- [53] H.P. Iwata, U. Lindefelt, S. Öberg and P.R. Briddon, *Ab initio study of 3C inclusions and stacking fault--stacking fault interactions in 6H-SiC*, Journal of Applied Physics **94**(8):(2003) p.4972-4979
- [54] R.S. Wagner and W.C. Ellis, *Vapor-Liquid-solid mechanism of single crystal growth*, Applied Physics Letters **4**(5):(1964) p.89-90

- [55] X.T. Zhou, N. Wang, F.C.K. Au, H.L. Lai, H.Y. Peng, I. Bello, C.S. Lee and S.T. Lee, *Growth and emission properties of β -SiC nanorods*, Materials Science and Engineering: A **286**(1):(2000) p.119-124
- [56] J. Lorenzzi, "*Growth and doping of heteroepitaxial 3C-SiC layers on α -SiC substrates using Vapour-Liquid-Solid mechanism*", PhD Thesis, (2010)
- [57] M. Soueidan, G. Ferro, J. Dazord, Y. Monteil and G. Younes, *Surface preparation of α -SiC for the epitaxial growth of 3C-SiC*, Journal of Crystal Growth **275**(1-2):(2005) p.e1011-e1016
- [58] H. Nagasawa and K. Yagi, *3C-SiC Single-Crystal Films Grown on 6-Inch Si Substrates*, physica status solidi (b) **202**(1):(1997) p.335-358
- [59] H. Nagasawa, K. Yagi, T. Kawahara and N. Hatta, *Reducing Planar Defects in 3C-SiC*, Chemical Vapor Deposition **12**(8-9):(2006) p.502-508
- [60] H. Nagasawa, T. Kawahara, K. Yagi, N. Hatta, H. Uchida, M. Kobayashi, S. Reshanov, R. Esteve and A. Schoner, *High Quality 3C-SiC Substrate for MOSFET Fabrication*, in "*Heterosic & Wasmpe 2011*", D. Alquier (Ed.), Stafa-Zurich, Trans Tech Publications Ltd, **711**: 91-98 (2012)
- [61] A. Boule, D. Chaussende, F. Conchon, G. Ferro and O. Masson, *Characterization of stacking faults in thick 3C-SiC crystals using high-resolution diffuse X-ray scattering*, Journal of Crystal Growth **310**(5):(2008) p.982-987
- [62] W.J. Choyke, H. Matsunami and G. Pensl *Silicon Carbide: Recent major advances*. New York, Springer (2004)
- [63] M. Syväjarvi and R. Yakimova P. Bhattacharya, R. Fornari and H. Kamimura *Sublimation Epitaxial Growth of Hexagonal and Cubic SiC*. Comprehensive Semiconductor Science and Technology. P. Bhattacharya, R. Fornari and H. Kamimura, Elsevier: (2011) p.
- [64] M. Beshkova, M. Syvajarvi, R. Vasiliauskas, J. Birch and R. Yakimova, *Structural Properties of 3C-SiC Grown by Sublimation Epitaxy*, in "*Silicon Carbide and Related Materials 2008*", A. PerezTomas, P. Godignon, M. Vellvehi and P. Brosselard (Eds.), Stafa-Zurich, Trans Tech Publications Ltd, **615-617**: 181-184 (2009)
- [65] W.M. Vetter and M. Dudley, *Characterization of defects in 3C-silicon carbide crystals*, Journal of Crystal Growth **260**(1-2):(2004) p.201-208
- [66] D. Chaussende, J. Eid, F. Mercier, R. Madar and M. Pons, *Nucleation and Growth of 3C-SiC Single Crystals from the Vapor Phase*, in "*Silicon Carbide and Related Materials 2008*", A. PerezTomas, P. Godignon, M. Vellvehi and P. Brosselard (Eds.), **615-617**: 31-36 (2009)

- [67] D. Chaussende, M. Ucar, L. Auvray, F. Baillet, M. Pons and R. Madar, *Control of the supersaturation in the CF-PVT process for the growth of silicon carbide crystals: Research and applications*, Crystal Growth & Design **5**(4):(2005) p.1539-1544
- [68] M. Soueidan, G. Ferro, B. Nsouli, M. Roumie, E. Polychroniadis, M. Kazan, S. Juillaguet, D. Chaussende, N. Habka, J. Stoemenos, J. Camassel and Y. Monteil, *Characterization of a 3C-SiC single domain grown on 6H-SiC(0001) by a vapor-liquid-solid mechanism*, Crystal Growth & Design **6**(11):(2006) p.2598-2602
- [69] R. Menzel *Photonics: Linear and Nonlinear Interactions of Laser Light and Matter*. Berlin, Springer-Verlag (2007)
- [70] H.J. Eichler, P. Gunder and D.W. Pohl *Laser-Induced Dynamic Gratings*. Berlin, Heidelberg, Springer-Verlag (1986)
- [71] P. Grivickas, "*Optical Studies of Carrier Transport and Fundamental Absorption in 4H-SiC and Si*", PhD Thesis, (2004)
- [72] B.K. Ridley *Quantum Processes in Semiconductors*. Oxford, Oxford University Press (1999)
- [73] B. Pödör, *Electron Mobility in Plastically Deformed Germanium*, physica status solidi (b) **16**(2):(1966) p.K167-K170
- [74] R.L. Petritz, *Theory of Photoconductivity in Semiconductor Films*, Physical Review **104**(6):(1956) p.1508-1516
- [75] J.W. Orton and M.J. Powell, *The Hall effect in polycrystalline and powdered semiconductors*, Reports on Progress in Physics **43**(11):(1980) p.1263
- [76] M. Grundmann *The Physics of Semiconductors*. Heidelberg, Springer (2010)
- [77] H.K. Sy, D.K. Desai and C.K. Ong, *Electron Screening and Mobility in Heavily Doped Silicon*, physica status solidi (b) **130**(2):(1985) p.787-792
- [78] J. Linnros, *Carrier lifetime measurements using free carrier absorption transients. I. Principle and injection dependence*, Journal of Applied Physics **84**(1):(1998) p.275-283
- [79] A.B. Sproul, *Dimensionless solution of the equation describing the effect of surface recombination on carrier decay in semiconductors*, Journal of Applied Physics **76**(5):(1994) p.2851-2854
- [80] S.M. Ryvkin *Photoelectric Effects in Semiconductors*. New York, Consultants Bureau (1964)

- [81] M. Ichimura, *Temperature dependence of a slow component of excess carrier decay curves*, Solid-State Electronics **50**(11-12):(2006) p.1761-1766
- [82] P.P. Debye and E.M. Conwell, *Electrical Properties of N-Type Germanium*, Physical Review **93**(4):(1954) p.693-706
- [83] G.L. Pearson and J. Bardeen, *Electrical Properties of Pure Silicon and Silicon Alloys Containing Boron and Phosphorus*, Physical Review **75**(5):(1949) p.865-883
- [84] B. Podor, *Thermal ionization energy of Mg acceptors in GaN: effects of doping level and compensation*. International Conference on Solid State Crystals 2000: Growth, Characterization, and Applications of Single Crystals, Zakopane, Poland, SPIE, 4412: (2001)
- [85] J. Monecke, W. Siegel, E. Ziegler and G. Kühnel, *On the Concentration Dependence of the Thermal Impurity-to-Band Activation Energies in Semiconductors*, physica status solidi (b) **103**(1):(1981) p.269-279
- [86] K. Jarasiunas, *Nonlinear optical characterization of photoelectrical properties of wide bandgap semiconductors by time-resolved four-wave mixing technique*, in "Wide Bandgap Materials and New Developments", M. Syväjärvi and R. Yakimova (Eds.), Kerala, India, Research Singpost (2006)
- [87] J. Linnros and V. Grivickas, *Carrier lifetime: free carrier absorption, photoconductivity, and photoluminescence*, in "Characterization of Materials", E. N. Kaufmann (Ed.), New Jersey, John Wiley & Sons (2003)
- [88] P. Scajev, V. Gudelis, K. Jarasiunas and P.B. Klein, *Fast and slow carrier recombination transients in highly excited 4H-and 3C-SiC crystals at room temperature*, Journal of Applied Physics **108**(2):(2010) p.
- [89] V. Grivickas, A. Galeckas, V. Bikbajevs, J. Linnros and J.A. Tellefsen, *Spatially and time-resolved infrared absorption for optical and electrical characterization of indirect band gap semiconductors*, Thin Solid Films **364**(1-2):(2000) p.181-185
- [90] P. Grivickas, V. Grivickas and J. Linnros, *Excitonic Absorption above the Mott Transition in Si*, Physical Review Letters **91**(24):(2003) p.246401
- [91] V. Grivickas, G. Manolis, K. Gulbinas, K. Jarasiunas and M. Kato, *Excess carrier recombination lifetime of bulk n-type 3C-SiC*, Applied Physics Letters **95**(24):(2009) p.242110
- [92] J. Linnros and V. Grivickas, *Carrier lifetime: Free carrier absorption, Photoluminescence and Photoconductivity*, in "Characterization of materials", E. N. Kaufman (Ed.), New Jersey, John Wiley & Sons Inc. (2000)

- [93] M. Kawai, T. Mori, M. Kato, M. Ichimura, S. Sumie and H. Hashizume, *Excess carrier lifetimes in a bulk p-type SiC wafer measured by the microwave photoconductivity decay method*, in "Silicon Carbide and Related Materials 2006", N. Wright, C. M. Johnson, K. Vassilevski, I. Nikitina and A. Horsfall (Eds.), Stafa-Zurich, Trans Tech Publications Ltd, **556-557**: 359-362 (2007)
- [94] S.A. Reshanov, K. Schneider, R. Helbig, G. Pensl, H. Nagasawa and A. Schoner, *Midgap defects in 4H-, 6H- and 3C-SiC detected by deep level optical spectroscopy*, in "Silicon Carbide and Related Materials 2003, Prts 1 and 2", R. Madar and J. Camassel (Eds.), Zurich-Uetikon, Trans Tech Publications Ltd, **457-460**: 513-516 (2004)
- [95] J.P. Bergman, *Carrier lifetimes in SiC, studied by time resolved photoluminescence spectroscopy*, Diamond and Related Materials **6**(10):(1997) p.1324-1328
- [96] P. Grivickas, A. Galeckas, J. Linnros, M. Syvajarvi, R. Yakimova, V. Grivickas and J.A. Tellefsen, *Carrier lifetime investigation in 4H-SiC grown by CVD and sublimation epitaxy*, Materials Science in Semiconductor Processing **4**(1-3):(2001) p.191-194
- [97] A. Galeckas, J. Linnros, M. Frischholz and V. Grivickas, *Optical characterization of excess carrier lifetime and surface recombination in 4H/6H-SiC*, Applied Physics Letters **79**(3):(2001) p.365-367
- [98] P.B. Klein, *Carrier lifetime measurement in n[^{sup} -] 4H-SiC epilayers*, Journal of Applied Physics **103**(3):(2008) p.033702-033714
- [99] M. Ichimura, H. Tajiri, Y. Morita, N. Yamada and A. Usami, *Excess carrier lifetime of 3C-SiC measured by the microwave photoconductivity decay method*, Applied Physics Letters **70**(13):(1997) p.1745-1747
- [100] M. Ichimura, N. Yamada, H. Tajiri and E. Arai, *Slow photoconductivity decay in 3C-SiC on Si substrates*, Journal of Applied Physics **84**(5):(1998) p.2727-2731
- [101] A. Galeckas, A.Y. Kuznetsov, T. Chassagne, G. Ferro, J. Linnros and V. Grivickas, *Optical investigation of the built-in strain in 3C-SiC epilayers*, in "Silicon Carbide and Related Materials 2003, Prts 1 and 2", R. Madar and J. Camassel (Eds.), Zurich-Uetikon, Trans Tech Publications Ltd, **457-460**: 657-660 (2004)
- [102] K. Neimontas, K. Jarasiunas, M. Soueidan, G. Ferro and Y. Monteil, *Nonequilibrium carrier dynamics in DPB-Free 3C-SiC layer studied by dynamic grating technique in wide excitation and temperature range*, in "Silicon Carbide and Related Materials 2006", N. Wright, C. M. Johnson, K. Vassilevski, I. Nikitina and A. Horsfall (Eds.), Stafa-Zurich, Trans Tech Publications Ltd, **556-557**: 395-398 (2007)

- [103] G. Manolis, K. Jarasiunas, I.G. Galben and D. Chaussende, *Optical Investigation of Electronic Properties in Bulk and Surface Region of Sublimation-grown 3C-SiC Crystals*, in "Silicon Carbide and Related Materials 2008", A. PerezTomas, P. Godignon, M. Vellvehi and P. Brosselard (Eds.), **615-617**: 303-306 (2009)
- [104] P. Scajev, K. Jarasiunas, A. Kadys, J. Storasta, P.L. Abramov, S.P. Lebedev and A.A. Lebedev, *Impact of nonintentional Al impurity to carrier lifetime and diffusion in sublimation grown 3C heterostructures*, in "2010 Wide Bandgap Cubic Semiconductors: From Growth to Devices", G. Ferro and P. Siffert (Eds.), **1292**: 107-110 (2010)
- [105] V. Grivickas, J. Linnros, A. Vigelis, J. Seckus and J.A. Tellefsen, *A study of carrier lifetime in silicon by laser-induced absorption: a perpendicular geometry measurement*, Solid-State Electronics **35**(3):(1992) p.299-310
- [106] J.W. Sun, I.G. Ivanov, R. Liljedahl, R. Yakimova and M. Syvajarvi, *Considerably long carrier lifetimes in high-quality 3C-SiC(111)*, Applied Physics Letters **100**(25):(2012) p.252101-252105
- [107] K. Jarasiunas, P. Scajev, V. Gudelis, P.B. Klein and M. Kato, *Nonequilibrium carrier recombination in highly excited bulk SiC crystals*, in "Silicon Carbide and Related Materials 2009, Pts 1 and 2", A. J. Bauer, P. Friedrichs, M. Krieger, G. Pensl, R. Rupp and T. Seyller (Eds.), **645-648**: 215-218 (2010)
- [108] A. Haug, *Band-to-band Auger recombination in semiconductors*, Journal of Physics and Chemistry of Solids **49**(6):(1988) p.599-605
- [109] L. Huldt, *Band-to-band auger recombination in indirect gap semiconductors*, physica status solidi (a) **8**(1):(1971) p.173-187
- [110] A. Haug, *Auger Recombination with Deep Impurities in Indirect Band Gap Semiconductors*, physica status solidi (b) **108**(2):(1981) p.443-448
- [111] D. Macdonald, A. Cuevas and J. Wong-Leung, *Capture cross sections of the acceptor level of iron--boron pairs in p-type silicon by injection-level dependent lifetime measurements*, Journal of Applied Physics **89**(12):(2001) p.7932-7939
- [112] D. Macdonald and A. Cuevas, *Validity of simplified Shockley-Read-Hall statistics for modeling carrier lifetimes in crystalline silicon*, Physical Review B **67**(7):(2003) p.075203
- [113] T. Yamada and K.M. Itoh, *Optical and electrical characterization of free-standing 3C-SiC films grown on undulant Si substrates*, in "Silicon

Carbide and Related Materials 2001, Pts 1 and 2, Proceedings", S. Yoshida, S. Nishino, H. Harima and T. Kimoto (Eds.), **389-3**: 675-678 (2002)

[114] D. Macdonald and A. Cuevas, *Trapping of minority carriers in multicrystalline silicon*, Applied Physics Letters **74**(12):(1999) p.1710-1712

[115] G. Pensl, T. Frank, M. Krieger, M. Laube, S. Reshanov, F. Schmid and M. Weidner, *Implantation-induced defects in silicon carbide*, Physica B-Condensed Matter **340**:(2003) p.121-127

[116] H. Nagasawa, K. Yagi and T. Kawahara, *3C-SiC hetero-epitaxial growth on undulant Si(0 0 1) substrate*, Journal of Crystal Growth **237–239, Part 2**(0):(2002) p.1244-1249

[117] E. Polychroniadis, M. Syväjärvi, R. Yakimova and J. Stoemenos, *Microstructural characterization of very thick freestanding 3C-SiC wafers*, Journal of Crystal Growth **263**(1–4):(2004) p.68-75

[118] J. Stoemenos, C. Dezauzier, G. Arnaud, S. Contreras, J. Camassel, J. Pascual and J.L. Robert, *Structural, optical and electrical properties of state of the art cubic SiC films*, Materials Science and Engineering: B **29**(1–3):(1995) p.160-164

[119] M. Soueidan and G. Ferro, *A vapor-liquid-solid mechanism for growing 3C-SiC single-domain layers on 6H-SiC(0001)*, Advanced Functional Materials **16**(7):(2006) p.975-979

[120] J.A. Powell, D.J. Larkin, L.G. Matus, W.J. Choyke, J.L. Bradshaw, L. Henderson, M. Yoganathan, J. Yang and P. Pirouz, *Growth of improved quality 3C-SiC films on 6H-SiC substrates*, Applied Physics Letters **56**(14):(1990) p.1353-1355

[121] A.N. Andreev, A.S. Tregubova, M.P. Scheglov, A.L. Syrkin and V.E. Chelnokov, *Influence of growth conditions on the structural perfection of β -SiC epitaxial layers fabricated on 6H-SiC substrates by vacuum sublimation*, Materials Science and Engineering: B **46**(1–3):(1997) p.141-146

[122] M. Beshkova, J. Lorenzzi, N. Jegenyes, J. Birch, M. Syvajarvi, G. Ferro and R. Yakimova, *Properties of 3C-SiC Grown by Sublimation Epitaxy on Different Type of Substrates*, Silicon Carbide and Related Materials 2009, Pts 1 and 2 **645-648**:(2010) p.183-186

[123] M. Soueidan, G. Ferro, O. Kim-Hak, F. Cauwet and B. Nsouli, *Vapor-liquid-solid growth of 3C-SiC on alpha-SiC substrates. 1. Growth mechanism*, Crystal Growth & Design **8**(3):(2008) p.1044-1050

[124] M. Soueidan, G. Ferro, B. Nsouli, F. Cauwet, J. Dazord, G. Younes and Y. Monteil, *Effect of growth parameters on the heteroepitaxy of 3C-SiC on 6H-*

SiC substrate by chemical vapor deposition, Materials Science and Engineering B-Solid State Materials for Advanced Technology **130**(1-3):(2006) p.66-72

[125] M. Marinova, A. Mantzari, M. Beshkova, M. Syvajarvi, R. Yakimova and E.K. Polychroniadis, The Influence of the Temperature Gradient on the Defect Structure of 3C-SiC Grown Heteroepitaxially on 6H-SiC by Sublimation Epitaxy, Journal **645-648**:(2010) p.367-370

[126] G. Ferro A. J. Bauer, P. Friedrichs, M. Krieger, G. Pensl, R. Rupp and T. Seyller Overview of 3C-SiC Crystalline Growth. Silicon Carbide and Related Materials 2009, Pts 1 and 2. A. J. Bauer, P. Friedrichs, M. Krieger, G. Pensl, R. Rupp and T. Seyller. Stafa-Zurich, Trans Tech Publications Ltd. **645-648**:(2010) p. 49-54.

[127] P. Scajev, A. Usikov, V. Soukhoveev, R. Aleksiejunas and K. Jarasiunas, *Diffusion-limited nonradiative recombination at extended defects in hydride vapor phase epitaxy GaN layers*, Applied Physics Letters **98**(20):(2011) p.202105-202103

[128] N. Jegenyés, G. Manolis, J. Lorenzini, V. Souliere, D. Dompont, A. Boule, G. Ferro and K. Jarasiunas, *Nondestructive evaluation of photo-electrical properties of 3C-SiC (111) homoepitaxial layers grown by CVD*, Silicon Carbide and Related Materials 2010 **679-680**:(2011) p.153-156

[129] M. Marinova, A. Mantzari, M. Beshkova, M. Syvajarvi, R. Yakimova and E.K. Polychroniadis, *TEM investigation of the 3C/6H-SiC transformation interface in layers grown by sublimation epitaxy*, in "Applied Crystallography Xxi", D. Stroz and M. Karolus (Eds.), Stafa-Zurich, Trans Tech Publications Ltd, **163**: 97-100 (2010)

[130] M. Marinova, N. Jegenyés, A. Andreadou, A. Mantzari, J. Lorenzini, G. Ferro and E.K. Polychroniadis, *Defects in (111) 3C-SiC layers grown at different temperatures by VLS and CVD on 6H-SiC substrates*, AIP Conference Proceedings **1292**(1):(2010) p.95-98

[131] L. Latu-Romain, D. Chaussende, C. Balloud, S. Juillaguet, L. Rapenne, E. Pernot, J. Camassel, M. Pons and R. Madar, *Characterization of bulk (111) 3C-SiC single crystals grown on 4H-SiC by the CF-PVT method*, in "Silicon Carbide and Related Materials 2005, Pts 1 and 2", R. P. Devaty (Ed.), **527-529**: 99-102 (2006)

[132] A.A. Lebedev, *Heterojunctions and superlattices based on silicon carbide*, Semiconductor Science and Technology **21**(6):(2006) p.R17

[133] G. Pensl and W.J. Choyke, *Electrical and optical characterization of SiC*, Physica B-Condensed Matter **185**(1-4):(1993) p.264-283

- [134] A.A. Lebedev *Structural defects and deep acceptors in silicon carbide*. New York, IEEE (1998)
- [135] A. Henry, C. Hallin, I.G. Ivanov, J.P. Bergman, O. Kordina, U. Lindefelt and E. Janzén, *Ga-bound excitons in 3C-, 4H-, and 6H-SiC*, Physical Review B **53**(20):(1996) p.13503-13506
- [136] MANSiC <http://www.mansic.eu/>
- [137] G. Ferro, O. Kim-Hak, J. Lorenzzi, N. Jegenyés, M. Marinova, M. Soueidan, D. Carole and E.K. Polychroniadis, *On the mechanism of twin boundary elimination in 3C-SiC(111) heteroepitaxial layers on alpha-SiC substrates*, in "Silicon Carbide and Related Materials 2010", E. V. Monakhov, T. Hornos and B. G. Svensson (Eds.), Stafa-Zurich, Trans Tech Publications Ltd, **679-680**: 71-74 (2011)
- [138] M. Soueidan, G. Ferro, O. Kim-Hak, N. Habka, V. Souliere and B. Nsouli, *Vapor-liquid-solid growth of 3C-SiC on alpha-SiC substrates. 2. Growth kinetics*, Crystal Growth & Design **8**(3):(2008) p.1051-1054
- [139] A.O. Konstantinov, C. Hallin, O. Kordina and E. Janzen, *Effect of vapor composition on polytype homogeneity of epitaxial silicon carbide*, Journal of Applied Physics **80**(10):(1996) p.5704-5712
- [140] J. Camassel, S. Juillaguet, M. Zielinski and C. Balloud, *Application of LTPL Investigation Methods to CVD-Grown SiC*, Chemical Vapor Deposition **12**(8-9):(2006) p.549-556
- [141] J.M. Dorkel and P. Leturcq, *Carrier mobilities in silicon semi-empirically related to temperature, doping and injection level*, Solid-State Electronics **24**(9):(1981) p.821-825
- [142] T. Malinauskas, K. Jarasiunas, M. Heuken, F. Scholz and P. Bruckner, *Diffusion and recombination of degenerate carrier plasma in GaN*, in "Physica Status Solidi C: Current Topics in Solid State Physics, Vol 6, Suppl 2", R. Butte (Ed.), **6**: S743-S746 (2009)
- [143] N. Jegenyés, J. Lorenzzi, V. Soulière, J. Dazord, F. Cauwet and F. G., *Investigation of 3C-SiC(111) homoepitaxial growth by CVD at high temperature*, Materials Science Forum **645-648**:(2010) p.127-130
- [144] D. Dompont, A. Boulle, I.G. Galben-Sandulache and D. Chaussende, *Diffuse X-ray scattering from partially transformed 3C-SiC single crystals*, Nuclear Instruments and Methods in Physics Research Section B: Beam Interactions with Materials and Atoms **284**(0):(2012) p.19-22
- [145] A.S. Grove *Physics and Technology of Semiconductor Devices* Wiley (1967)

- [146] G. Manolis, G. Zoulis, S. Juillaguet, J. Lorenzzi, G. Ferro, J. Camassel and K. Jarasiunas, *Optical characterization of VLS+CVD grown 3C-SiC films by non-linear and photoluminescence techniques*, in "Silicon Carbide and Related Materials 2009, Pts 1 and 2", A. J. Bauer, P. Friedrichs, M. Krieger, G. Pensl, R. Rupp and T. Seyller (Eds.), **645-648**: 443-446 (2010)
- [147] P. Scajev, J. Hassan, K. Jarasiunas, M. Kato, A. Henry and J.P. Bergman, *Comparative Studies of Carrier Dynamics in 3C-SiC Layers Grown on Si and 4H-SiC Substrates*, Journal of Electronic Materials **40**(4):(2011) p.394-399
- [148] P.B. Klein, A. Shrivastava and T.S. Sudarshan, *Slow de-trapping of minority holes in n-type 4H-SiC epilayers*, physica status solidi (a) **208**(12):(2011) p.2790-2795
- [149] L. Latu-Romain, D. Chaussende, P. Chaudouët, F. Robaut, G. Berthomé, M. Pons and R. Madar, *Study of 3C-SiC nucleation on (0 0 0 1) 6H-SiC nominal surfaces by the CF-PVT method*, Journal of Crystal Growth **275**(1-2):(2005) p.e609-e613
- [150] J. Eid, I.G. Galben, G. Zoulis, T. Robert, D. Chaussende, S. Juillaguet, A. Tiberj and J. Camassel, *Nitrogen Doping of 3C-SiC Single Crystals Grown by CF-PVT*, in "Silicon Carbide and Related Materials 2008", T. A. Perez, P. Godignon, M. Vellvehi and P. Brosselard (Eds.), Stafa-Zurich, Trans Tech Publications Ltd, **615-617**: 45-48 (2009)
- [151] D. Chaussende, F. Baillet, L. Charpentier, E. Pernot, M. Pons and R. Madar, *Continuous feed physical vapor transport - Toward high purity and long boules growth of SiC*, Journal of the Electrochemical Society **150**(10):(2003) p.G653-G657
- [152] D. Chaussende, C. Balloud, L. Auvray, F. Baillet, M. Zielinski, S. Juillaguet, M. Mermoux, E. Pernot, J. Camassel, M. Pons and R. Madar, *Characterization of thick 2-inch 4H-SiC layers grown by the Continuous Feed - Physical Vapor Transport method*, in "Silicon Carbide and Related Materials 2003, Prts 1 and 2", R. Madar and J. Camassel (Eds.), **457-460**: 91-94 (2004)
- [153] H. Yugami, S. Nakashima, A. Mitsuishi, A. Uemoto, M. Shigeta, K. Furukawa, A. Suzuki and S. Nakajima, *Characterization of the free-carrier concentrations in doped beta-SiC crystals by Raman scattering*, Journal of Applied Physics **61**(1):(1987) p.354-358
- [154] K. Neimontas, T. Malinauskas, R. Aleksiejūnas, M. Sūdžius, K. Jarašiūnas, L. Storasta, J.P. Bergman and E. Janzen, *The determination of high-density carrier plasma parameters in epitaxial layers, semi-insulating and heavily doped crystals of 4H-SiC by a picosecond four-wave mixing technique*, Semiconductor Science and Technology **21**(7):(2006) p.952

- [155] P. Grivickas, J. Linnros and V. Grivickas, *Free carrier diffusion measurements in epitaxial 4H-SiC with a Fourier transient grating technique: Injection dependence*, in "Silicon Carbide and Related Materials - 1999 Pts, 1 & 2", C. H. Carter, R. P. Devaty and G. S. Rohrer (Eds.), Zurich-Uetikon, Trans Tech Publications Ltd, **338-3**: 671-674 (2000)
- [156] J.P. Bergman, O. Kordina and E. Janzén, *Time Resolved Spectroscopy of Defects in SiC*, *physica status solidi (a)* **162**(1):(1997) p.65-77
- [157] J.F. Young and H.M. van Driel, *Ambipolar diffusion of high-density electrons and holes in Ge, Si, and GaAs: Many-body effects*, *Physical Review B* **26**(4):(1982) p.2147-2158
- [158] D.E. Kane and R.M. Swanson, *The effect of excitons on apparent band gap narrowing and transport in semiconductors*, *Journal of Applied Physics* **73**(3):(1993) p.1193-1197
- [159] D.M. Caughey and R.E. Thomas, *Carrier mobilities in silicon empirically related to doping and field*, *Proceedings of the IEEE* **55**(12):(1967) p.2192-2193
- [160] M. Roschke and F. Schwierz, *Electron mobility models for 4H, 6H, and 3C SiC*, *Ieee Transactions on Electron Devices* **48**(7):(2001) p.1442-1447
- [161] M. Kato, Y. Iwata, Y. Matsushita and M. Ichimura, *Structural and electrical characterization for 3C-SiC homoepitaxial layers*. HeteroSiC - WASMPPE 2009, Catania (Italy): (2009)
- [162] K. Yagi, T. Kawahara, N. Hatta and H. Nagasawa, 'Switch-Back Epitaxy' as a Novel Technique for Reducing Stacking Faults in 3C-SiC, *Materials Science Forum* **527-529**:(2006) p.291
- [163] K.H. Baik, Y.G. Seo, S.K. Hong, S. Lee, J. Kim, J.S. Son and S.M. Hwang, *Effects of Basal Stacking Faults on Electrical Anisotropy of Nonpolar a-Plane (11 $\bar{2}$ 0) GaN Light-Emitting Diodes on Sapphire Substrate*, *Ieee Photonics Technology Letters* **22**(9):(2010) p.595-597
- [164] B. Chen, H. Matsuhata, T. Sekiguchi, A. Kinoshita, K. Ichinoseki and H. Okumura, *Tuning minority-carrier lifetime through stacking fault defects: The case of polytypic SiC*, *Applied Physics Letters* **100**(13):(2012) p.132108-132104
- [165] M. Abadier, R.A. Berechman, P.G. Neudeck, A.J. Trunek and M. Skowronski, *Nucleation of 3C-SiC associated with threading edge dislocations during chemical vapor deposition*, *Journal of Crystal Growth* **347**(1):(2012) p.45-48

[166] R. Vasiliauskas, "*Sublimation Growth and Performance of Cubic Silicon Carbide*", PhD Thesis, (2012)

[167] M. Marinova, A. Mantzari and E.K. Polychroniadis, *Some recent results on the 3C-SiC structural defects*, in "*Nanostructured Materials, Thin Films and Hard Coatings for Advanced Applications*", L. Kolakieva and R. Kakanakov (Eds.), Stafa-Zurich, Trans Tech Publications Ltd, **159**: 39-48 (2010)

[168] R. Vasiliauskas, M. Marinova, M. Syväjärvi, R. Liljedahl, G. Zoulis, J. Lorenzzi, G. Ferro, S. Juillaguet, J. Camassel, E.K. Polychroniadis and R. Yakimova, *Effect of initial substrate conditions on growth of cubic silicon carbide*, Journal of Crystal Growth **324**(1):(2011) p.7-14

Unfortunately people were not lucky enough to find the cup of hemlock which can do away with such a being, for all the poisons they created – envy, slander, and inner anger – were insufficient to destroy that self-satisfied magnificence... who drive the chariot of our culture and every other one, but that almost always the wagon and the horses are inferior material and cannot match the glory of their drivers, who then consider it funny to whip such a team into the abyss, over which they themselves jump with a leap worthy of Achilles.

Friedrich Nietzsche